AGH-UST
University of Science and Technology
in Cracow

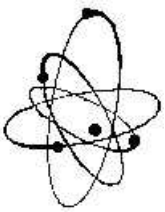

Faculty of Physics and Nuclear Techniques

Dorota Szuba

The study of diffractive photoproduction of J/ψ at large $\gamma - p$ energy in the ZEUS experiment at HERA

PhD Thesis

Supervisor: Prof. dr hab. J. Figiel

February, 2004

In memory of my Grandparents

Abstract

The proton-dissociative diffractive photoproduction of J/ψ mesons has been studied in ep collisions with the ZEUS detector at HERA using an integrated luminosity of 36 pb^{-1}. The differential cross-section $d\sigma/dt$ has been measured at $W \simeq 200$ GeV, where W is the centre-of-mass energy of the photon-proton system, for $|t|$ values up to 7 GeV^2, where t is the squared four-momentum transfer at the proton vertex. The results are compared to expectations of theoretical models.

Acknowledgments

Many people contributed to the work presented here and supported me during my Ph.D. studies. Here I would like to thank all of them.

I would like to thank first of all Professor Danuta Kisielewska for giving me the opportunity to work on my Ph.D. within the ZEUS Collaboration at DESY. I am thankful for all her support during my work.

I would like to thank my supervisor Professor Jan Figiel for his help, advice and encouragement. I am also very grateful for the second independent analysis which he did.

Many thanks to Alessia Bruni for her interest and many fruitful discussions, helpful comments and suggestions.

I wish to thank Leszek Adamczyk for patient answering of numerous questions. I have learned a lot from him and I would like to give special thanks to him.

I wish to thank Agnieszka Kowal for sharing an office with me for such a long time and for her hard work on correcting my English.

I wish to thank Leszek Suszycki, Katarzyna Klimek, Janusz Chwastowski and Leszek Zawiejski for many discussions and support in solving numerous problems.

Special thanks to Krzysztof and Agnieszka Wrona for their help in solving plenty of technical problems and their care during my stays at DESY.

Finally, I would like to express my gratitude to my family, especially to my husband Janusz and children Kuba and Gosia, who have always been patient, loving, caring and understanding. This thesis and work towards it would not have been possible without them.

Contents

Introduction **6**

1 Diffractive vector meson production in electron-proton scattering **8**

1.1 Electron-proton scattering 8

1.2 Photon-proton scattering 9

1.3 Structure of the proton 10

1.4 Classification of hadronic processes 10

1.5 Quantum Chromodynamics 10

1.5.1 Factorization 11

1.5.2 Evolution equations 12

1.6 Diffraction in hadron physics 13

1.7 Regge phenomenology 15

1.8 Diffraction in photoproduction 18

1.8.1 Hadronic character of the photon 18

1.8.2 Classification of diffractive γp processes 19

1.8.3 Vector meson photoproduction 19

1.8.4 Regge theory expectation 20

1.8.5 Proton-dissociative vector meson photoproduction in pQCD models 21

2 The HERA collider and the ZEUS detector **23**

2.1 Overview of the ZEUS experiment 25

2.2 The Central Tracking Detector 27

2.3 The Uranium Calorimeter 28

2.4 The Proton Remnant Tagger 29

2.5 Luminosity measurement 29

2.6 The electron tagger at 35m 31

2.7 The muon detectors 32

2.8 Other detector components 32

2.9 The ZEUS Data Acquisition System 32

3 Monte Carlo **34**

3.1 Monte Carlo simulation 34

3.2 MC generators 34

4 Event reconstruction **37**

4.1 Event characteristics 37

4.1.1 The event topology 37

4.2 Event reconstruction 39

4.2.1 The CTD reconstruction 39

4.2.2 Detection of the particles in the UCAL 40

4.2.3 Matching of tracks with calorimeter objects 42

4.2.4 The reconstruction of proton dissociation system 42

4.2.5 Detection of the scattered electron 43

4.2.6 The reconstruction of the kinematic variables 45

5 Data selection **47**

5.1 Trigger 47

5.2 Offline selection 48

5.2.1 General cuts 48

5.2.2 The tracking requirements 48

5.2.3 Track-cluster matching 49

5.2.4 Lepton identification 49

5.2.5 Reconstruction of the lepton energy 52

5.2.6 Proton dissociation 55

5.2.7 The kinematic cuts 55

5.3 Mass distribution 56

6 Data and Monte Carlo comparison **59**

6.1 Tuning of the MC parameters 59

6.2 Background studies 61

6.3 Comparison of data and MC 61

6.4 Binning 61

7 Experimental Results **69**

7.1 Cross section definition 69

7.2 Systematic uncertainties 70

7.3 Differential cross section 73

7.4 Comparison with other measurements 77

8 Comparison with theoretical models **82**

8.1 Comparison with BFKL model 82

8.2 Comparison with DGLAP model 86

9 Summary **88**

List of Figures

1 Lepton-proton scattering 8
2 Notation of a ladder diagram of n gluon emission. 12
3 Particle spins plotted against their squared masses. 16
4 Total photoproduction cross section as a function of $W_{\gamma p}$ 17
5 Vector meson production in the VDM. 18
6 Elastic and proton-dissociative vector meson production. 20
7 The pQCD diagrams for proton-dissociative vector meson production. . . 22
8 The HERA storage ring. 23
9 Luminosity delivered by HERA in the 1993-2000 running periods. 24
10 The ZEUS detector. 26
11 A schematic picture of the calorimeter. 29
12 The scheme of PRT detectors. 30
13 Luminosity system. 31
14 Data and MC simulation chain. 34
15 QED processes included in GRAPE MC. 36
16 Event topologies. 38
17 Z-vertex distribution. 40
18 ZUFO - a clustering in the CAL. 41
19 The Distance of Closest Approach. 42
20 The energy distributions in photon and electron detectors. 43
21 The correlation of the electron ADC'_e and the photon ADC_γ. 44
22 Electrons and muons shower in the CAL. 50
23 The E_{EMC}/E distribution for events with PT35m trigger. 51
24 The invariant mass spectrum with one lepton identified as an electron. . . 52
25 The E_{EMC}/E distribution for events with BRMU trigger. 53
26 The angular distribution of decay lepton candidates 54
27 The mass reconstruction done with the CAL only and with the CAL and the PT35m. 55

28 The energy distribution in the FCAL before and after the PRT tag. 56
29 The J/ψ mass distribution for all event topologies in the data. 57
30 The mass distribution of the final sample. 58
31 The E_{FCAL} distributions in the data and MC before and after β correction. 60
32 The distribution of the energy of tagged electron. 62
33 The distributions of W and t in the data and MC 63
34 The distributions of E and p_t in the data and MC 64
35 Study of reconstruction of variable $E_{e'}$. 66
36 Study of reconstruction of variable t. 67
37 Acceptance in the function of $|t|$ 68
38 Systematic uncertainty for $J/\psi \to e^+e^-$ 71
39 Systematic uncertainty for $J/\psi \to \mu^+\mu^-$ 72
40 $M_{e^+e^-}$ distributions in bins of $|t|$ 74
41 $M_{\mu^+\mu^-}$ distributions in bins of $|t|$ 75
42 $d\sigma/dt$ for the electron and muon decay channels separately 76
43 The combined $d\sigma/dt$ with a power-like fit for $M_Y^2/W^2 < 0.1$. 77
44 Comparison of $d\sigma/dt$ with ZEUS 1995 measurement. 78
45 Comparison of $d\sigma/dt$ with ZEUS 1996-1997 measurement. 79
46 Comparison of $d\sigma/dt$ with H1 measurement. 80
47 The cross section as the function W. 81
48 Comparison of $d\sigma/dt$ with the predictions of BFKL based pQCD model. . 84
49 Comparison of $d\sigma/dt$ at $W \approx 100\,\text{GeV}$ and $W \approx 200\,\text{GeV}$ with the BFKL model. 85
50 Comparison of $d\sigma/dt$ with the DGLAP based pQCD model. 87

Introduction

The discovery of the J/ψ particle played a very important role in the development of the Standard Model. In November 1974 the M.I.T. group at the Brookhaven National Laboratory discovered a resonance at mass 3.1 GeV decaying into an e^+e^- pair from the collisions of 30 GeV protons with a beryllium target [1]. This resonance was attributed to the production of a new particle J. Meanwhile researches at SPEAR, the electron-positron storage ring at SLAC, observed the process of electron-positron annihilation to hadrons. They found an enormous and very narrow resonance at a collision energy of about 3.1 GeV and addressed it to a new particle ψ [2]. Because of this double discovery, nowadays this particle is known as J/ψ. The simultaneous publications in 1974 in Physics Review Letters, along with a third, independent, confirmation [3] gave a reason for a flood of theoretical discussions. The leaders of the two collaborations which made the discovery of new particle, Ting and Richter, were rewarded in 1976 with the Nobel prize.

The very long lifetime of J/ψ, as indicated by the small width of the resonance (~ 90 keV), allowed to interpret this particle, as a meson built up of the new, heavy charm quarks, whose existence had been postulated earlier [4, 5].

The J/ψ is an example of quarkonium, a term used for mesons which are formed of a heavy quark plus its antiquark. Since it has spin 1, odd parity and odd charge conjugation ($\mathrm{J}^{PC} = 1^{--}$) it is a vector meson. These are the same quantum numbers which a photon has.

Many years after the discovery, the production of J/ψ mesons still generates interest. Through its leptonic decay modes it provides a clean experimental signature. The charm quark mass (~ 1.5 GeV), which sets a scale of QCD interactions involving the J/ψ is just large enough to allow the application of perturbative QCD (pQCD) calculations. It is expected also, that for the diffractive vector meson production, the large four momentum transfer squared at the proton vertex, t, may also be a hard scale. The measurement of the J/ψ production cross section in γp collisions can provide information on the gluon density of the nucleon.

The subject of this study is proton-dissociative J/ψ photoproduction at high $|t|$. This analysis is an extension in γp center of mass energy range of the previous ZEUS measurements [6, 7] and covers a similar $|t|$ range. The data sample analyzed was collected in 1996 and 1997 and corresponds to an integrated luminosity of $36\,\mathrm{pb}^{-1}$.

The thesis is organized as follows:
The first Section introduces the kinematic variables used in the study of vector meson photoproduction and gives the outline of vector meson production theory. The second Section describes the experimental setup, focusing on the relevant aspects of the HERA

collider and on the ZEUS detector. The third Section presents the Monte Carlo simulation programs that were used extensively in the present analysis to estimate experimental acceptance and resolution and to estimate the background contamination. The methods used in the reconstruction of kinematic variables are described in Section 4. The trigger and offline event selection are described in Section 5. The sixth Section gives the description of the tuning of the MC simulation and comparison of the data and the simulation. In Section 7 the results of this analysis are presented and compared with other measurements. Section 8 presents the comparison of the experimental results with theoretical expectations. The summary is drawn in Section 9.

1 Diffractive vector meson production in electron-proton scattering

1.1 Electron-proton scattering

The electron-proton scattering is mediated by the exchange of a virtual vector boson. The intermediate boson may be a virtual photon (γ^*) or one of the weak gauge bosons (Z^o, $W^{\pm}$). Further, we focus on the photon exchange, since the weak *ep* interactions are beyond the kinematic range used in this analysis. In the lowest order, lepton-proton scattering is described by the diagram shown in Fig. 1, where P, P', k, k', q denote the four momenta of the incoming proton, the outgoing hadronic system, the incoming lepton, the scattered lepton and the exchanged virtual photon, respectively.

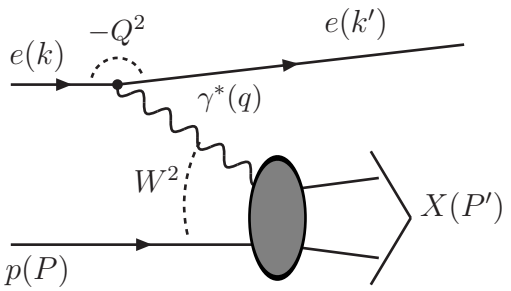

Figure 1: *Schematic diagram of electron-proton scattering in one-photon-exchange approximation. X represents any hadronic final state.*

The electron-proton scattering can be described in terms of the following variables:

- the square of the *ep* centre-of-mass energy

$$s = (k + P)^2 \approx 4E_p E_e, \tag{1}$$

  where E_p, E_e denote the proton and electron initial energy, respectively;

- the negative squared four-momentum of the exchanged photon

$$Q^2 = -q^2 = -(k - k')^2; \tag{2}$$

- the fraction of the electron energy transferred to the hadronic final state in the rest frame of the initial state proton

$$y = \frac{P \cdot q}{P \cdot k} \approx \frac{E_e - E'_e}{E_e}, \tag{3}$$

  where E'_e is the energy of the scattered electron;

- the squared centre-of-mass energy of the photon-proton system

$$W^2 = (q + P)^2 \approx sy. \tag{4}$$

1.2 Photon-proton scattering

In *ep* interactions via photon exchange, one can view the lepton beam as a source of virtual photons which then interact with the proton. The exchanged photon is treated as a massive spin 1 particle and acquires three polarization vectors corresponding to helicities $\lambda = \pm 1, 0$, where the last one would become negligible for Q^2 sufficiently small. The cross section may depend on the photon helicity, although for parity invariance reasons the cross sections for $\lambda = \pm 1$ have to be equal. There will be thus two independent cross sections: one for absorbing a transversely polarized photon $\sigma_T(\lambda = \pm 1)$ and one for longitudinally polarized photons $\sigma_L(\lambda = 0)$. The differential cross section for the *ep* interaction for $Q^2 \ll W^2$ can be expressed as:

$$\frac{d^2\sigma_{ep}}{dydQ^2} = \Gamma_T \sigma_T^{\gamma^* p}(y, Q^2) + \Gamma_L \sigma_L^{\gamma^* p}(y, Q^2), \tag{5}$$

where Γ_T and Γ_L are, respectively, the transverse and longitudinal photon fluxes generated at the leptonic vertex which is calculable within QED, defined as

$$\Gamma_T = \frac{\alpha_{QED}}{2\pi Q^2}\left(\frac{1+(1-y)^2}{y} - \frac{2(1-y)}{y}\frac{Q^2_{min}}{Q^2}\right), \tag{6}$$

$$\Gamma_L = \frac{\alpha_{QED}}{2\pi Q^2}\frac{2(1-y)^2}{y}, \tag{7}$$

where α_{QED} is the fine structure constant, and $Q^2_{min} = \frac{m_e^2 y^2}{1-y}$ is the minimum possible value of Q^2, with m_e being the electron mass. For $Q^2 \to 0$ limit they satisfy:

$$\lim_{Q^2 \to 0} \sigma_T^{\gamma^* p}(y, Q^2) = \sigma^{\gamma p}(y), \tag{8}$$

$$\lim_{Q^2 \to 0} \sigma_L^{\gamma^* p}(y, Q^2) = 0. \tag{9}$$

For the photon virtualities $Q^2 < 0.01\,\mathrm{GeV}^2$, covered by this measurement, $\sigma_L^{\gamma^* p}$ and the Q^2 dependence of $\sigma_T^{\gamma^* p}$ can be neglected, so the differential cross section can be rewritten as [8]

$$\frac{d^2\sigma_{ep}}{dydQ^2} = \Gamma_T(y, Q^2)\sigma^{\gamma p}(y). \tag{10}$$

The *ep* cross section can be extracted from the photon-proton cross section since one is related to the other by means of the photon flux factor generated at the leptonic vertex which can be integrated over the y and Q^2 range covered by the measurement.

1.3 Structure of the proton

The internal structure of the proton was considered in various approaches. In the Feynman model [9] the proton is built up of the free point-like objects called *partons*. Each parton i carries a fraction ξ_i of the proton momentum p ($0 \leq \xi_i \leq 1$). The inelastic ep cross section is given by the incoherent sum of quasi-elastic electron-parton scattering. The *Quark Model*, developed independently by Gell-Mann [10] and Zweig [11, 12] treated all hadrons as constructed from three spin-$\frac{1}{2}$ fermions called *quarks*. In 1969 Bjorken and Paschos [13] identified partons as objects identical to quarks within the model called therefore *Quark Parton Model* (QPM). In the Quantum Chromodynamics (QCD) an improved parton model these partons interacts among themselves by the exchange of gluons. These gluons can split up to create $q\bar{q}$ pairs (sea quarks) and the gluon-gluon pairs. Each parton (quark or gluon) can emit or absorb another parton, the probability of which itself depends on parton densities. The fractional charge of the partons and the postulated number of three valence quarks in the nucleons was confirmed by neutrino-nucleon scattering [14]. Direct evidence for the existence of gluons was found in 1979 at DESY in the observation of three-jet events in e^+e^- annihilation [15].

1.4 Classification of hadronic processes

Hadronic processes are traditionally classified into two distinct groups: *soft* and *hard* processes.

- The *soft processes* are characterized by an energy scale of the order of the hadron size R ($\sim 1\,\mathrm{fm}$). This is the only typical scale of such processes. The momentum transfer squared is generally small: $|t| \sim 1/R^2$ ($\sim$ few hundred MeV)^2. The t-dependence of the cross section is exponential, $d\sigma/dt \sim e^{-R^2|t|}$. The soft processes are very well described by the Regge theory.
- The *hard processes* are characterized by two (or more) energy scales: one is still the hadron size, the other is a 'hard' energy scale. In the case of a hard scale the momentum transfer is large ($\geq 1\,\mathrm{GeV}^2$). The cross section is typically powerlike. The examples of hard processes are: deep inelastic scattering, or large $|t|$ heavy vector meson production. The presence of a hard scale allows one to use perturbative QCD to describe the process.

1.5 Quantum Chromodynamics

Quantum Chromodynamics (QCD) is the field theory of the strong interaction. It introduces an additional quantum number - color charge carried by quarks. The three coloured

quarks of one flavor form a triplet. The gauge bosons of QCD are the eight gluons carrying a combination of colour and anti-colour. QCD is a non-abelian gauge theory, based on the SU(3) symmetry group. In contrary to QED, the QCD coupling constant α_s is scale dependent by the introduction of an effective reference scale μ, namely the renormalization scale. The scale dependence in leading order perturbation theory is given as

$$\alpha_s(\mu^2) = \frac{12\pi}{(11 - 2n_f)\ln(\mu^2/\Lambda^2_{QCD})} \tag{11}$$

where n_f is the number of quark flavors. The QCD parameter Λ_{QCD} determines the energy scale at which α_s becomes small. The parameter Λ_{QCD} has been measured to be $(100 - 300)$ MeV. The α_s increases for small momentum transfers (large distances) and is small at large momentum transfers. At large distances the force between quarks becomes so large that is not possible to observe free quarks outside bound states. This property is known as *confinement* of the quarks in hadrons. At small distances the strong interaction becomes weak and in consequence the partons in the proton do not interact with each other. This is referred to as *asymptotic freedom* of the quarks.

1.5.1 Factorization

In the QCD improved parton model a hadron-hadron or lepton-hadron scattering process is the result of interactions between the quarks, gluons or photons of the one incoming particle with those from the other particle. The incoming particles can be viewed as a beam of partons or photons carrying fractions of its momenta. To calculate, for example the *ep* scattering cross section, it must be separated into two independent parts. The interaction between virtual photon and a quark with a given momentum fraction x in the proton is a short-range process and can be obtained using perturbative calculations. The probability to find a particular quark having a momentum fraction between x and $x + dx$ is given by a long-range process, which cannot be calculated in pQCD. The separation of the scattering process in short and long range physics is called *factorization*.

The the quark $q_i(\mu^2, x)$ and gluon $g_i(\mu^2, x)$ density distributions must be determined experimentally. However, if they are known at one particular value of μ^2 or x they can be under certain conditions calculated for other regions. It can be done using DGLAP or BFKL evolution equations. The Dokshitzer-Gribov-Lipatov-Altarelli-Parisi (DGLAP) equations allow one to determine the parton distributions for fixed x at any value of μ^2, while the Balitzky-Fadin-Kuraev-Lipatov (BFKL) equation describes an evolution in x for fixed μ^2.

1.5.2 Evolution equations

DGLAP evolution

The DGLAP evolution equations [16–19] allow to determine the parton density evolutions with Q^2, if they are known at one particular value of Q_0^2 and for a fixed x. In the leading logarithmic approximation (LL) terms of the form $(\alpha_s \ln Q^2)^n$, which are dominant at large Q^2, are summed to all orders of n. The amplitude for the ep scattering process can be obtained by summing ladder diagrams of consecutive gluon emissions, see Fig. 2. The struck quark evolves from the incoming proton and by such gluon emission loses, gradually, its longitudinal momentum. The fraction of longitudinal momentum x_j is ordered $x_1 > x_2 > ... > x_n$, while the gluon transverse momenta are strongly ordered along the ladder i.e. $Q_0^2 \ll k_{T1}^2 \ll ... \ll k_{Tn}^2 \ll Q^2$. This is valid for large Q^2 and restricts DGLAP calculations to $(\alpha_s(Q^2) \ln \frac{1}{x} \ll 1$.

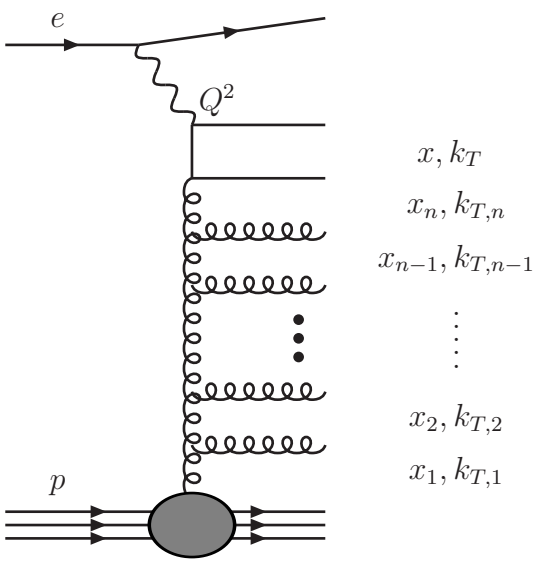

Figure 2: *Notation of a ladder diagram of n gluon emission.*

BFKL evolution

In the kinematic region of small x the parton density evolution can be described by the BFKL formalism [20–22]. The BFKL evolution sums the terms $(\alpha_s \ln \frac{1}{x})^n$ up to all n. It takes into account ladder diagrams where the longitudinal momentum fraction are

strongly ordered $x_1 \gg x_2 \gg ... \gg x_n$, and the gluon ladder does not have to be ordered in k_T.

1.6 Diffraction in hadron physics

The term *diffraction* was introduced in nuclear high-energy physics about fifty years ago. This term is used in strict analogy with the familiar optical phenomenon, that occurs when a beam light crosses a hole or meets an obstacle whose dimensions are comparable to its wavelength. In high energy particle physics it was first used to describe small angle elastic hadron-hadron scattering of the type $a+b \to a+b$. Later, diffraction was extended to processes when one (*single dissociation:* $a+b \to X+b$) or both (*double dissociation:* $a+b \to X+Y$) colliding hadrons dissociate into a multi-particle final state preserving the quantum numbers of the initial hadrons.

According to Good and Walker [23], who gave the first description, the *hadronic diffraction* is:

A phenomenon [...] in which a high energy particle beam undergoing diffraction scattering from a nucleus will acquire components corresponding to various products of the virtual dissociations of the incident particle [...] These diffraction-produced systems would have a characteristic extremely narrow distribution in transverse momentum and would have the same quantum numbers of initial particle.

Hadronic diffractive processes are defined as the reactions at high energy in which no quantum numbers (other then the vacuum quantum numbers) are exchanged between the colliding particles.

The coherence condition between the outgoing and incoming waves, which defines diffraction [23] for single dissociative diffractive process, $a+b \to X+b$, is:

$$\frac{M_X^2}{s} \lesssim \frac{1}{2m_a R}, \tag{12}$$

where M_X is the mass of the system X and R is the interaction radius. For R of the order of [1] $1\,\text{fm} \approx 5\,\text{GeV}^{-1}$ one gets $\frac{M_X^2}{s} < 0.1$.

The consequence of Eq. 12 is a suppression of the large mass diffractive states:

$$\frac{d\sigma}{dt dM_X^2} \sim \frac{1}{M_X^2}, \tag{13}$$

[1] In natural unit system ($c = \hbar = 1$) one has equivalence between distance and energy units with conversion factor $\hbar c = 197.3\,\text{MeV fm}$.

where t is Mandelstam variable. At high energies the diffractive processes have a characteristic signature: there is no exchange of quantum numbers in t-channel, what implies no color charge exchange at the partonic level. Therefore the outgoing systems are well separated in the phase space. This is most common for elastic and single dissociation, where at least one of the incoming particles emerges from the collision with a very small loss of its initial energy, simultaneously preserving its identity. Diffractive events are thus characterized by a large rapidity gap, given by

$$\Delta Y = \ln \frac{s}{M_X^2}. \tag{14}$$

Experimentally, the rapidity gap can be i.e. a large angle separation and can be approximated for particles with small mass, ($E \simeq |p|$), by the *pseudorapidity*

$$\eta = -\ln \tan \left(\frac{\theta}{2} \right), \tag{15}$$

where θ is the polar angle measured with respect to the collision axis.

Another feature of diffractive scattering is the exponential suppression of the cross section as a function of t. This is reminiscent of diffraction in optics, where the intensity of scattered light from a circular aperture is a function of an angle. For small t region the diffractive cross section can be parametrized as

$$\frac{d\sigma}{dt} \propto e^{-b|t|}. \tag{16}$$

The slope of b is related to the interaction radius R of the target by $b = \frac{R^2}{4}$. It typically increases slowly with energy s, what is known as *shrinkage* of the diffractive peak.

At high energies the energy dependence of the forward elastic cross section can be parametrized as

$$\frac{d\sigma_{el}}{d|t|}(t = 0) \propto s^{2\epsilon} \tag{17}$$

and according to the optical theorem the energy dependence of the total cross section can be expressed by

$$\sigma_{tot} \propto s^{\epsilon}, \tag{18}$$

where $\epsilon = 0.08$ was found experimentally [24].

At HERA the observed fraction of the diffractive events is of the order of 10%, fairly independent of W and Q^2 [25].

1.7 Regge phenomenology

The hadron-hadron interactions are well described by Regge phenomenology [26,27] based on the formalism of the analytical continuation of the scattering amplitude into the complex angular momentum. Regge theory successfully describes the energy dependence of the total hadron-hadron interaction cross section and certain properties of elastic and diffractive scattering. The review of Regge theory one can find in [28].

The interaction in hadron-hadron scattering is viewed as due to the exchanges of collective states called *Regge poles*. A Regge pole is equivalent to a superposition of many particles with the same quantum numbers except for spin. All exchanged particles fit on a line called a *Regge trajectory* or *reggeon* in a Chew-Frautschi plot [29], in the $J - m^2$ plane, where J is the spin of the particle and m its mass, as shown in Fig. 3 (spin $J = \alpha$, $m^2 = t$). The continuation of a trajectory to negative values of m^2 leads to a parameterization of t as

$$\alpha(t) = \alpha_0 + \alpha' \cdot t, \tag{19}$$

where α_0 is the intercept and α' is the slope of the trajectory. The lightest particle on a trajectory gives the name to the trajectory itself. The slope of $\alpha^{'}$ is typically close to $1\,\mathrm{GeV}^{-2}$. The intercept α_0 of trajectories corresponding to known particles is in the range $0 - 0.5$, for instance $\alpha_\pi \approx 0$, $\alpha_\rho \approx 0.5$. In the high energy limit, $s \to \infty$, and at fixed t the scattering amplitude, for each Regge pole, can be written as

$$A(s,t) \overset{s\to\infty}{\longrightarrow} \beta(t) \left(\frac{s}{s_0}\right)^{\alpha(t)}, \tag{20}$$

where $s_0 \simeq 1\,\mathrm{GeV}^2$ is the hadronic mass scale.

The cross section of the elastic scattering process, of type $ab \to ab$ is

$$\frac{d\sigma_{el}}{dt} \propto \frac{1}{s^2}|A(s,t)|^2 \propto F(t) \left(\frac{s}{s_0}\right)^{2\alpha(t)-2}. \tag{21}$$

The observed exponential decrease of $d\sigma/dt$ with increasing t leads to parameterization $F(t) = e^{-bt}$. Inserting this and Eq. 19 into Eq. 21 the differential cross section can be written as

$$\frac{d\sigma_{el}}{dt} \propto \left(\frac{s}{s_0}\right)^{2\alpha(t)-2} e^{-bt}, \tag{22}$$

with

$$b = b_0 + 2\alpha^{'} \left(\frac{s}{s_0}\right). \tag{23}$$

The width of the forward peak $\Delta|t| = \left(b_0 + 2\alpha^{'}\left(\frac{s}{s_0}\right)\right)^{-1}$ decreases as the energy increases. This is the shrinkage of the diffractive peak, which can be interpreted as an increase of the

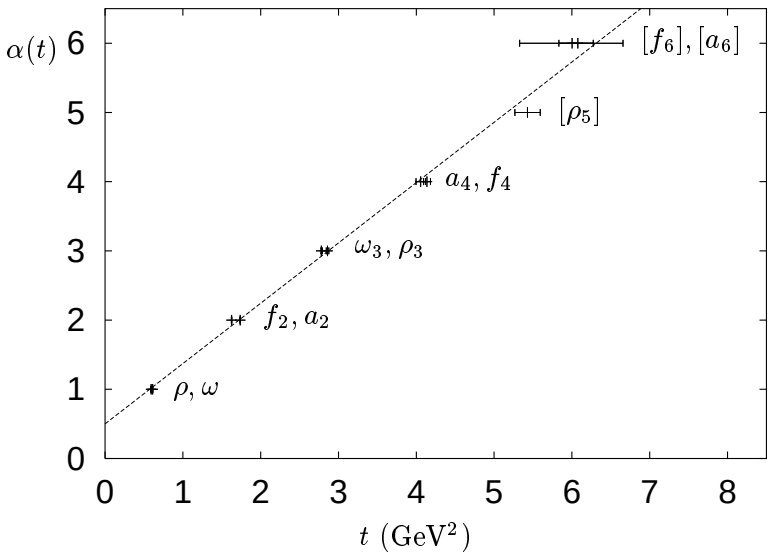

Figure 3: *Particle spins plotted against their squared masses t. The straight line is the corresponding Regge trajectory: $\alpha(t) = 0.5 + 0.9t$. The particles in square brackets are listed in the data tables [30], but there is some doubt about them. The figure is taken from [31].*

interaction radius $R_{int} \overset{s\to\infty}{\sim} \sqrt{\alpha' \ln s}$. The prediction of the shrinkage, having no analogy in optics is an important achievement of Regge theory.

Using the optical theorem, which relates the total cross section to the elastic scattering amplitude, the energy dependence of the total hadron-hadron scattering cross section is:

$$\sigma_{tot} \sim \frac{1}{s} \mathrm{I}m[A(s, t = 0)] \propto \left(\frac{s}{s_0}\right)^{\alpha_0 - 1} . \tag{24}$$

The exchange of Regge trajectories, having intercepts up to 0.5, leads to total cross sections decreasing with energy, accordingly to Eq. 24. However, it is experimentally known that the hadronic total cross sections are flat for a wide range of energy and increase slowly at high energies. In order to describe the data within the Regge framework a new trajectory named *pomeron* (IP), after I. Ya. Pomeranchuk has been introduced [29,32] with $\alpha_{\mathrm{IP}} \approx 1$. In the case of the exchange of reggeons the quantum numbers are exchanged, while in the case of pomeron exchange the vacuum quantum numbers are exchanged (zero electric and color charge, izospin 0 and C parity +1).

Donnachie and Landshoff [24] used experimental results of the total hadron-hadron interaction to extract the pomeron trajectory. The cross sections were fitted using a parame-

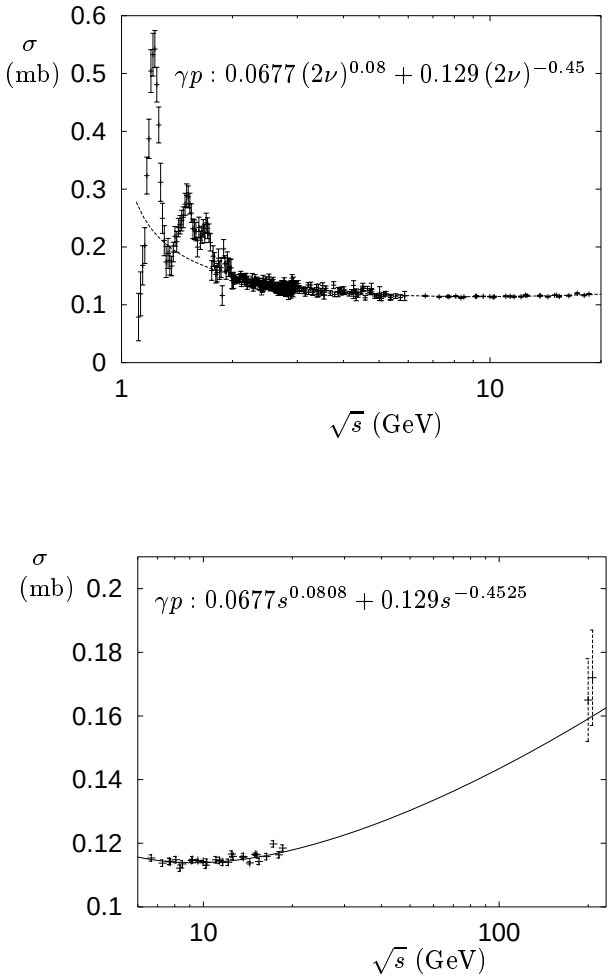

Figure 4: *Total photoproduction cross section as a function of the γp center of mass energy $W_{\gamma p}$ at low energy (upper plot) and at high energy (lower plot) together with a common Donnachie-Landshoff fit. The figure is taken from [31].*

terization of the form

$$\sigma_{tot} = As^{\alpha_{\rm IR}-1} + Bs^{\alpha_{\rm IP}-1}. \tag{25}$$

The first term in Eq. 25 correspond to the exchange of a reggeon, responsible for the decrease of the cross section at low energies, while the second term accounts for the pomeron contribution, which dominates at high energies. The results of the fits are: $\alpha_{\rm IR}-1 = 0.4525$ and $\alpha_{\rm IP}-1 = 0.0808$. In the pomeron case, the following parameterization of its trajectory has been extracted

$$\alpha_{\rm IP} = 1.08 + 0.25t. \tag{26}$$

This pomeron trajectory, which describes the weak dependence of the total cross section is known as *soft* pomeron.

1.8 Diffraction in photoproduction

1.8.1 Hadronic character of the photon

The fixed target experiments in the 60's, where the scattering of photons on protons was studied, showed remarkable similarities between photon-proton and the hadron-hadron interactions. The possible way to understand this fact was the assumption of a structured nature of the photon. The physical photon $|\gamma>$ can be considered as a superposition of two states: a bare photon $|\gamma_B>$ and a hadronic component $\sqrt{\alpha}|h>$

$$|\gamma>=\sqrt{Z_3}|\gamma_B>+\sqrt{\alpha}|h>, \tag{27}$$

where $\alpha = 1/137$ is the electromagnetic coupling constant and Z_3 is the proper normalization. The hadronic state $|h>$ dominates due to very large hadron-hadron cross section. Conservation laws require that the hadronic component has the same quantum numbers as the photon i.e. $J^{PC} = 1^{--}, Q, B, S = 0$. The major contribution to $|h>$ are the light vector mesons ρ^0, ω, ϕ. The restrictive assumption, that these vector mesons are responsible for hadronic interactions and the bare photon $|\gamma_B>$ does not interact with the proton at all, is the hypothesis of the Vector Dominance Model (VDM) [33]. A later generalization included more constituents than ρ^0, ω, ϕ is referred to as Generalized Vector Dominance Model (GVDM) [34].

Within the VDM the photoproduction of vector mesons at small photon virtuality ($Q^2 \approx 0$) and small values of W has good explanation. This process may be explained in the following way. The photon fluctuates, due to the uncertainty principle, into a $q\bar{q}$ pair with the same quantum numbers, a vector meson. The time allowed for this fluctuation is $t_f \sim \frac{2\nu}{Q^2+M_V^2}$, where ν is the photon energy in the proton rest frame and M_V is the mass of the vector meson the photon fluctuates into. If the $t_f \gg t_i$, where the interaction time $t_i = R_p$ with R_p being the proton radius, the photon interacts as if it was a hadron, so the vector meson scatters elastically off the incoming proton, see Fig. 5.

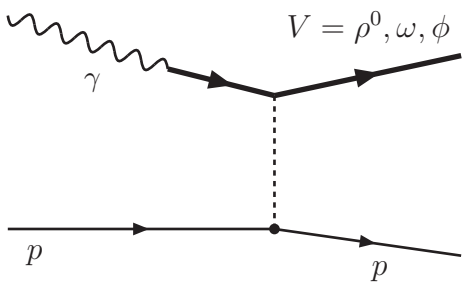

Figure 5: *A diagram for vector meson production based on the VDM.*

1.8.2 Classification of diffractive γp processes

The γp interaction in photoproduction ($Q^2 \approx 0$) is predominantly a hadronic interaction. In analogy to hadron-hadron scattering, γp diffractive processes can be divided into four classes:

1. 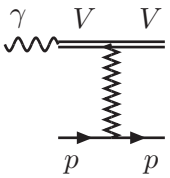

elastic scattering, $\gamma p \to V + p$, where the photon fluctuates into a vector meson V and scatters off the proton elastically,

2. 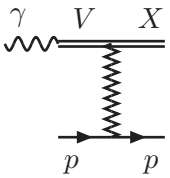

single photon dissociation, $\gamma p \to X + p$, where the photon dissociates into a higher mass state X, while the proton remains intact,

3. 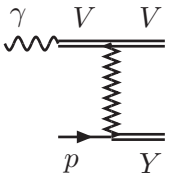

single proton dissociation, $\gamma p \to V + Y$, the photon remains intact and the proton dissociates into a higher mass state Y,

4. 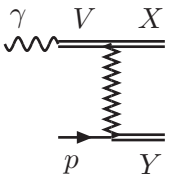

double dissociation, $\gamma p \to X + Y$, both the photon and the proton dissociate into higher mass states.

1.8.3 Vector meson photoproduction

In *ep* interactions vector mesons are produced via interaction of the exchanged almost real or virtual photon with the incoming proton.

The examples of diffractive process in which the photon fluctuates into a vector meson are the following reactions: $\gamma p \to Vp$, called *elastic* or *exclusive* vector meson production and $\gamma p \to VY$, where the proton breaks up into higher mass state Y. The latter is referred to as *proton dissociative* vector meson production and will be studied in detail in this thesis, see Fig. 6.

For this process additional (to these defined in Sec. 1.1) variables are introduced:

- the four momentum squared at the photon vertex

$$t = (q - v)^2 = (P - P')^2, \tag{28}$$

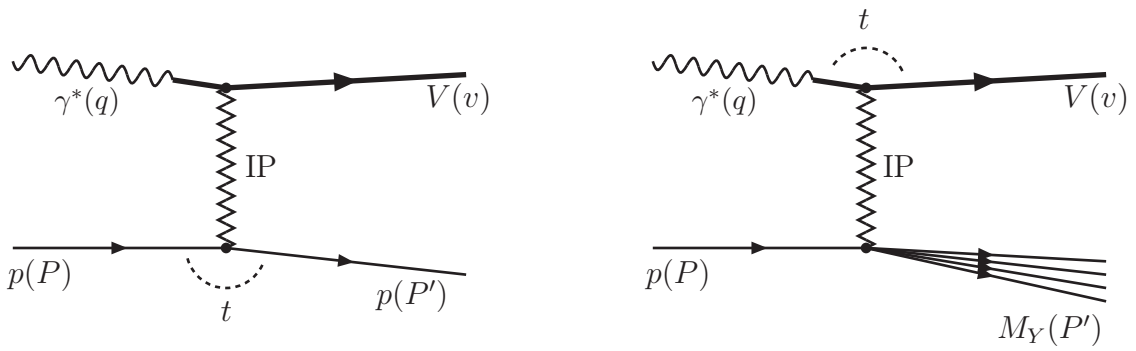

Figure 6: *Diagrams of diffractive vector meson production processes: elastic vector meson production (left) and proton dissociative vector meson production (right).*

where v is the four momentum of the vector meson,

- the vector meson mass M_V,
- the mass M_Y of the proton dissociative system, where

$$M_Y^2 = (P')^2. \tag{29}$$

1.8.4 Regge theory expectation

The photoproduction of vector mesons can be viewed in the following way: the virtual photon emitted from the incoming lepton fluctuates according to VDM into a vector meson, which then interacts with the proton through the exchange of a pomeron. The absorption of the pomeron four-momentum puts the vector meson on the mass shell.

The elastic and proton dissociative γp cross sections, predicted by the Regge theory, can be obtained using formulae presented in Sec. 1.7.

The elastic $\gamma p \to Vp$ cross section is expect to have a form

$$\frac{d\sigma_{\gamma p \to Vp}}{d|t|} \propto e^{-b_{el}|t|} \left(W^2\right)^{2(\alpha_{\rm IP}(t)-1)}, \tag{30}$$

where

$$b_{el} = b_0 + 2\alpha'_{\rm IP} \ln(W^2). \tag{31}$$

The $W_{\gamma p}$ dependence of the elastic cross section is (in the HERA kinematic region)

$$\sigma^{el}_{\gamma p \to Vp} \propto \frac{(W^2)^{2(\alpha_{\rm IP}(t)-1)}}{b(W^2_{\gamma p})} \approx W^{0.22}, \tag{32}$$

For the case of proton dissociative vector meson production the cross section can be approximated by

$$\frac{d\sigma_{\gamma p\to VY}}{dtdM_Y^2} \propto e^{-b_{pd}|t|}\frac{1}{M_Y^2}\left(\frac{W^2}{M_Y^2}\right)^{2(\alpha_{\rm IP}(t)-1)} [(M_Y^2)^{\alpha_{\rm IP}(0)-1} + R\cdot(M_Y^2)^{\alpha_{\rm IR}-1}], \qquad (33)$$

where

$$b_{pd} = b_0 + 2\alpha'_{\rm IP}\ln\left(\frac{W^2}{M_Y^2}\right). \qquad (34)$$

The light vector mesons photoproduction exhibit the features predicted by Regge theory over wide range of W. On the other hand J/ψ photoproduction shows a much steeper energy dependence. Also for electroproduction of light vector mesons, the cross section rises with W as W^δ, with δ increasing with Q^2. The understanding of these features requires different approaches such as perturbative QCD, discussed in next sections.

1.8.5 Proton-dissociative vector meson photoproduction in pQCD models

The diffractive photoproduction of J/ψ mesons in γp interaction, $\gamma p \to J/\psi\, Y$ with large momentum transfer t is an excellent tool to probe the parton dynamics of the diffractive exchange. This process is interesting experimentally, because of the clean signal; an isolated vector meson with large transverse momentum, well separated from the proton remnant by a large rapidity gap. The scattering is mediated by the exchange of a colour singlet object. A hard scale, necessary to justify calculations within pQCD framework, is given by the vector meson mass and the momentum transfer t. The description of the hard diffractive process is simplified by a factorization theorem. The scattering amplitude for such process can be written as a convolution of the wave function of the produced vector meson, a hard interaction part and a part related to the density of partons in the proton.

The diffractive photoproduction of vector mesons can be modeled in the proton rest frame, where photon fluctuates into a $q\bar{q}$ pair a long time before the interaction. The lifetime of the fluctuation is inversely proportional to Bjorken x. The interaction between a $q\bar{q}$ fluctuation and the proton as a colour singlet exchange can be described in the lowest order (LO) QCD by the exchange of two gluons [35]. In the leading logarithmic (LL) approximation this process is referred to the effective exchange of a gluon ladder. Both processes are schematically shown in Fig. 7. After the scattering the photonic fluctuation forms the vector meson. This transition is a soft, non-perturbative component and its description requires the knowledge of the vector meson wave function.

The diffractive process, $\gamma p \to J/\psi\, Y$, at large $|t|$ takes placed by exchange of the 'hard' pomeron. This process is analyzed within the Regge limit $s \gg t \gg Q_0^2$, where Q_0^2 is

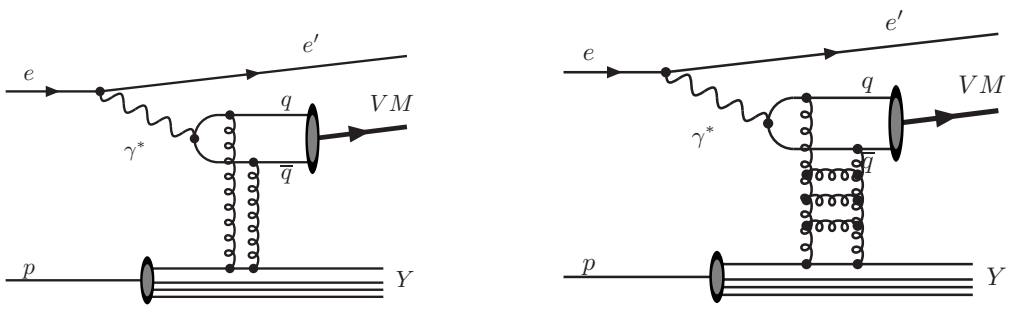

Figure 7: *Left: the pQCD diagram for proton-dissociative vector meson production via two-gluon exchange. Right: the pQCD diagram with gluon ladder exchange.*

the typical hadronic scale of the order $\sim 1\,\mathrm{GeV}^2$. At large momentum transfer, the hard pomeron couples predominantly to individual partons in the proton [36]. Thus, the cross section may be factorized into a product of the parton level cross section and the parton distribution functions:

$$\frac{d\sigma(\gamma p \to VY)}{dtdx} = (\frac{81}{16}G(x,t) + \sum_f [q_f(x,t) + \bar{q_f}(x,t)])\frac{d\sigma(\gamma q \to Vq)}{dt} \qquad (35)$$

where $G(x,t)$ and $q_f(x,t)$ are the gluon and quark density of the proton. The struck parton in the proton, initiating a jet in the proton hemisphere, carries the fraction x of the longitudinal momentum of the incoming proton.

The wave function of the J/ψ shares the longitudinal momentum of the vector meson equally between the quark and the anti-quark. This non-relativistic approximation is valid for heavy vector mesons. In this approximation, the vector meson retains the helicity of the photon such that the s-channel helicity conservation (SCHC) is satisfied.

At sufficiently low x (i.e. large values of W) the gluon ladder is expected to include contribution from BFKL evolution as well as from standard DGLAP evolution. The pQCD models with the gluon ladder exchange predict an approximate power-like behaviour for the $|t|$ dependence of the cross section. They predict also, in contrary to two gluon exchange a rise of the differential cross section with increasing energy.

The theoretical models describing the proton-dissociative vector meson production, using different evolution equations, are presented in more detail in Sec. 8. The predictions of these models are compared with the result of the present analysis and previous ZEUS measurement [7].

2 The HERA collider and the ZEUS detector

The **H**era **E**lektron **R**ing **A**nlage HERA is the first and the only *ep* collider in the world. It is located at DESY (Deutsche Elektronen Synchrotron) in Hamburg, Germany.

HERA was approved in 1984, and the construction of the accelerator was completed in 1990. First electron-proton collisions were achieved in October 1991. Operations for

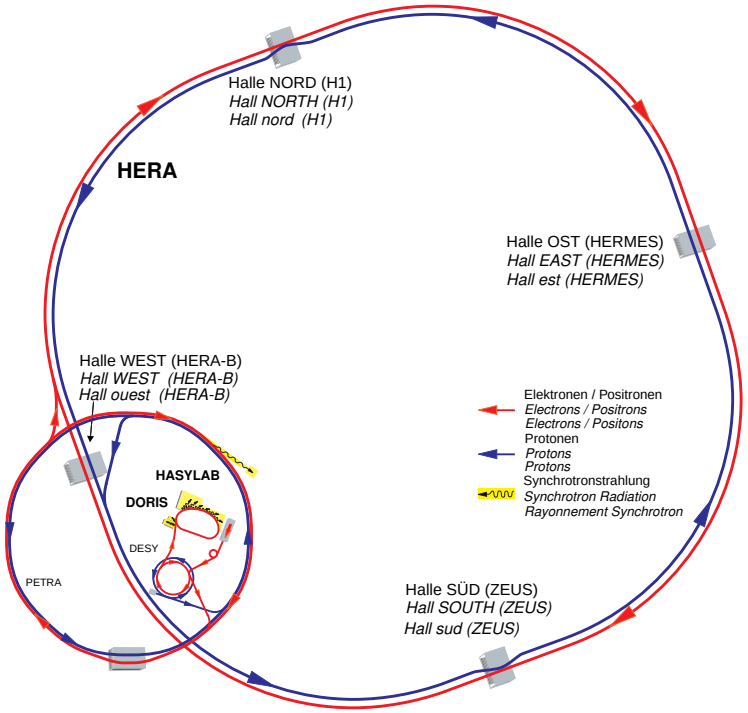

Figure 8: *The HERA storage ring and its pre-accelerator complex. Four experiments are located in the experimental halls South (ZEUS), West (HERA-B), North (H1), and West (HERMES).*

physics started in the summer of 1992.

HERA is designed to collide electrons (positrons) accelerated up to an energy of 30 GeV with protons of 820(920) GeV yielding a center of mass energy of $\sqrt{s} \approx \sqrt{4E_eE_p} \approx$ 300 GeV.

The accelerating system is placed in the 6.34 km long tunnel, 10-30 m underground and consists of two storage rings: one for the electrons and one for the protons. Each storage ring is made of four 90^o arcs connected by 360 m straight segments. Four experiments

have been installed in the middle of straight sections along the HERA ring: the two main experiments ZEUS and H1 (South and North experimental halls, respectively) and two fixed-target experiments HERMES (East Hall) and HERA-B (West Hall).

In the experimental area of ZEUS and H1 the beams are made to collide head-on at zero crossing angle giving the possibility of study the *ep* interactions. The two other experiments are using only one of the beams: HERMES investigates the nucleon spin structure by means of longitudinal polarized electron beam colliding with an internal polarized gas target (hydrogen, deuterium, ^{3}He), while HERA-B was designed to use the beam halo protons scattering off wire targets to produce B-mesons for the study of CP violation in the $B\overline{B}$ system.

The acceleration of the electron and proton beams is done in few steps. Protons are obtained from negatively charged hydrogen H^- brought up to an energy of 50 GeV in the LINAC by stripping electrons off ions. Next protons are injected into the proton synchrotron DESY III where they are accelerated up to 7.5 GeV before being transferred to PETRA. As their energy reaches 40 GeV, they are moved from PETRA to the HERA proton storage ring to obtain the final energy [2] of 820 GeV.

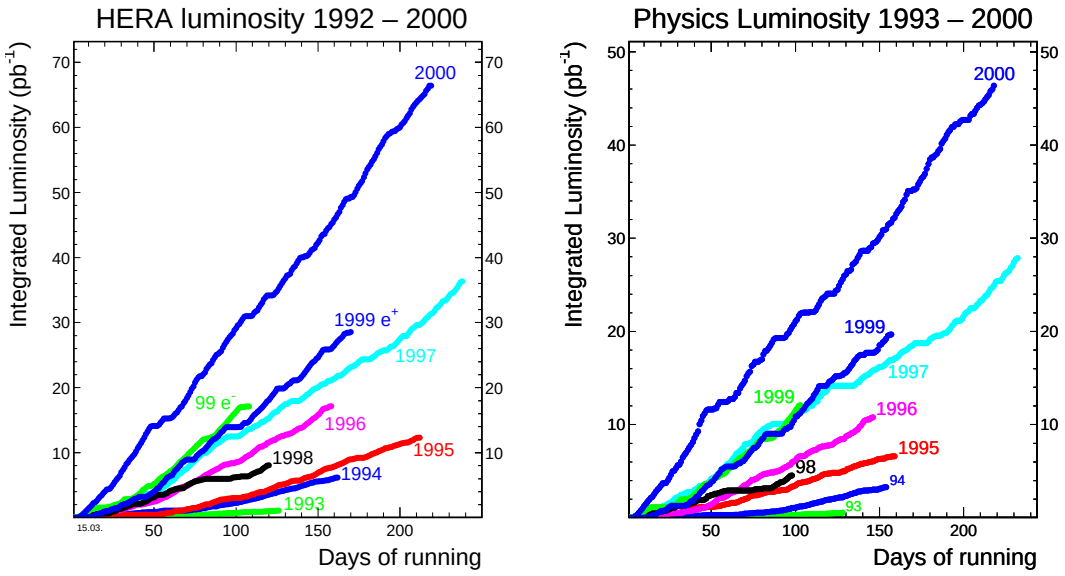

Figure 9: *The integrated luminosity delivered by HERA (left) and collected by the ZEUS detector (right) in the 1993-2000 running periods.*

The injection of electrons starts in a 450 MeV LINAC II. Further they are accumulated in the storage ring PIA, from where, in bunches, they are transferred to DESY III, where

[2] In the 1998/1999 running period the proton energy in HERA was increased to 920 GeV.

their energy is brought up to 7.5 GeV. The next step is PETRA, here electrons reach an energy of 14 GeV and are injected into the HERA lepton storage ring and accelerated to the energy of 27.5 GeV.

Finally HERA is filled with 210 bunches of electrons and protons spaced by 96 ns. In normal running not all of the bunches are filled: unpaired 'pilot' bunches are used to estimate the beam gas background. There are also empty 'pilot' bunches (neither proton nor electron bunches) enabling the measurement of the cosmic ray background.

The integrated luminosity delivered by HERA and collected by the ZEUS detector in the 1993-2000 running periods is shown in Fig. 9.

2.1 Overview of the ZEUS experiment

ZEUS is a general purpose magnetic detector designed to study the broad area of electron-proton scattering process. The full description of the ZEUS detector can be found elsewhere [37].

The ZEUS detector was commissioned in the spring of 1992 and since then it has been undergoing continuous changes.

The coordinate system in ZEUS is orthogonal and right-handed: the x axis points the centre of HERA, y axis points upwards, and z axis points towards the direction of the incoming proton beam. The $+z$ direction is called $forward$ and $-z$ as $backward$ direction. The nominal interaction point is at $z = 0$. The polar angle θ, defined with respect to the z axis is 0^o for the proton beam and 180^o for the electron beam. The azimuthal angle ϕ is measured with respect to the x axis.

The ZEUS detector consists of the main detector located around the nominal interaction point and several small detectors along the beam pipe in the forward and backward direction. In Fig. 10 the cross section of the main detector is shown.

The detector is asymmetric: larger and deeper in the forward direction because of the asymmetry of the ep final system caused by a large difference in energies of incoming particles. Its dimensions are 11.6 m $\times$ 10.6 m $\times$ 20.0 m (x, y, z) and the total weight is about 3600 tones.

Initially, the closest to the beam pipe was the Vertex Detector (VXD) removed during the 1995 upgrade. So, the most important tracking device is the Central Tracking Detector (CTD). The tracking system is completed in the forward direction by three sets of planar drift chambers (FTD) with Transition Radiation Detector (TRD) in between (together labeled FDET in Fig. 10) whereas in the rear direction one planar drift chamber with three layers is installed. The tracking system is surrounded by a superconducting solenoid

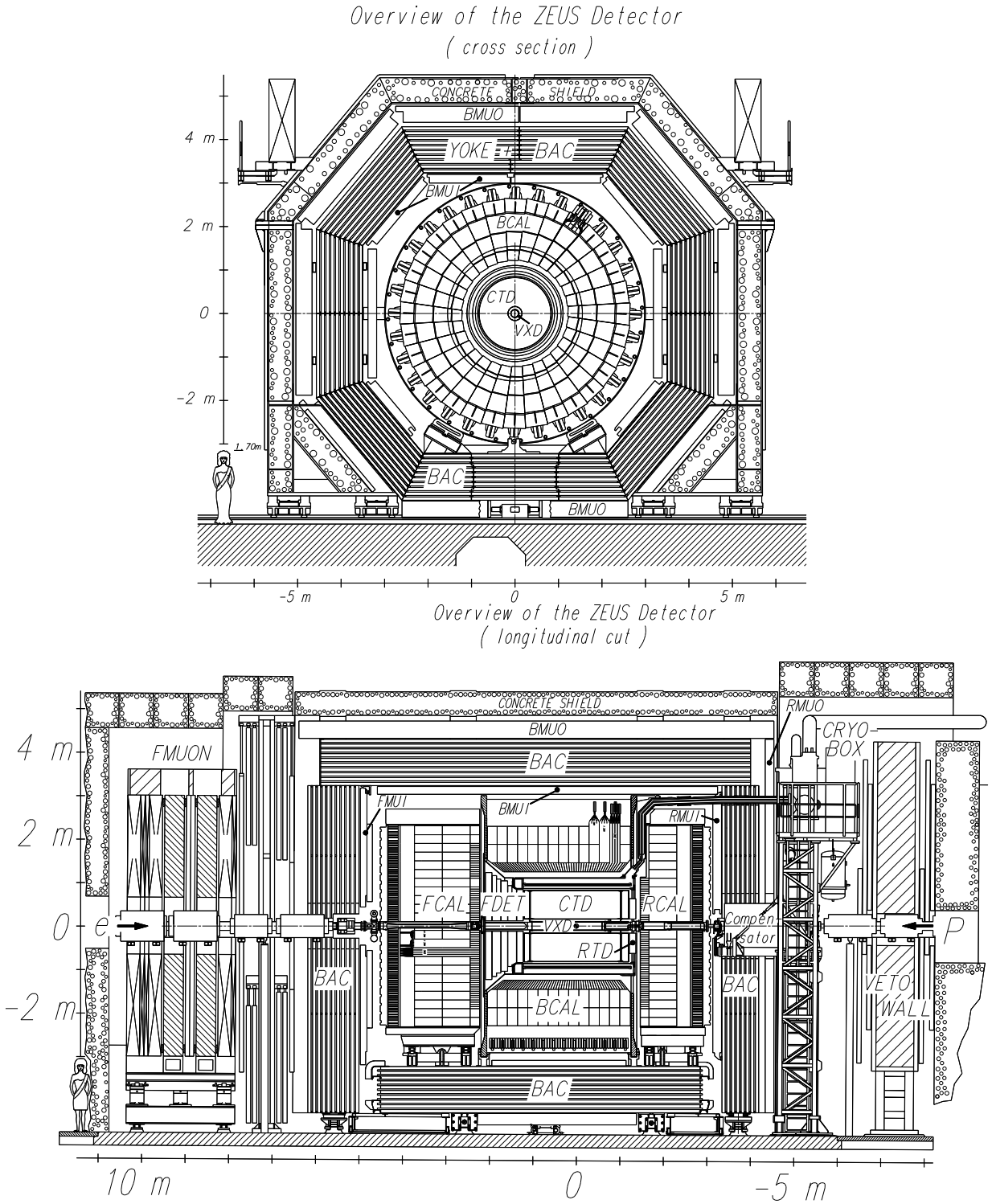

Figure 10: *The ZEUS detector: cross section (upper) and longitudinal cut (lower).*

providing the magnetic field of 1.43 T. The high resolution uranium calorimeter (CAL) encloses the tracking detectors. The CAL is divided geometrically into forward (FCAL),

barrel (BCAL) and rear (RCAL) sections.

To improve the discrimination between electromagnetic and hadronic showers for low energy particle ($< 5\,\text{GeV}$), silicon diodes have been added in the forward and rear parts of the calorimeter (hadron-electron separator, HES). The CAL is surrounded by an iron yoke, which provides a return path for the solenoid magnetic field flux and is an absorber for the backing calorimeter (BAC), which measures energy leakage from the main calorimeter.

As the yoke is magnetized to 1.6 T by the cooper coils it is used to deflect muons. In order to measure the momentum of the muons limited streamer tubes are mounted inside and outside of the barrel (BMUI,BMUO) and the rear (RMUI, RMUO) iron yoke. Since the particle density in the forward direction is very high the forward muon chambers are constructed in another way; inside the iron yoke there are limited streamer tubes (FMUI) and outside are mounted the drift chambers and limited streamer tubes (FMUO).

A small angle rear tracking detector is situated between the RTD and the RCAL covering a radius of ~ 34 cm around the beam pipe. The Beam Pipe Calorimeter (BPC), a small electromagnetic sampling detector is installed close to the beam in the beam hole in the RCAL. It is supplemented by the Beam Pipe Tracker (BPT) which consists of two silicon microstrip detectors. To extend the angular calorimetric coverage, in 1998, a small Forward Plug Calorimeter (FPC) was installed in a FCAL beam hole.

There are additional detectors located outside the main detector. In the forward direction the Proton Remnant Tagger (PRT), a lead/scintillator counter is placed at $z = 5\,\text{m}$ and $z = 24\,\text{m}$, which provides an information about the hadronic final state. The six stations of the Leading Proton Spectrometer (LPS) are located at a distance from 24 m to 90 m away from the interaction point to measure scattered protons with low transverse momentum ($< 1\,\text{GeV}$). At $z = 106\,\text{m}$ the Forward Neutron Calorimeter (FNC) is installed to detect neutrons at small forward angles.

In the backward direction two small electromagnetic calorimeters (LUMI-e and LUMI-γ) are placed at $z = -35\,\text{m}$ and $z = -107\,\text{m}$ to measure bremsstrahlung events ($ep \to e\gamma p$) necessary for the determination of the luminosity and also used for tagging photoproduction events. The other detectors, able to measure the scattered positron under very small angles are placed at $z = -8\,\text{m}$ and $z = -44\,\text{m}$ and are sensitive for energy range of $1 < E_{e'} < 3\,\text{GeV}$ and $21 < E_{e'} < 26\,\text{GeV}$, respectively.

2.2 The Central Tracking Detector

The Central Tracking Detector (CTD) [38–40] is placed in the centre of ZEUS detector around the interaction point. The CTD provides a high precise measurement of the

direction and momentum of charged particles. In addition, the particles can be identified by estimation of the energy loss, dE/dx.

The CTD is a cylindrical drift chamber surrounded by a superconducting magnet which create an axial field of 1.43 T. The drift chamber with the inner and outer radius of 18.2 cm and 79.4 cm, respectively and the 205 cm length is filled with the gas mixture of argon, CO_2, and ethane and covers the polar angle range of $15^o < \theta < 164^o$ and the full azimuthal angle. The device consists of 72 radial layers organized in 9 superlayers, oriented axial and stereo (inclination of about 5^o with respect to the beam line) and allowing both R-ϕ and z coordinate measurement. The interaction vertex is measured with a typical resolution along and transverse to the beam axis of 0.4 cm and 0.1 cm, respectively.

2.3 The Uranium Calorimeter

The uranium calorimeter (CAL) [41–43] is a compensating sampling calorimeter consisting of the layers of depleted uranium and plastic scintillator. The thickness of the layers is chosen in order to have linear and equal response to hadrons and electrons up to the highest energies. The calorimeter provides precise energy measurements for hadrons and jets, an angular resolution for jets better than 10 mrad, the ability to discriminate between hadrons and electrons using their different energy depositions and a time resolution of 1 ns. The relative energy resolution measured in the test beams was $\sigma(E)/E = 0.18(0.35)/\sqrt{E}$ for electrons (hadrons).

The UCAL is a 4π detector with the exception of the holes located in the centre of forward and rear part, which are occupied by the beam pipe, and is divided into three main parts covering different angular regions. The details are summarized in Tab. 1. Each part of the calorimeter is further subdivided into towers with dimensions 20 cm × 20 cm (transverse to the beam). The towers are segmented longitudinally into inner electromagnetic section (EMC) and two (one for RCAL) hadronic section (HAC1 and HAC2); both sections are organized into cells (larger for the HAC sections), see Fig. 11. Each cell is read-out at two sides by wavelength shifters which are coupled to photomultiplier tubes (PMTs).

	FCAL	BCAL	RCAL
θ-range	2.2^o-39.9^o	36.7^o-129.1^o	128.1^o-176.5^o
η-range	-4.0–1.0	-1.1-0.74	0.72-3.49
radiation length X_0	25.9	24.6	24.3
absorption length λ	7	5	4

Table 1: *The CAL angular acceptance and longitudinal depth.*

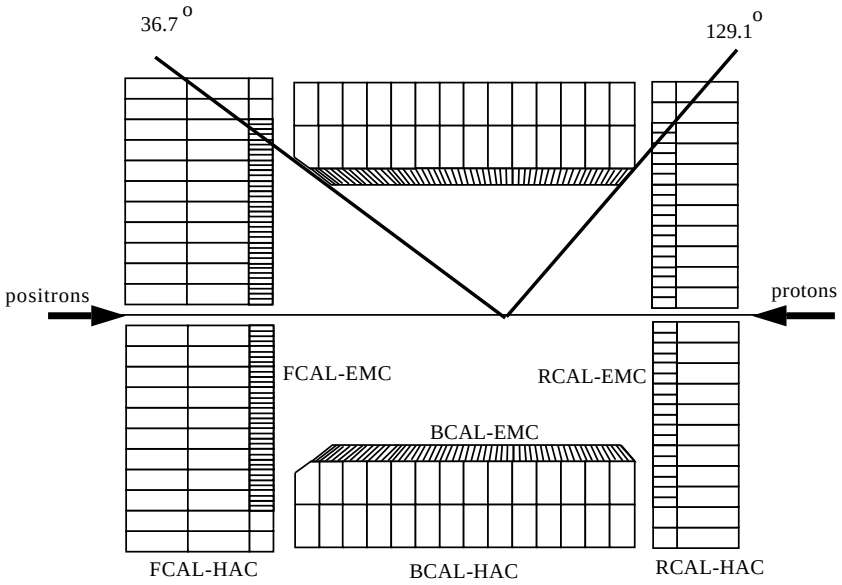

Figure 11: *A schematic picture of the calorimeter. The different EMC and HAC sections are shown, also the angular coverage of the BCAL is indicated.*

2.4 The Proton Remnant Tagger

The Proton Remnant Tagger (PRT) [44] is used to detect charged particles emitted at very small angles, that escape the central detector through the forward beam pipe. The detection of those particles allows to distinguish events with an elastically scattered proton from a proton dissociative events.

The PRT consists of seven pairs of lead-scintillator counters surrounding the beam pipe in a forward direction. Two pairs of the counters (PRT1) are located at $z = 5$ m and next five pairs (PRT2) at $z = 24$ m, tagging particles in the angular range $6 < \theta < 26$ mrad and $1.5 < \theta < 8$ mrad, respectively. The counters in a pair are of equal size covering the same area. The schematic picture of the PRT tagger system is presented in Fig. 12.

The signals observed in a pair in coincidence allow high energetic particles to be detected, while suppressing backgrounds due to soft particles, including synchrotron radiation photons.

2.5 Luminosity measurement

A precision measurement of luminosity in the ZEUS experiment is done according to the following formula:

$$R = \mathcal{L} \times \sigma, \tag{36}$$

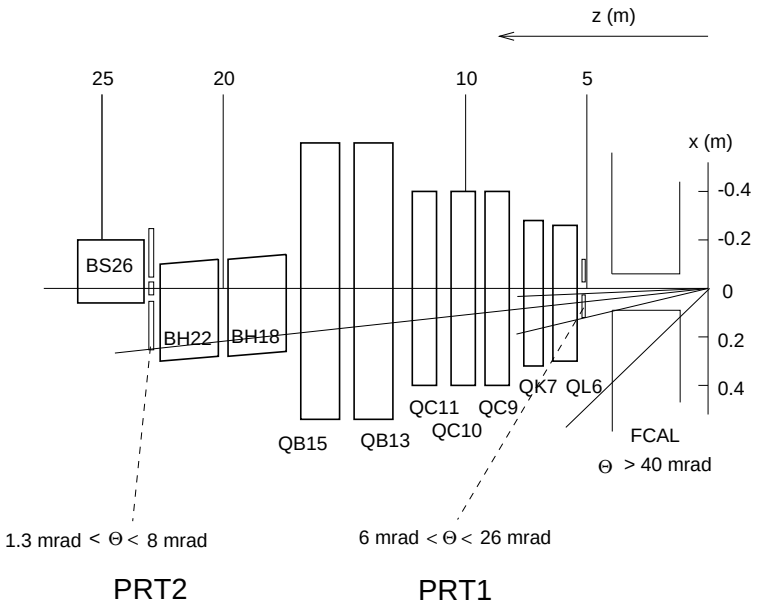

Figure 12: *The position of PRT1 and PRT2 detectors with respect to HERA magnets and their angular coverage.*

where R is the rate of events per second for a given process with the cross section σ in cm^2 and the standard unit of measured luminosity $\mathcal{L}$ is cm$^{-2}s^{-1}$. In order to measure the luminosity one chooses process for which the cross section is very well known from theory and is large enough to allow for a statistically precise measurements. In the case of HERA this process is the bremsstrahlung process $ep \to ep\gamma$ [45,46], which cross section is known with accuracy of 0.5%. A large background with almost the same experimental signature originates from electron bremsstrahlung on the residual gas. By measuring bremsstrahlung rate of unpaired electron bunches together with a measurement of the current in both paired and unpaired bunches the background can be substracted statistically.

Initially, the luminosity was measured via coincidence of a high energy photon and a scattered electron, but because of excellent background conditions and well controled photon acceptance, it was decided to use only photons for a precise luminosity determination. Since 1992 the luminosity calculations are based only on the measurement of high energy bremsstrahlung photons, while the measurement of scattered electrons is used for systematic checks and also in tagged photoproduction.

The LUMInosity monitor (LUMI) [47] consists of two components: the photon detector (LUMI-γ) and the electron detector (LUMI-e) (see Sec. 2.6). The schematic picture of the LUMI system is presented in Fig. 13.

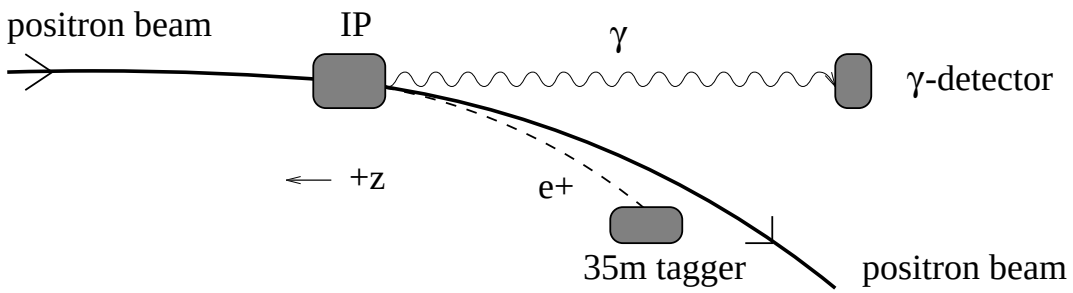

Figure 13: *The luminosity detectors system consists of two components: the photon detector at −107 m (LUMI-γ) and the electron tagger at −35 m (LUMI-e).*

The bremsstrahlung photons propagate inside the proton beam pipe leaving it through a Cu-Be window placed at $z = -92\,\mathrm{m}$. Photons, which are emitted under angles $\theta_\gamma < 0.5\,\mathrm{mrad}$ with respect to the electron beam direction, can be detected by a lead/scintillator sampling calorimeter (LUMI-γ) placed at $z = -107\,\mathrm{m}$. It contains also the position detector, which allows to recontruct the photons' impact position with a resolution of 2 mm. The detector is shielded by a $3.5X_0$ carbon/lead filter from synchrotron radiation. With this filter the energy resolution of the calorimeter of $25\%/\sqrt{E}$ (E is measured in GeV) was achieved in the test beam measurements.

2.6 The electron tagger at 35m

The electron detector, called often photoproduction tagger at 35 m (PT35m), is the part of the LUMI monitor. It is a lead/scintillator sampling detector, $22X_0$ deep, read out by light guides and photomultipliers. LUMI-e contains the electron position detector, able to measure the position of tagged electron by means of scintillator fingers located at a depth of $7\mathrm{X}_0$. The sampling step is 1 X_0 and is uniform through the calorimeter. The geometric acceptance of the electron detector is determined by the magnets and the beam pipe apertures: electrons that have lost part of their energy radiating a bremsstrahlung photon, or have been scattered at a very small angle at the IP, are deflected from the nominal beam orbit by the magnetic field of HERA. These electrons leave the beam pipe through an exit window (0.085 X_0) located at $z = -27$ m and are detected by the LUMI-e which is located at $z = -35$ m. The transversal dimensions of the calorimeter are $25\,\mathrm{cm} \times 25\,\mathrm{cm}$. The 35m tagger measures electrons scattered at angles below 6 mrad with efficiency greater than 70 % for $0.35\mathrm{E}_e < \mathrm{E}_{e'} < 0.65\mathrm{E}_e$ (GeV).

The LUMI-e calorimeter is used to detect photoproduction events, where scattering angle is very small, in the interval $10^{-7} < Q^2 < 0.02\,\mathrm{GeV}$.

2.7 The muon detectors

Muons behave as minimum ionizing particles which easily penetrate the calorimeter if they have an energy of more than a couple of GeV. The ZEUS detector is surrounded by chambers to identify and measure the momentum of these muons. The iron yoke making up the BAC calorimeter is magnetized with a toroidal field of about 1.5 T, and a momentum measurement is performed by measuring the angular deflection of the particle traversing the yoke. In the barrel and rear region, there are muon detectors composed of two layers of chambers - BRMUI/BRMUO and RMUI/RMUO, using Limited Streamer Tubes (LST), placed inside and outside the yoke. This structure of the muon detectors allows an accurate measurement of the position of the track at the exit of the calorimeter and a momentum propagation by means of the yoke magnetic field. The muon chambers allow to distinguish between background interactions (events) arising from cosmic ray, beam halo muons [3] and events originating in the interaction region.

The forward muon spectrometer (FMUON) provides an independent momentum measurement of muons as well as improves the rejection of muons from background sources. It uses two toroidally magnetized iron regions interleaved with drift chambers, limited streamer tubes and time-of-flight counters.

2.8 Other detector components

In addition to the detector components described above, two other components are relevant to this analysis trough their role in the trigger: the Veto Wall and the C5 counter.

The Veto Wall [37] is an iron wall placed at about $z = -7.5$ m. It protects the detector by stopping particles created by interactions of the beam halo with the beam pipe material. The iron wall is 87 cm thick and is instrumented with scintillators on both sides. It acts as a veto against events produced by particles passing through the wall.

The C5 detector [48] consist of two planes of scintillator layers interleaved with layers of tungsten and placed around the beam pipe at $z = -1.2$ m. It detects particles from beam-gas events and its signal is used as a veto in the trigger.

2.9 The ZEUS Data Acquisition System

The bunch crossing time at HERA is 96 ns giving an event rate of about 10 MHz. This translates into more than 5 TB of data per second. A large fraction of these are the

[3] Beam halo muons are the result of interactions between protons and gas upstream of the ZEUS detector. Some of the particles (pions, kaons) produced in these interactions decay in flight to muons.

events coming from proton beam gas interactions, proton beam halo and cosmic ray induced events; the rest are the real *ep* colision data. In order to distinguish and read out physics events the three level trigger and the data acquisition (DAQ) system has been developed. The trigger system reduces the total rate of accepted events to a few Hz.

Each component has its own electronics and the first level trigger system. During ~ 5 μs after the bunch crossing each component makes its own FLT decision. This informations are sent to the Global First Level Trigger (GFLT), from which the decision on wheather an event is accepted or not is issued to all detector components 4.4 μs later. The GFLT reduces the amount of data to ~ 1 kHz.

If the GFLT decision is positive the data are transferred to the Second Level Trigger (SLT). The local SLT information is sent to the Global Second Level Trigger (GSLT) which then computes the global decision and gives the answer to each component. The GSLT is designed to achieve a reduction of data to 100 Hz.

For an event accepted by the GSLT data from each component are transferred to the Eventbuilder which combines and formats all the components' data into one data set. This data set is accessible to the Third Level Trigger (TLT) which reconstructs the event online. The TLT finally reduces the input rate to a few Hz. Events accepted by the TLT are registered on magnetic tape.

3 Monte Carlo

3.1 Monte Carlo simulation

The Monte Carlo (MC) simulation of the observed data is a powerful tool which allows to make direct comparison between theory and the experiment. It is also used to correct the geometrical acceptance of the detectors and is useful in the determination of the selection cuts in the data or for separating the signal from background.
The MC programs are used to generate events according to the chosen theoretical model and to simulate the detector response. The output of the MC generator is the list containing the four-momenta of the final states, produced according to the model. Then the events are passed through the MOZART [48] program (*MOnte carlo for Zeus Analysis, Reconstruction and Trigger*), which is a full simulation of the ZEUS detector. The structure of the detector is simulated using the GEANT [49] package. The output is in ADAMO tables [50] format, the same as for the real data. The next step is the ZGANA package [51], which is a complete simulation of the three-level trigger system of ZEUS, so the MC is treated in the same way as data. The events which pass the selection criteria of a physics filter are flagged and stored in the form of a Data Summary Tape (DST).

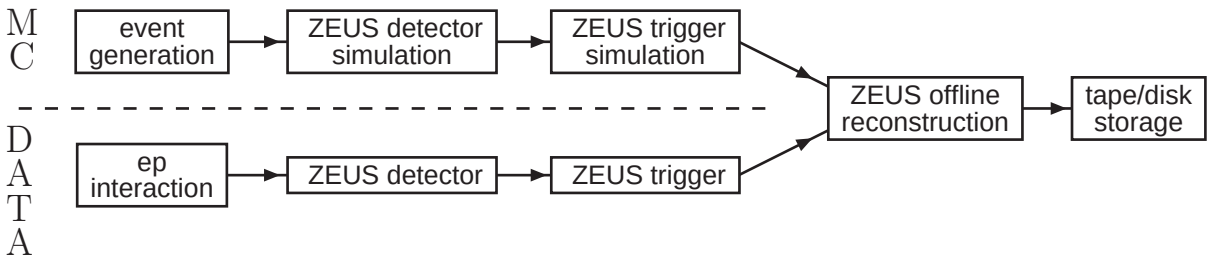

Figure 14: *Overview of the data and MC simulation chain in the ZEUS experiment.*

3.2 MC generators

In this section the MC generators which have been used to simulate the proton-dissociative J/ψ production and the Bethe-Heitler process are briefly described.

EPSOFT

EPSOFT [52, 53] is a Monte Carlo program for simulating soft diffractive and non-diffractive photon-proton interactions. It has been developed in the framework of HER-

WIG [54] and tuned specifically for photoproduction in diffractive events.

In this analysis the EPSOFT generator was used to simulate the vector meson photoproduction with the proton dissociation $\gamma p \to VY$.

The cross section for this process is described according to

$$\frac{d^2\sigma(\gamma p \to VY)}{dt dM_Y^2} \sim \sigma_{ALLM}(\gamma p) \cdot \frac{e^{-b|t|}}{M_Y^\beta} \tag{37}$$

where b and β are free parameters. The $\sigma_{ALLM}(\gamma p)$ is the cross section for scattering photons on protons calculated from the ALLM parameterization [55]. It relies on triple-Regge formalism and has been fitted to the available photoproduction and Deep Inelastic Scattering (DIS) data. In the MC sample generated for this analysis $\beta = 2.0$ and the t distribution was parametrized as $e^{-b|t|}$ with $b = 1.0\,\mathrm{GeV}^{-2}$. The EPSOFT MC was generated under the condition $M_Y^2 < 0.1W^2$.

The vector meson mass was assumed to be a fixed constant. The multiplicity distribution for charged and neutral hadrons from the decay of the nucleonic system Y comes from a fit to ZEUS photoproduction data and hadron-hadron results.

GRAPE

The reaction $\gamma p \to eYl^+l^-$ is simulated using GRAPE [56] which is a Monte Carlo event generator for dilepton production in ep collisions.

The cross section calculation is based on the exact matrix elements. The Feynman amplitudes were generated by the automatic calculation system GRACE [57]. The interaction at the proton vertex is parametrized by an electromagnetic structure function, based on the parameterization taken from fits to the experimental data from [58] (for proton resonance region $M_Y < 2\,\mathrm{GeV}$) and from [55] (for continuum region $M_Y > 2\,\mathrm{GeV}$). The hadronic final state is generated using the MC event generator SOPHIA [59]. The corresponding processes are shown in Fig. 15. No radiative corrections were included into the simulation.

The generator was used to study the possible background in two lepton spectrum from J/ψ decay. These events were generated in a restricted kinematic range of $t < 100\,\mathrm{GeV}^2$, $M_Y < 60\,\mathrm{GeV}$, $120 < W < 280\,\mathrm{GeV}$, $Q^2 < 0.02\,\mathrm{GeV}^{-2}$, $p_T(lepton) > 0.1\,\mathrm{GeV}$, $5^o < \theta < 179^o$, where θ is the polar angle of the produced lepton in the laboratory frame. The corresponding theoretical cross sections are listed in Tab. 2.

mode	cross section (pb)
e^+e^-	209.15 ± 0.12
$\mu^+\mu^-$	194.74 ± 0.05

Table 2: *The theoretical cross sections for lepton pair production in the reaction* $\gamma p \to eYl^+l^-$ *from GRAPE generator.*

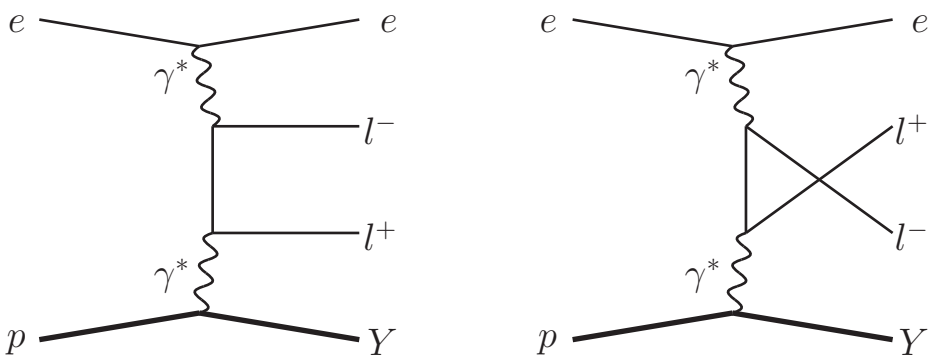

(a) Two-photon Bethe-Heitler

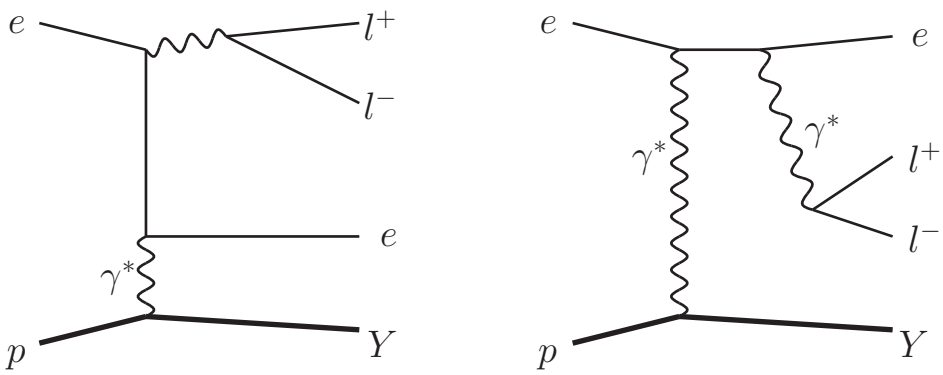

(b) Internal Photon Conversion

Figure 15: *Feynman diagrams included in GRAPE MC.*

4 Event reconstruction

4.1 Event characteristics

The subject of this analysis is the proton dissociative J/ψ photoproduction in the reaction $ep \to e\, J/\psi\, Y$, studied in the two leptonic decay channels: $J/\psi \to e^+e^-$ and $J/\psi \to \mu^+\mu^-$. The analyzed data is a subset of the photoproduction sample characterized by high W and high $|t|$ range. The main features of these events are the following: two leptons originating from one vertex, having a track or tracks found in the CTD, no activity in the BCAL/RCAL, except that associated with these decay leptons and a scattered electron in the PT35m. The proton dissociative events are recognized as these with a hit in the PRT or an activity in the FCAL above the noise level. The scattered electron detected in the PT35m ensures low virtuality Q^2 of the exchanged photon.

4.1.1 The event topology

The analyzed data sample was divided into three classes according to the number and the reconstruction quality of the tracks measured in the CTD:

a *two track* event - two tracks of high quality, which crossed at least three superlayers [4] are within the CTD angular acceptance and are pointing to the vertex. The momentum reconstruction of a track is based on the CTD information. There are two energy deposits, above the noise level in the part of the CAL covered by the angular acceptance of the CTD, in the BCAL or the RCAL, which are matched to the tracks.

b *quasi-one track* event - there are two tracks from the vertex, one of the high quality, while the second is reconstructed rather poorly (the number of crossed CTD superlayers is less than three). This class of events are treated as the *one track* events, and the reconstruction is performed as described below.

c *one track* event - there is only one good track pointing at the vertex and two energy deposits in the calorimeter, in the BCAL or the RCAL, above the noise level. These energy deposits come from the decay lepton candidates. One of them is within the angular acceptance of the CTD and is matched to the track, the other is in the RCAL near the beam pipe hole. The complete reconstruction of such event is derived from the energy-momentum conservation law. The needed information for it is the momentum of the track reconstructed from the CTD, the position of the unmatched cone island in the RCAL and the energy of the scattered electron in PT35m.

[4] Such a track is further called *good track*

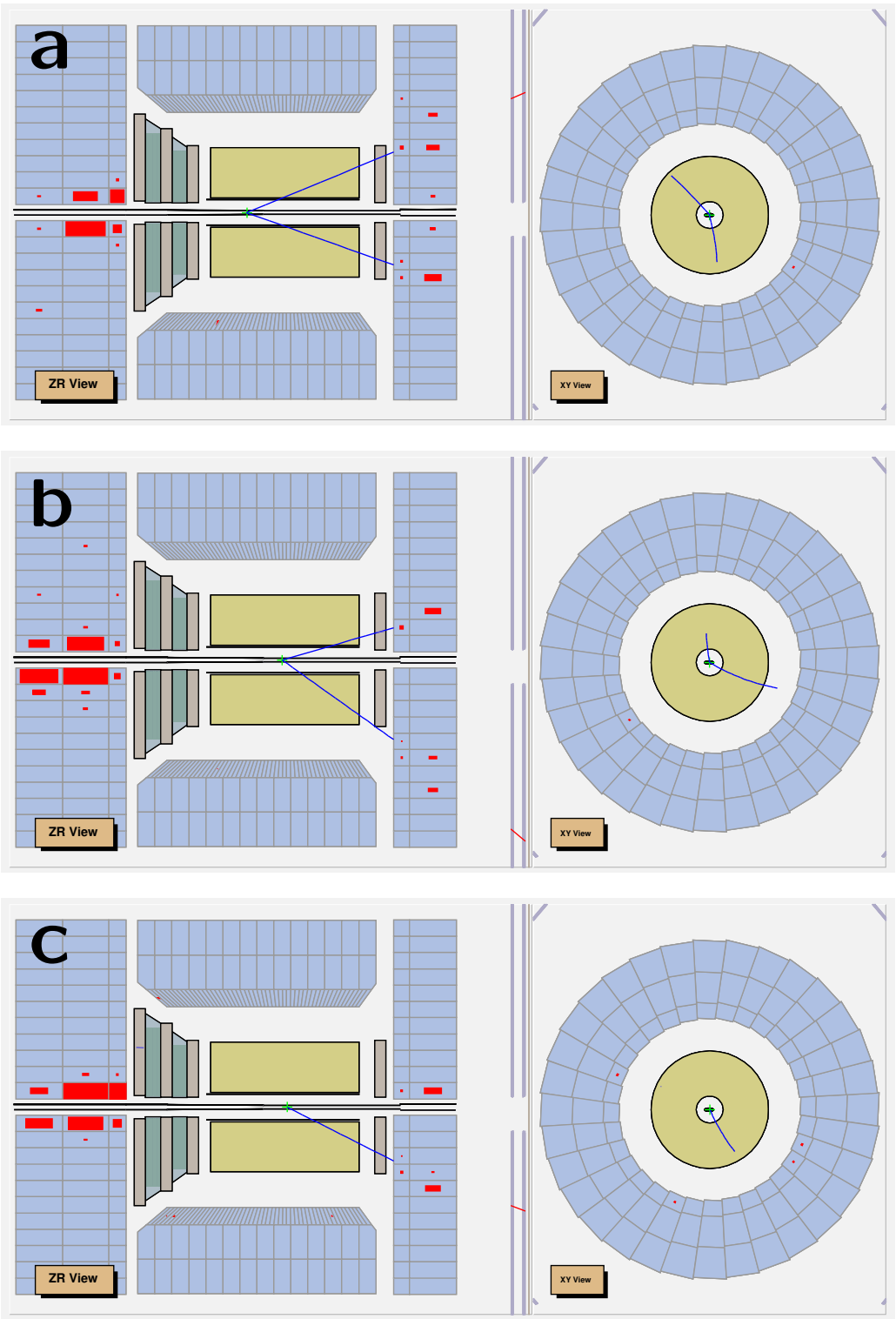

Figure 16: *The proton dissociative J/ψ events from the data sample, displayed with the ZEUS event display ZEVIS. For detailed description see the text.*

Further, the quasi-one and one track event topologies are treated as the same class of events and named simply *one track events*.

All three types of events are illustrated in Fig. 16. These are real events for $J/\psi \to \mu^+\mu^-$ displayed with the ZEUS event display ZEVIS. In the left part of the figure one can identify in the Y-Z view of the ZEUS detector one can identify the tracks reconstructed in the CTD and associate them with the energy deposits in the RCAL and the hits in the muon chambers. In the FCAL the activity coming from the break up of the proton is indicated. The right part of the figure shows the X-Y view of the ZEUS detector with the reconstructed muon tracks. A *two track* event, rather rare in this data sample is shown in Fig. 16a (run number 25872, event number 11936), Fig. 16b presents a *quasi-one track* event (run number 22345, event number 8323). A *one track* event dominant in this data sample is presented in Fig. 16c (run number 27653, event number 17626). The presented events are after all selection cuts, described in this and next paragraphs.

4.2 Event reconstruction

4.2.1 The CTD reconstruction

The CTD tracks and the primary vertex are reconstructed using the VCTRAK package [60]. The track reconstruction in this analysis is based only on the CTD information. (The CTD*only* mode was used, while the CTD regular mode uses the additional information from the RTD and FTD detectors.)

The reconstruction of charged particles in the CTD begins from a track *seed* in an outer part of the CTD, which either comes from a hit in three CTD axial superlayers hit, or a combination of RTD, FTD and CTD hits. Given a track *seed*, a trajectory is extrapolated inwards. The precision of the track reconstruction increases as more axial hits are assigned to the track. The hits from Z-by-timing and stereo layers are added and eventually every track has 3D information. Firstly the longest tracks are reconstructed, then the shorter ones. Reconstructed tracks are fitted to the common vertex. The determination of the primary vertex position is undergoing three stages: tracks that are incompatible with coming from the beam line are rejected. The remaining trajectories are fitted, and used to estimate the vertex position as a weighted center of gravity. This is an iterative process, in which tracks contributing too much to the χ^2 are removed until the quality of the fit is acceptable. The final complete vertex fit gives not only the vertex position, but re-evaluates the direction and curvature of the tracks constrained to it.

The distribution of vertex z-coordinate in data and MC is shown in Fig. 17.

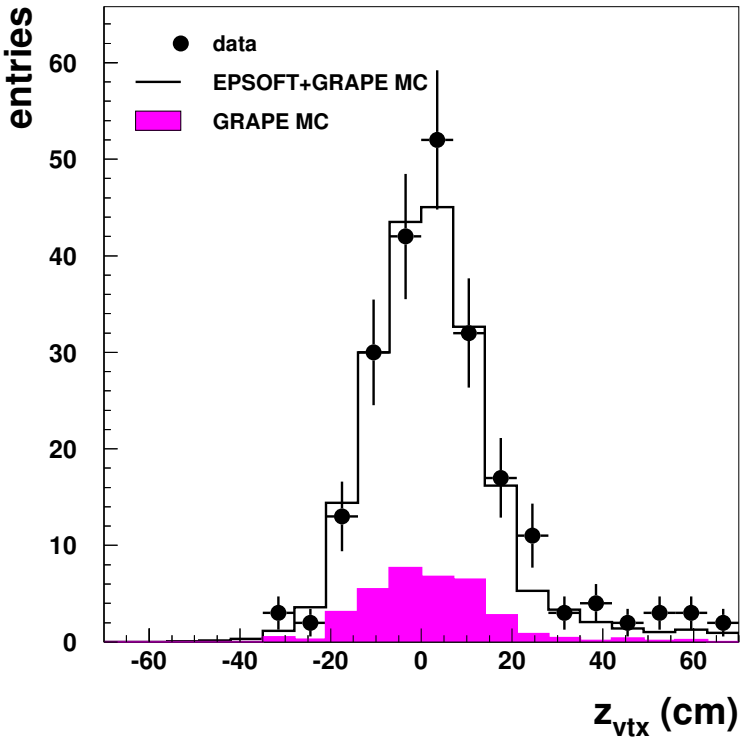

Figure 17: *The comparison of Z vertex distribution in the data (full circles) and MC (solid line). The solid line is the sum of EPSOFT and GRAPE MC. The shaded area indicates the background coming from QED processes (GRAPE MC).*

4.2.2 Detection of the particles in the UCAL

The reconstruction of the calorimeter quantities uses as input the readout of the two PTM's connected to each cell. The energy imbalance, measured from the difference of the response between the two PTM's is used to improve the position reconstruction.

The cell clustering in the CAL, based on angular separation, is performed using a method just like the one in the ZUFO [5] package [61]. For individual parts of the calorimeter, the adjacent cells in EMC, HAC1, HAC2 separately are clustered into cell islands. Cells that match at the corner are not connected, and there is no connection in depth. The resulting cell islands become three-dimensional objects when they are joined into a cone island (see Fig 18). The position of the cone island is subsequently determined through

[5] ZUFO - the hadronic reconstruction method known as Zeus Unidentified Flow Objects

the logarithmic centre of gravity of the shower. The logarithmic weights take into account the exponential falloff of the shower energy distribution from the shower maximum.

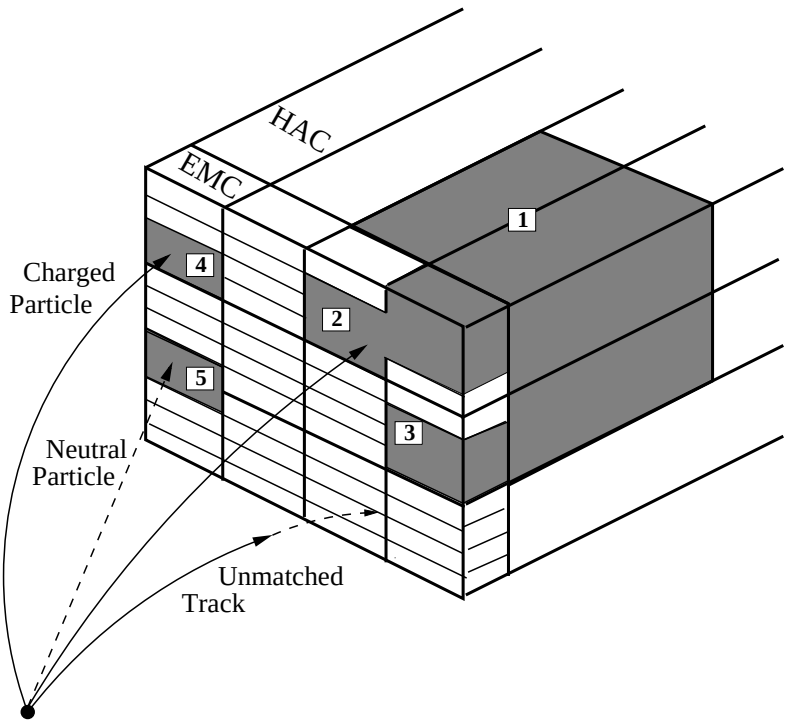

Figure 18: *Schematic representation of a clustering in the CAL. Neighbouring calorimeter cells are clustered into cell islands. This picture shows four EMC cell islands and one HAC cell island. EMC islands 2 and 3 are joined with HAC island 1 to form a cone island. In the next step the cone islands are matched to the tracks.*

The measurement of the hadron energy in the calorimeter is biased by several detector effects. The particle interacts, along its path from the interaction point to the surface of the CAL, with an inactive material (the beam pipe, screws, cables etc.) and looses its energy. This effect should be properly simulated in the MC. Thus, the global energy scale corrections should be done before the hadronic final state reconstruction. In the RCAL region an energy scale factor was determined for individual cells [62] and varies between $5 - 13\%$. In the BCAL the measured energy is scaled up by 5% [63].

The reconstruction of the calorimeter objects is affected by noise in this detector. By using the routine NOISE96s, firstly isolated cells with energies above a threshold are removed (80 MeVfor EMC and 140 MeVfor HAC cells) and next a cut on the maximum imbalance of the two read-out channels of a cell (70 % for cells with energy deposit less than 0.7 GeV) is imposed. In addition cells which were found to be continuously noisy over some time are removed according to run-by-run selection.

4.2.3 Matching of tracks with calorimeter objects

The reconstructed calorimeter objects are matched to the tracks using the Distance of Closest Approach (DCA) method (see Fig. 19). In the DCA algorithm a *good* track, fitted earlier to the primary vertex is extrapolated to the inner surface of the calorimeter and associated to the cone island. The *good* track is the track of high quality, which has traversed at least three superlayers of the CTD. The track matches an island if the distance of closest approach between the extrapolated track and the island position is less than an assumed value, or if the DCA is less than the maximum radius of the island on the plane perpendicular to a ray drawn from the vertex to the island. In this analysis the matching has been done for the whole calorimeter, except for the FCAL region. The cone island and tracks undergoing this procedure were expected to be within the CTD angular acceptance.

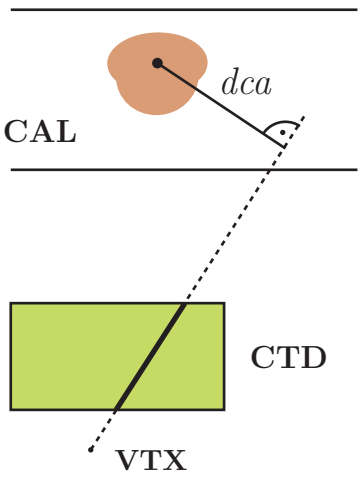

Figure 19: *The Distance of Closest Approach (DCA).*

4.2.4 The reconstruction of proton dissociation system

The products of the proton dissociation are boosted in the forward direction at small angle and may escape undetected in the main calorimeter. The identification of such events is performed by means of information from the PRT or from the energy deposit in the FCAL above the noise level. Only one part of the Proton Remnant Tagger, namely PRT1 component was used for proton remnant identification.

A particle is observed in the PRT if there is a signal of at least 1 m.i.p. in coincidence in both counters of one pair of the PRT paddles. Signal not related to particles coming from the IP were suppressed by a timing cut.

If there was no activity in the PRT an energy deposit in the FCAL was required. The requirement of matching all calorimeter objects to tracks was removed for clusters around the FCAL beam pipe.

type	pulse height [pC]	timing [ns]
DATA	$E_{11} > 1.5, E_{12} > 2.0, E_{13} > 2.0, E_{14} > 2.5$	$-20 < t < 10$
MC	0.015	-

Table 3: *Pulse height and timing cuts for identification of the minimum ionizing particle in the PRT1.*

4.2.5 Detection of the scattered electron

The final state electrons scattered at very small angles were detected in the PT35m after traversing a window in the beam pipe. The geometric acceptance of the PT35m restricts the kinematic range of the detected positrons to approximately $5 < E_{e'} < 20\,\mathrm{GeV}$ and giving the photon virtuality $Q^2 < 0.02\,\mathrm{GeV}^2$.

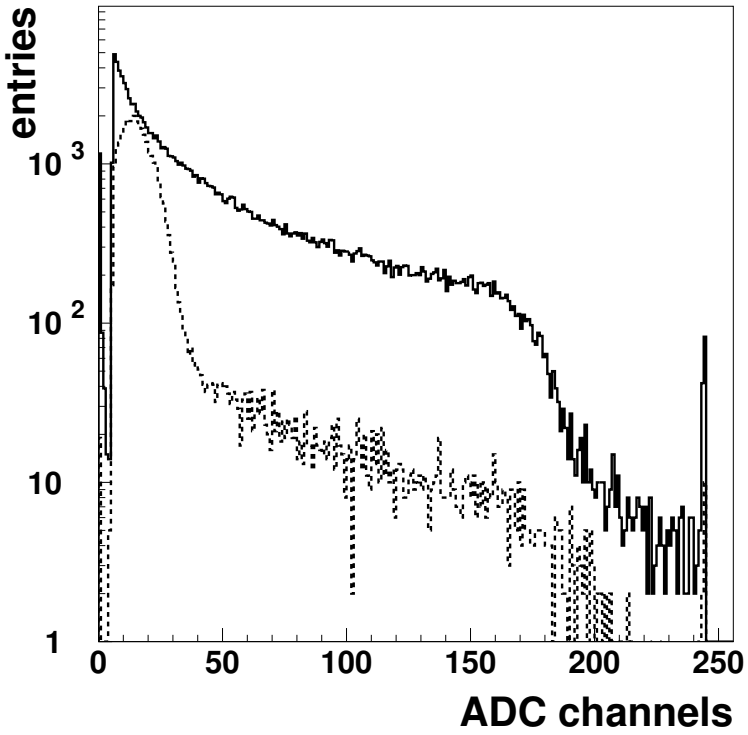

Figure 20: *The energy distribution in the LUMI-γ detector as a function of ADC counts for all events (solid line) and for events tagged in the electron tagger (dashed line).*

The calibration of the electron tagger was done using the bremsstrahlung process in the way described below. The information about the energy of the scattered and tagged electron $E_{e'}$ can be obtained from the relation $E_{e'} = E_e - E_\gamma$, where E_e is the energy of the incoming electron beam and E_γ is an energy of the radiated photon. The raw (averaged) E_γ have to be corrected for the overall gain and the change in ADC pedestals as well as for the non-linearities and fluctuations in the photon detector response. It is then transformed into GeV's using the following parameterization of the average detector

response, $\overline{ADC_\gamma}$, as a function of the 'true' photon energy E_γ [64]:

$$\overline{ADC_\gamma} = c_\gamma[1 + f_{nl}(E_e - E_\gamma)](E_\gamma - E_{filter}) + ADC_\gamma^{ped} \tag{38}$$

where c_γ is the global non-linearity parameter, ADC_γ^{ped} is the pedestal and E_{filter} is the parameter accounting for energy loss in the carbon filter of the LUMI-γ detector. To account for the sampling fluctuations in the LUMI-γ calorimeter the photon 'true' energy is smeared by a Gaussian function with the resolution σ_0. The parameters c_γ, f_{nl}, E_{filter} and σ_0 are obtained from the fits to the data and their values vary between 1996 and 1997. The typical energy distributions of the photon and the tagged positron are shown

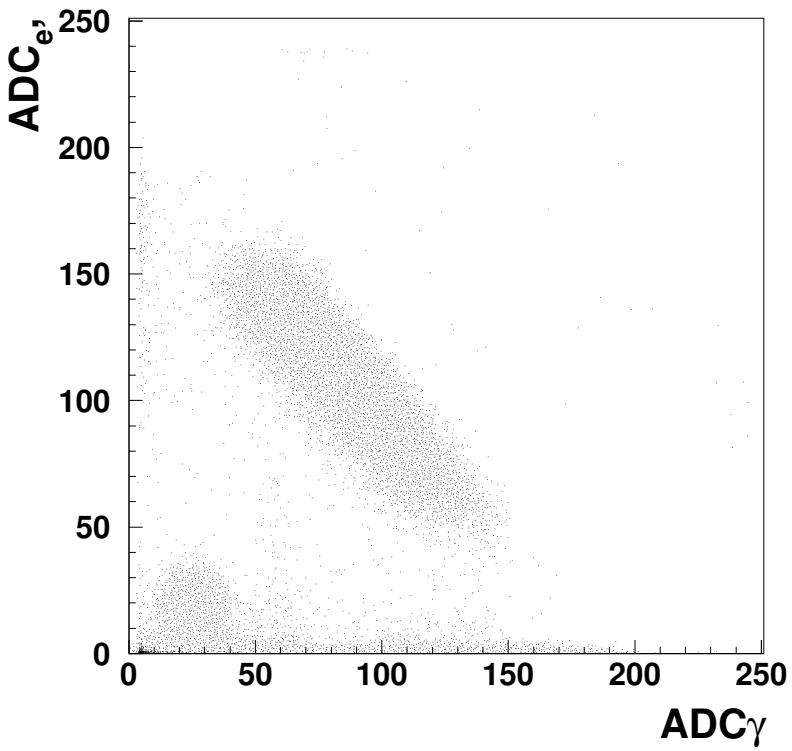

Figure 21: *The correlation of the electron ADC_e' and the photon ADC_γ.*

in Fig. 20. For the correlation between these energies see Fig. 21. The distributions of the sum of the photon and electron signals are used to control the electron detector energy scale and the energy resolution of the two calorimeters.

4.2.6 The reconstruction of the kinematic variables

In the measurement of the reaction $ep \to e\ J/\psi\ Y$ in the photoproduction regime, all relevant kinematic variables have been reconstructed from the decay leptons and/or the energy of the scattered electron as extracted from the tracking detectors, the calorimeter and the electron tagger.

In particular the J/ψ energy, momentum and mass are:

$$P_{iJ/\psi} = P_{il^+l^-} = P_{il^+} + P_{il^-} \qquad (i = x, y, z), \tag{39}$$

$$E_{J/\psi} = E_{l^+l^-} = \sqrt{M_{l^+}^2 + P_{l^+}^2} + \sqrt{M_{l^-}^2 + P_{l^-}^2}, \tag{40}$$

$$M_{J/\psi} = \sqrt{E_{l^+l^-}^2 - P_{l^+l^-}^2}. \tag{41}$$

In tagged photoproduction the photon virtuality Q^2 is in the range between $Q^2_{min} \approx M_e^2 y^2/(1-y) \approx 10^{-9}\,\mathrm{GeV}^2$, where M_e is the electron mass, to the maximum value at which the scattered electron is observed in the tagger, $Q^2_{max} = Q^2_{min} + 4E_eE_{e'}sin^2(\theta_{max}/2) \approx 0.02\,\mathrm{GeV}^2$, where θ_{max} is the maximum scattering angle and E_e and $E_{e'}$ are the energies of the incoming and scattered electron, respectively. The median of the Q^2 distribution is approximately $10^{-7}\,\mathrm{GeV}^2$ so Q^2 can be neglected in the reconstruction of the other kinematic variables.

Assuming $Q^2 \approx 0$ the emitted photon has zero transverse momentum and a longitudinal momentum $P_{z\gamma} \approx -E_\gamma$ in the direction of the incoming proton. From the assumption that the emitted photon is parallel to the beam axis it follows that

$$E_\gamma - P_{z\gamma} \approx 2E_\gamma. \tag{42}$$

According to the conservation of energy and momentum

$$E_\gamma + E_p = E_{J/\psi} + E_{p'}, \tag{43}$$

$$P_{z\gamma} + P_{zp} = P_{zJ/\psi} + P_{zp'} \tag{44}$$

and by subtracting Eq. 43 from Eq. 44 one gets

$$E_\gamma - P_{z\gamma} \approx E_{J/\psi} - P_{zJ/\psi} \approx 2E_\gamma, \tag{45}$$

where the relations $E_p \approx P_{zp}$ and $E_{p'} \approx P_{zp'}$ were used.

The obtained result can be used to reconstruct the γp center of mass energy as

$$\begin{aligned} W^2_{\gamma p} &= (P+q)^2 = M_p^2 + 2P\cdot q - Q^2 \\ &\approx 2E_p(E_\gamma - P_{z\gamma}) \approx 2E_p(E_{J/\psi} - P_{zJ/\psi}), \end{aligned} \tag{46}$$

while the transverse momentum t at the proton vertex is approximated by the vector meson transverse momentum

$$\begin{aligned} t = (P - P')^2 = (P_{J/\psi} - q)^2 &= M^2_{J/\psi} - 2P_{J/\psi} \cdot q - Q^2 \\ &\approx -2E_\gamma(E_{J/\psi} + P_{zJ/\psi}) + M^2_{J/\psi} \\ &\approx -(E_{J/\psi} - P_{zJ/\psi})(E_{J/\psi} + P_{zJ/\psi}) + M^2_{J/\psi} \\ &= -P^2_{TJ/\psi}. \end{aligned} \tag{47}$$

The *two track* event reconstruction is based on the CTD and the CAL only. In this case the equations Eq. 46, Eq. 47 and Eq. 41 were used for W, t and J/ψ mass reconstruction.

In the case of *one track* events to fully reconstructed kinematics of an event, besides the information from the CTD and CAL the energy of the scattered electron must be known. So, for energy conservation at the electron vertex

$$E_\gamma = E_e - E_{e'} \tag{48}$$

using Eq. 45, Eq. 46 can be rewritten in following way:

$$\begin{aligned} W^2_{\gamma p} = (P + q)^2 &= M^2_p + 2P \cdot q - Q^2 \\ &\approx 2E_p(E_\gamma - P_{z\gamma}) = 4E_p(E_e - E_{e'}). \end{aligned} \tag{49}$$

To reconstruct the mass and the t distribution the energy and momentum of both decay leptons is also needed. The four-momentum of one of these leptons is derived from the CTD, while to describe the other lepton the energy of the scattered electron, the four-momentum of the lepton associated to the track and the position of the unmatched object in the CAL is required. The energy of the unmatched lepton is derived from comparison of Eq. 46 and Eq. 49 as follows:

$$E_l = \frac{-A - \sqrt{A^2 \cos^2\theta_l - \frac{1}{4} m_l \sin^2 2\theta_l}}{\sin^2\theta_l}, \tag{50}$$

$$A = E_{tr} - p_{z,tr} - 2(E_e - E_{e'}),$$

where E_l, m_l, θ_l are the energy, mass and position of the energy deposit of the unmatched lepton in the RCAL, while E_{tr}, $p_{z,tr}$ are variables describing the track reconstructed in the CTD.

5 Data selection

The data used in this analysis was collected in 1996 and 1997 from ep interactions with the ZEUS detector at HERA, which operated with a proton beam energy of 820 GeV and a positron beam energy of 27.5 GeV. The data sample corresponds to an integrated luminosity of $30\,\mathrm{pb}^{-1}$ for the electron decay channel and $36\,\mathrm{pb}^{-1}$ for the muon decay channel.

The event selection consists of the following steps:

- the online selection - the tagged photoproduction trigger gives the subsample with both leptonic decay channels and BRMU trigger the subsample containing only muons
- dilepton selection, after removing objects related to the background
- determination of the proton dissociative events
- the limitation of the kinematic region

In the following sections, the detailed description of the event selection is presented.

5.1 Trigger

In this analysis two independent triggers were used, the trigger especially dedicated for tagged photoproduction (PT35m trigger) and the muon trigger (BRMU trigger).

PT35m trigger

The specially designed trigger for tagged vector mesons photoproduction allows to study this process at large values of W. The trigger conditions are described below.

1. The FLT requires a coincidence between the 35m tagger, the LUMI photon detector, the REMC subtrigger and a good track candidate in the CTD. An energy deposit in the 35m tagger should be greater than 5 GeV. The activity in the LUMI photon detector should not exceed 5 GeV to suppress random overlays with the bremsstrahlung events. The REMC subtrigger required a minimum energy deposit of 464 MeV in any of the 8 towers in the RCAL EMC section, excluding the towers immediately adjacent to the beam pipe region.
   In addition events are rejected if the activities in the C5 counter, the Vetowall and the SRTD have a timing inconsistent with that of ep interaction.
2. The SLT included a restriction on the number of tracks and a requirement on the vertex position, if a vertex had been found.

3. The TLT requires one vertex located within the bounds of the nominal IP, $|z_{vtx}| < 66\,\text{cm}$. The number of tracks should be less than 3, and at least one pointing to the vertex. Additionally, the photon-proton energy W, calculated from the CTD is required to be greater than 90 GeV, to reduce the contamination from the $p - gas$ background.

BRMU trigger

To enlarge the statistics and to obtain the events with the muon channel decay the independent muon trigger was used.
The detailed description is given below.

1. At the FLT level the coincidence between a signal from the barrel and/or rear inner muon chambers (B/RMUI), a signal from the CAL, compatible with the minimum ionizing particle (mip) and at least one track in CTD was required. The signal from the muon chambers and from the CAL must be correlated in the time.
2. The SLT: the calorimeter timing cuts are used for beam gas and cosmic rays rejection.
3. At the TLT the *glomu* package [65] searches subsequently for track segments in B/RMUI, good quality tracks and mip clusters in the CAL. If the signals are found, matching between the above components is done.

More details on the B/RMUI trigger configuration can be found here [66].

5.2 Offline selection

The events accepted by online triggering should satisfy also the particular offline selection cuts. In the next paragraphs they are described in details.

5.2.1 General cuts

Only runs in which there were proton and positrons beams, at nominal energies, colliding at the nominal interaction vertex were used. Runs, in which not all relevant detector components were monitored or their status was not good and stable, were rejected ('bad runs' for PRT in 1996, for the muon chambers in 1996-1997). For some runs the PT35m trigger had prescaling set to zero, what also reduced an available luminosity.

5.2.2 The tracking requirements

- The distance of the vertex from the nominal interacting point is restricted to $|z_{\text{vtx}}| \leq 60\,\text{cm}$, $r_{\text{vtx}} = \sqrt{x_{\text{vtx}}^2 + y_{\text{vtx}}^2} < 0.7\,\text{cm}$.

luminosity in pb^{-1}			
-	1996	1997	total
CTD, CAL	10.771	27.845	38.616
PRT1	9.057	27.845	36.902
BRMUI	10.092	26.984	37.076

Table 4: *Integrated luminosity in the 1996-1997 running period for central components (CTD, CAL), for the proton remnant tagger (PRT1) and the muon chambers (BRMUI).*

- There are one or two tracks associated with the vertex, at least one track has hits in three or more superlayers in the CTD, what guarantees a good reconstruction quality. This requirement restricts the polar angle of the track to be within $17^o < \theta < 164^o$. In the case of two track events the tracks have opposite charges.
- The transverse momentum of a track in the region of the CTD acceptance was required to be $p_T > 1.0\,\mathrm{GeV}$. In the case of a lepton, which was beyond the angular acceptance of the CTD, $p_T > 0.7\,\mathrm{GeV}$.

5.2.3 Track-cluster matching

- The distance of the closest approach (DCA) between the track and the cluster in the CAL was chosen to be 20 cm.
- The evidence of two islands in BCAL or RCAL with energy greater than 300 MeV was required. In the case of *two track* events both islands are matched to the tracks, in the other case only one is matched. No additional islands in BCAL and RCAL with $E > 400\,\mathrm{MeV}$ are required.

5.2.4 Lepton identification

The particle seen in the detector can be either an electron or a muon depending on the J/ψ decay channel. In the case of PT35m trigger, the latter is affected by the condition at the FLT level that the REMC subtrigger required an energy deposit in the EMC section of RCAL to be greater than 464 MeV. This requirement is easily fulfilled by electrons as they produce a purely electromagnetic cascade and deposit all their energy in the EMC section of the CAL. On the contrary, muons behave like minimum ionizing particles and leave only a small amount of energy along their path in both CAL sections, see Fig. 22. Very few of muons survive this requirement of the PT35m trigger.

So, it was decided to use only electrons from the PT35m trigger and the muon channel decay is obtained from the muon trigger configuration. To avoid a duplication of a

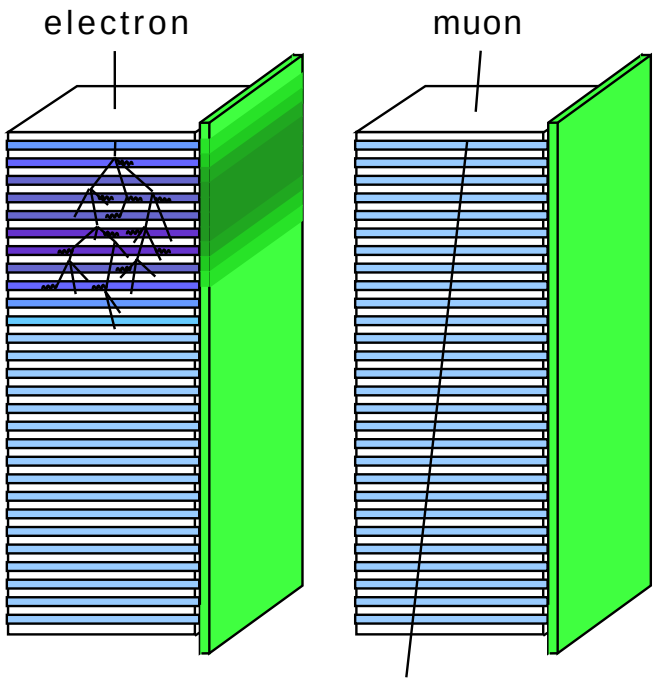

Figure 22: *Electrons and muons shower differently in the calorimeter.*

number of accepted muons it is necessary to separate electrons from muons in tagged photoproduction.

Due to the high W range the J/ψ mesons are boosted in the RCAL direction. Thus, one of the decay leptons tends to enter the RCAL close to the beam-pipe hole, so it is outside the CTD acceptance. Setting terminology, further the term 'decay track' refers to the well reconstructed track i.e. a track which crossed at least three superlayers, while the 'second lepton' is the decay lepton, located near to the beam pipe which remains unmatched (besides the *two track* events).

$\boxed{J/\psi \to e^+e^-}$

To exclude muons from PT35m triggered sample and restrict it only to electrons the shower characteristics mentioned above shower in the CAL was used. This feature causes that the lepton identification can be based on the ratio of energy deposited in the EMC section to the total energy of the island matched to the track: E_{EMC}/E. An event was

considered as electron decay channel candidate if

$$(\frac{E_{EMC}}{E})_{goodtrack} > 0.8. \tag{51}$$

Eq. 51 was applied only for the island associated with the well reconstructed track. In Fig. 23 (upper plot) the distribution of E_{EMC}/E for good track is shown and the vertical line indicates the above cut. The E_{EMC}/E distribution for the second lepton candidate with this cut applied to the decay track is shown on the lower plot of Fig. 23. For part of the events, for which E_{EMC}/E of the second lepton lies below 0.8, the reconstructed invariant mass of both leptons is within the chosen mass window (see Fig. 24). These events are regarded as electrons and are not rejected in further analysis.

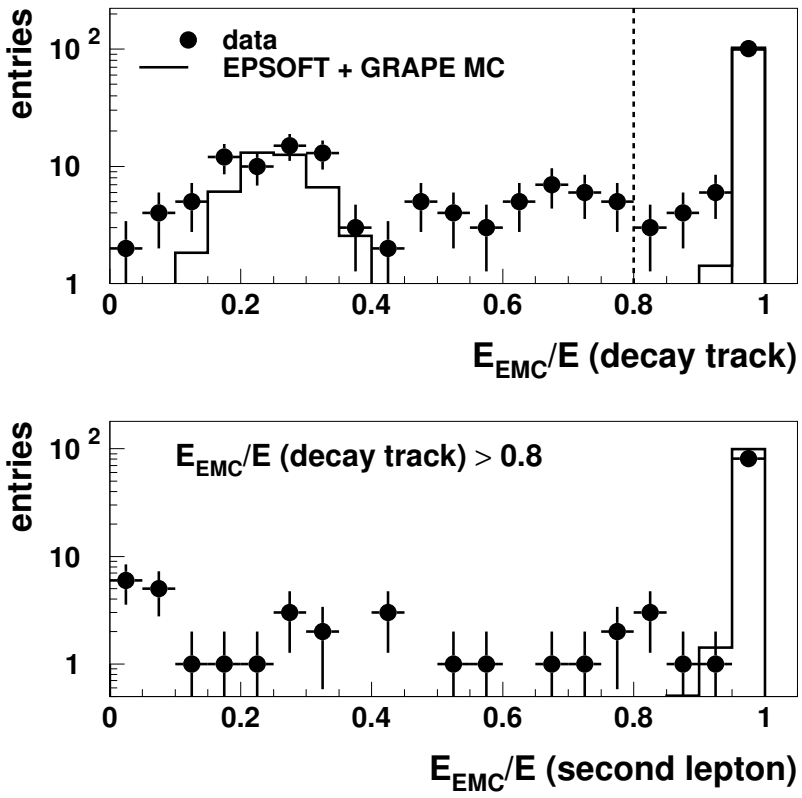

Figure 23: *The E_{EMC}/E distribution for event sample obtained with PT35m trigger. The upper plot is after all selection cuts, except these on E_{EMC}/E. The distribution on the lower plot was obtained after applying the cut $E_{EMC}/E > 0.8$ on the decay track.*

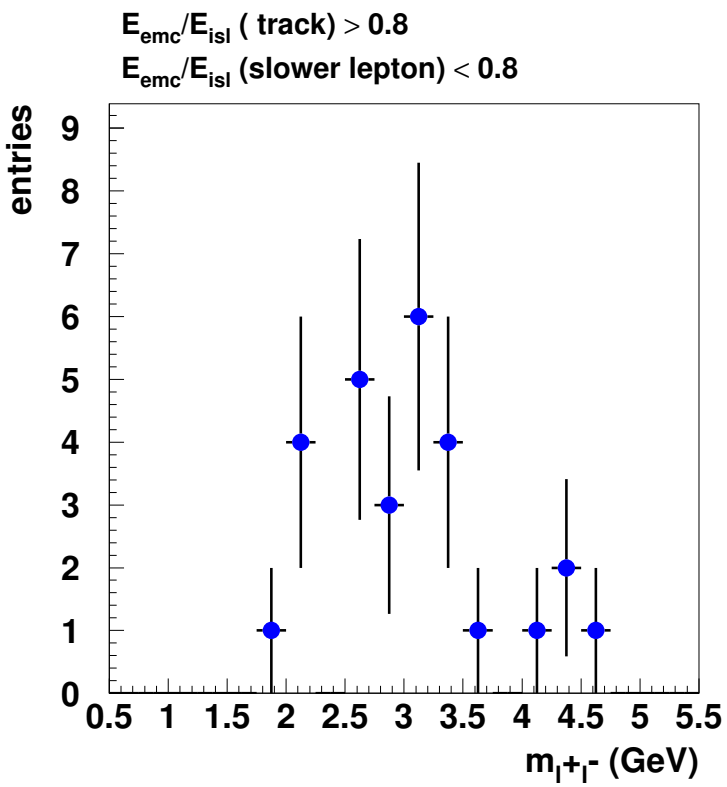

Figure 24: *The invariant mass spectrum for events with one lepton identified as electron and the other with ratio* $E_{EMC}/E < 0.8$.

$J/\psi \rightarrow \mu^+\mu^-$

No cut on E_{EMC}/E has been applied for the muon decay channel, obtained by the BRMU trigger. The leptons in this case are assumed to be muons due to the configuration of the trigger. This also is reflected in the distribution of E_{EMC}/E ratio in Fig. 25.

5.2.5 Reconstruction of the lepton energy

The reconstruction of the lepton four-momentum could be done on the base of the CTD, the CAL information and the energy of the scattered electron, deposited in the PT35m. The detailed reconstruction of the variables is given in Sec. 4.2.6.

In Fig. 26 the angular distribution of the decay leptons is shown, for electrons and muons

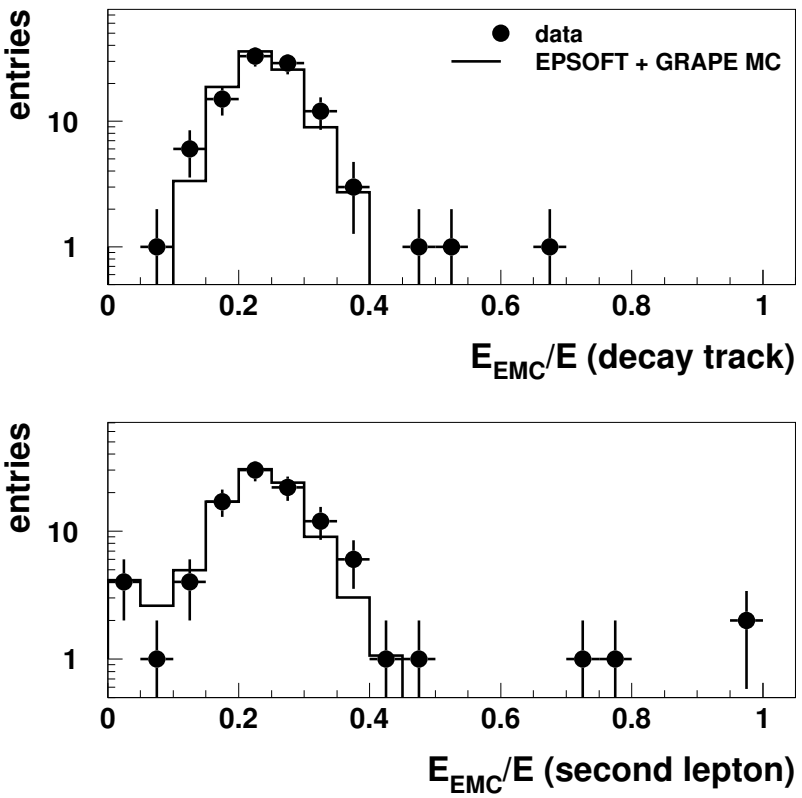

Figure 25: *The E_{EMC}/E distribution, after all selection cuts, for the muon decay channel obtained with the BRMU trigger. In the muon case no cut on E_{EMC}/E is used.*

separately. The upper plots present the angular distributions of the decay tracks, while the lower ones are for the second leptons.

For the *two track* event sample the full kinematic reconstruction is based only on the CTD. To reconstruct a *one track* event additional information is needed. Here, the four-momentum of the decay track is calculated from the CTD, while the energy of the second lepton is obtained from the cone island position in the CAL and the energy of the tagged electron, according to Eq. 50. This method allows to improve the resolution of the energy distribution, for $J/\psi \to e^+e^-$, compared to that obtained only from the CAL. The result of it is shown in Fig. 27. The other advantage is an extension of the available W range for $J/\psi \to \mu^+\mu^-$. So far previous analyses were performed in the lower range of W limited by the CTD acceptance [67, 68].

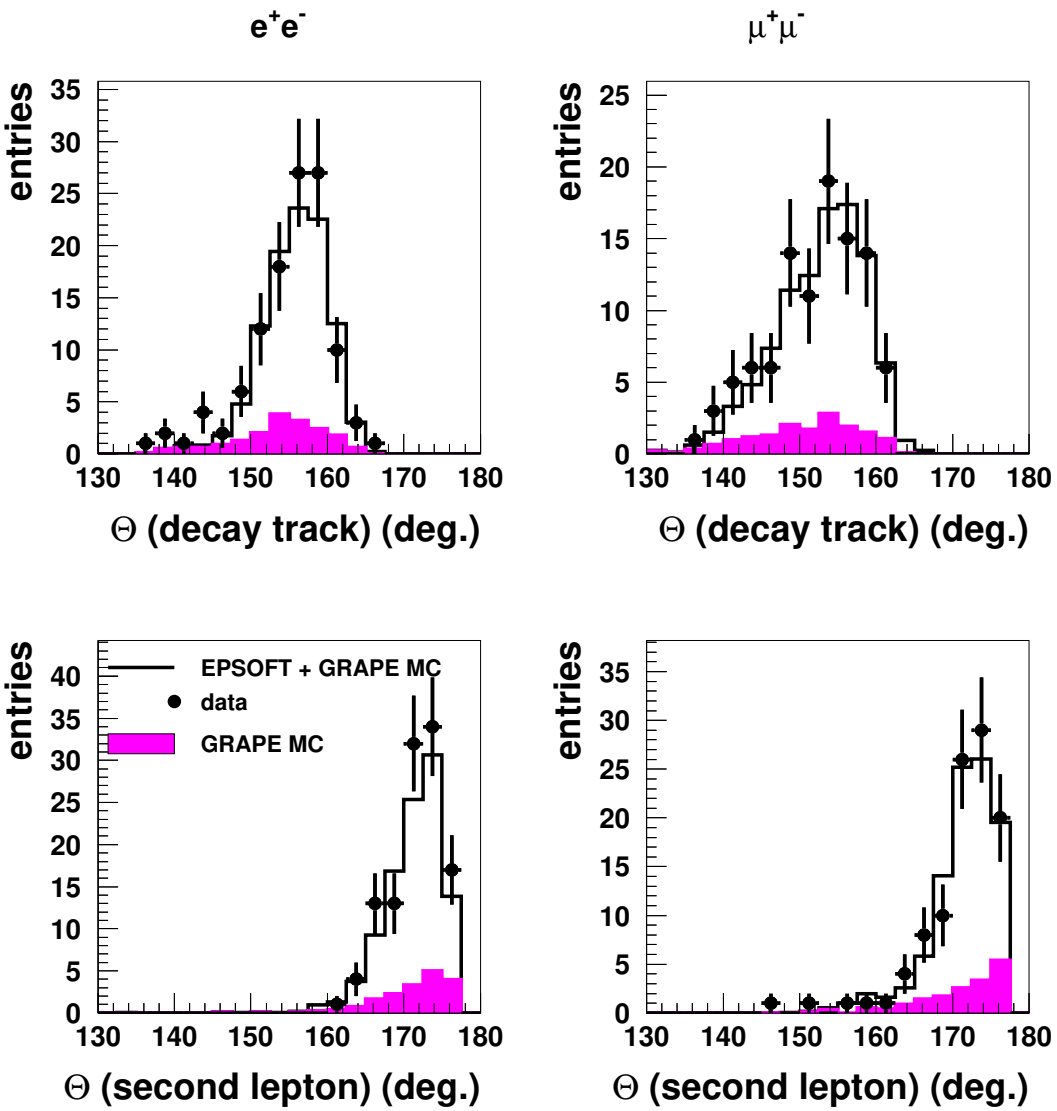

Figure 26: *The angular distribution of decay lepton candidates. The comparison of data (full dots) and MC (solid line) is shown, in left part of the figure for the electron decay channel, in right for muons. Upper plots presents the angular distribution of the reconstructed track within the CTD acceptance, while the lower plot is for second lepton candidates.The solid line is the sum of EPSOFT and GRAPE MC. The shaded area indicates the background coming from QED processes (GRAPE MC).*

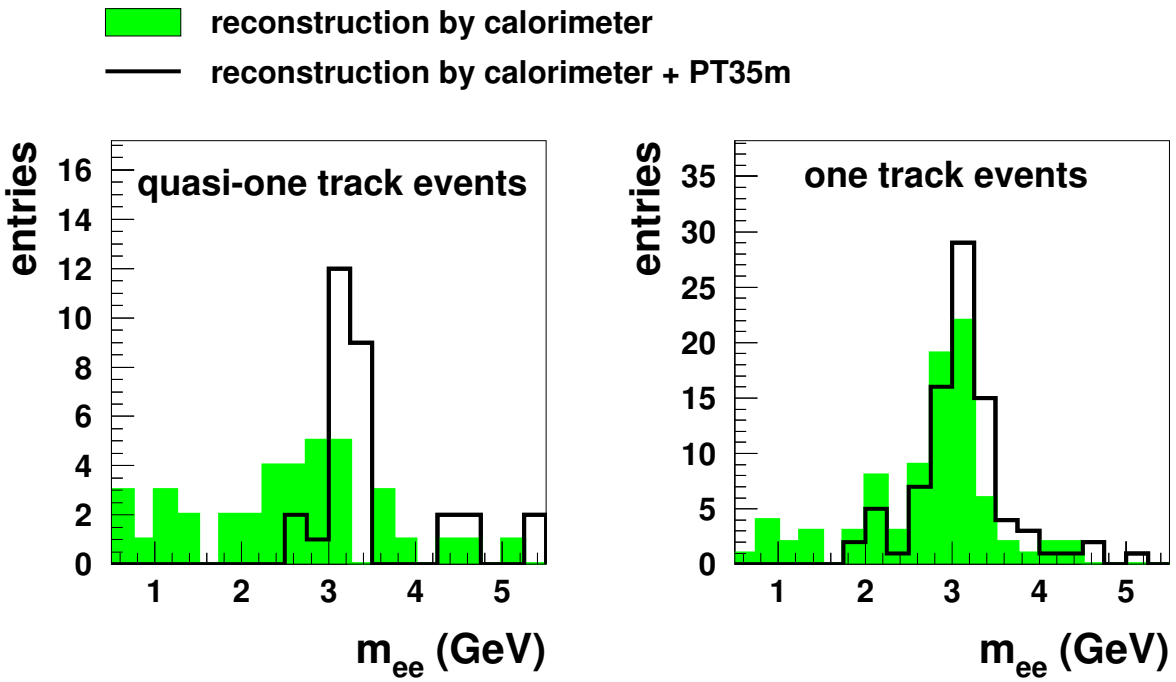

Figure 27: *The invariant mass, $J/\psi \to e^+e^-$, reconstructed with the CAL only (shaded histograms) and with the CAL and the PT35m (empty histogram), for quasi-one and one track events, separately.*

5.2.6 Proton dissociation

An event is proton-dissociative if a hit in PRT1 or an energy deposit in FCAL $E_{FCAL} > 400\,\text{MeV}$ is observed.

In Fig. 28 the distribution of the energy deposited in the FCAL is shown. The upper plot shows the distribution of the energy before tagging with the PRT, the lower one with tag in PRT.

5.2.7 The kinematic cuts

- The identification of the vector meson candidates was performed in the invariant mass range $1.5 < m_{ll} < 5.0\,\text{GeV}$.
- For both decay channels, electrons and muons, there was a requirement of the evidence of tagged electron in PT35m with energy $9 < E_{e'} < 17$ GeV within the acceptance of the tagger. The energy range of the PT35m translated into terms of photon-proton centre-of-mass energy gives the kinematic range restricted to $185 < W < 245$ GeV. Due to the low statistics there was no additional cut on the reconstructed electron

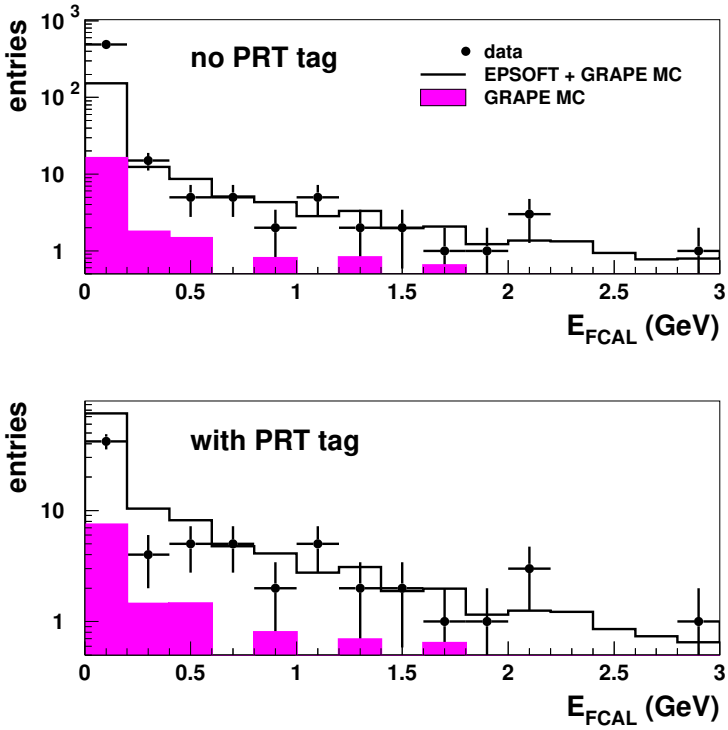

Figure 28: *The energy distribution in the FCAL after all selection cuts, except the PRT tag (upper plot) and with the PRT tag (lower plot). The full circles are the data, the solid line is the MC. The solid line is the sum of EPSOFT and GRAPE MC. The shaded area indicates the background coming from QED processes (GRAPE MC).*

position in the PT35m.

- Due to statistical limitation the range of $|t|$ was restricted to be $|t| < 7\,\mathrm{GeV}^2$.

5.3 Mass distribution

After all selection cuts described above a sample of 216 events remained. The sample is dominated by one track event topologies due to the high W range ensured by acceptance of electron tagger.

The detailed statistics is shown in Tab. 5. The mass distributions for each event topology, for electron and muon decay channel separately, are shown in Fig. 29. The mass spectra for the final sample for electrons and muons are presented in Fig. 30.

mode	one track events	quasi-one track events	two track events	all
muons	84	13	5	102
electrons	86	28	0	114

Table 5: *The detailed statistics of the collected J/ψ meson candidates sample.*

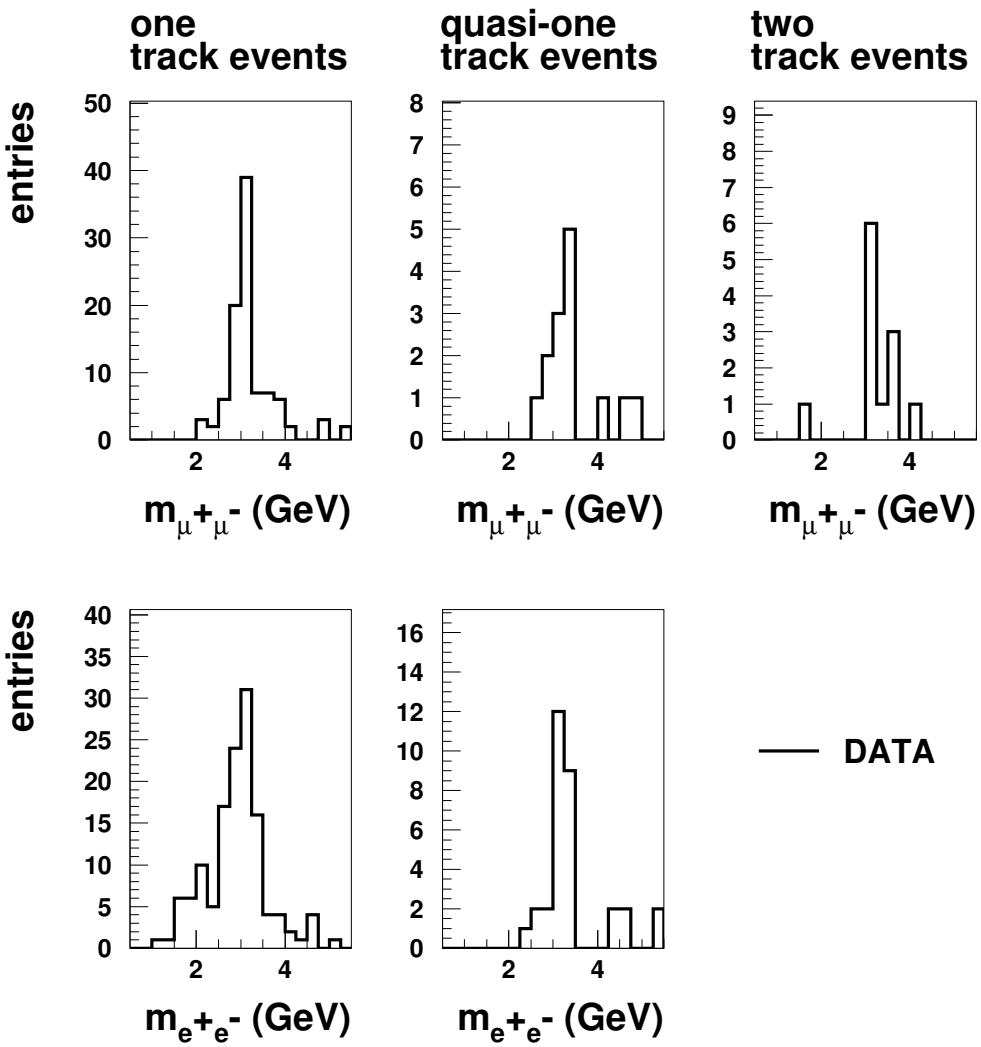

Figure 29: *The J/ψ mass distribution for all event topologies, after all selection cuts, in the data. Upper plots are for the muon channel decay, the lower ones for electrons.*

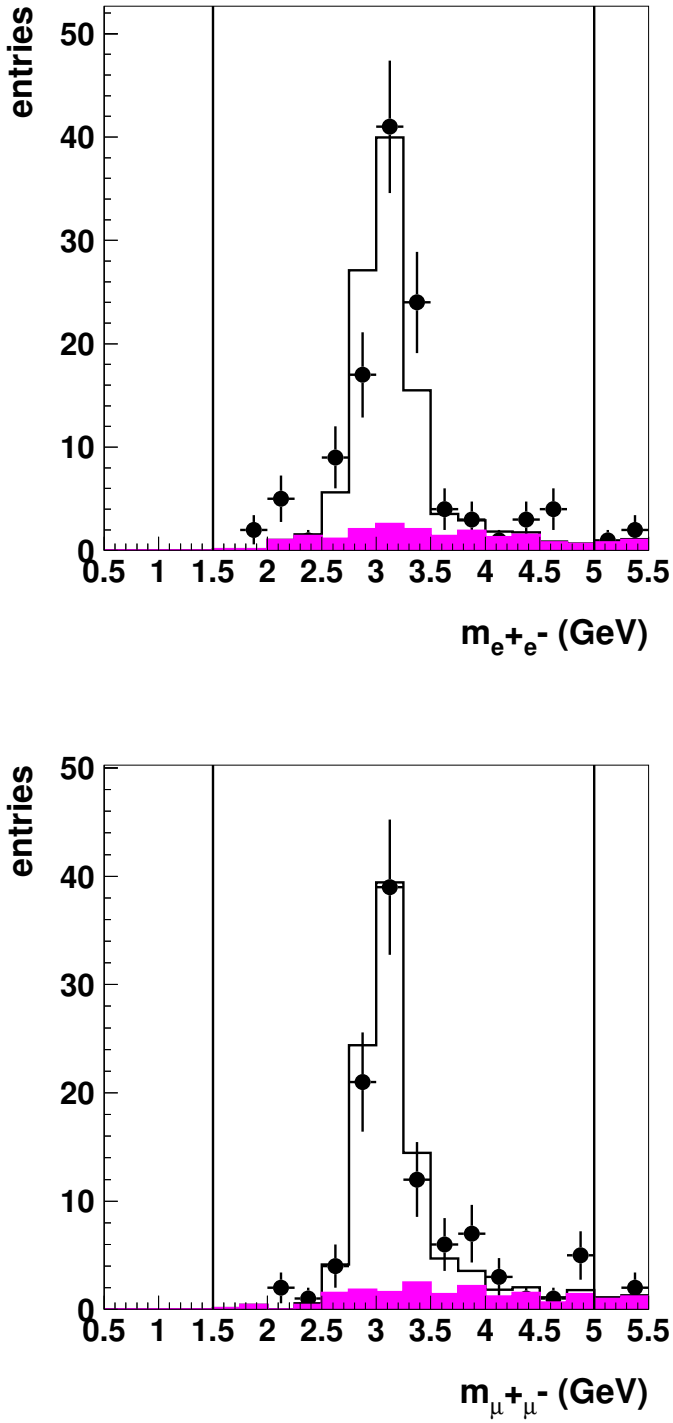

Figure 30: *The mass distribution of the final sample: $J/\psi \to e^+e^-$ (upper plot) and $J/\psi \to \mu^+\mu^-$ (lower plot). The full circles indicates the data, the solid line is a sum of EPSOFT and GRAPE MC, and the QED background (GRAPE MC) is indicated. The vertical lines show the mass window used in this analysis.*

6 Data and Monte Carlo comparison

6.1 Tuning of the MC parameters

The EPSOFT MC, which is used to obtain the acceptance, does not perfectly reproduce the data. To have confidence in the results one has to tune some parameters of the MC in order to get reasonable agreement between measured data distributions and the measured MC distributions. This procedure is called the reweighting of the MC.

In this analysis the reweighting function has three components. The first one comes from tuning the mass distribution of the proton dissociative system. The second one takes into account the differences between the $|t|$ distribution in data and MC. The third one is a correction of the muon chambers' efficiency, which was inadequate in the simulation of the ZEUS detector.

Reweighting of the dissociative mass distribution

The mass spectrum of the proton dissociative system has been generated according to Eq. 37 with $\beta = 2.0$. As this mass is not measured directly, one can look at the energy distribution in the FCAL, E_{FCAL}, coming from this nucleonic system, which is also sensitive to the parameter β. To find β best describing E_{FCAL} the minimum χ^2 method was used, with χ^2 function defined as

$$\chi^2 = \sum_{i=0} \frac{(d_i - m_i(\beta))^2}{\sigma_i^2}. \tag{52}$$

In Eq. 52 d_i is the number of data events, after the subtraction of the QED background, in bin i of the E_{FCAL} distribution, m_i is the number of MC events determined with parameter β in the corresponding bin and σ_i is the error assigned to the number of data and MC events in this bin. The sum runs through five bins in E_{FCAL}. The result of the fit is $\beta = 2.5 \pm 0.5$ and this value is used in further analysis.

Above value is compatible within errors with previous measurements [53, 69]. Fig. 31 shows the comparison of the energy distribution in FCAL between the data and the MC before and after reweighting.

Reweighting of t distribution

The next step in tuning MC is to improve the agreement between the data and MC in $|t|$ distribution. Since the EPSOFT MC was not generated with correct $|t|$ distribution, it had to be reweighted to describe data. The minimum χ^2 method was applied to

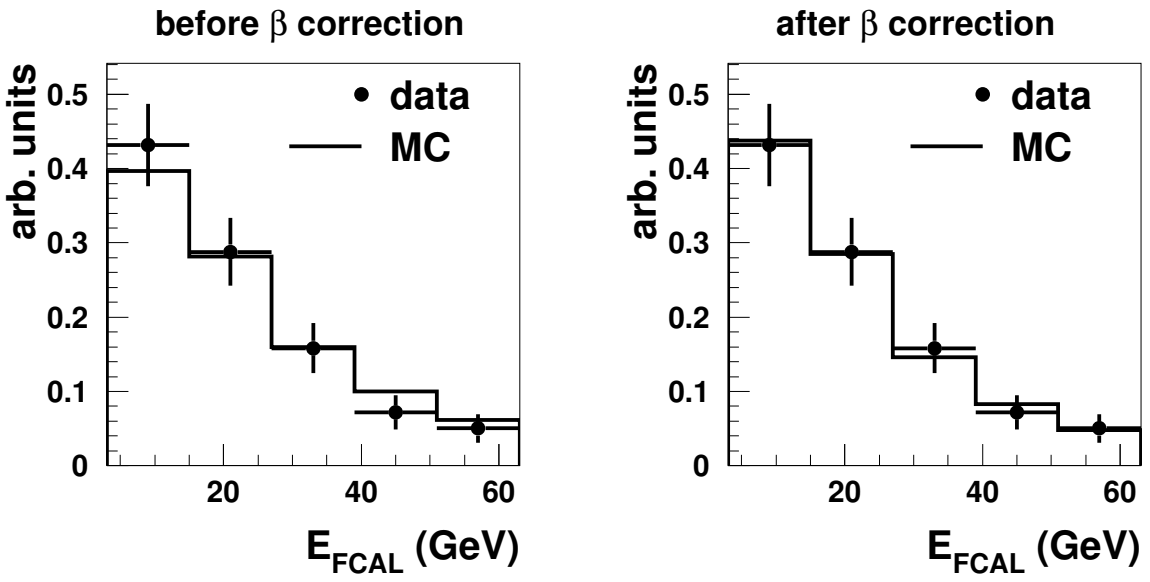

Figure 31: *Comparison of the distributions of the energy deposit in FCAL in the data (full circles) and MC simulation (solid line) before and after β correction. The distributions are normalized to unity.*

determine the parameters of the reweighting function. The minimalization was performed using MINUIT [70]. In the χ^2 fit the data distributions were compared to the MC after background subtraction.

BRMU efficiency corrections

The BRMU trigger efficiency is not correctly reproduced in the MC simulation. This is mainly caused by two reasons: the inadequate description of inactive material before the muon chambers and the lack of simulation of the chambers' inefficiencies due to dead limited streamer tubes. The correction factors were obtained separately for BMUI and RMUI using events with a reconstructed track with momentum $p > 2.5\,\mathrm{GeV}$ and $\eta > -1.6$, which also gives a signal in the inner and outer muon chambers. The detection efficiencies of the inner and outer chambers are slightly different due to greater radiation near the interaction point, however, here they are assumed equal. Assuming, that the probability to have a signal in the inner chamber is equal to the probability of signal coincidences in the inner and outer chambers, the correction factors were determined as 0.77 for BRMUI and 0.779 for RMUI. The error on these correction factors was estimated

to be 15% [71, 72].

6.2 Background studies

The selection criteria described in the earlier sections allow to extract the proton-dissociatively produced J/ψ signal. The selection cuts are effective for the removal of events with different decaying products and kinematics, especially the excited states of J/ψ production like $\psi' \to J/\psi\pi\pi$. In order to suppress such events, there was a requirement to have no additional energy deposits in BCAL or RCAL, except for the one associated with the track. In this case cone islands with an energy above 300 MeV were regarded as an additional particle and such an event was rejected. The energy of matched cone islands, after all selection cuts, is greater than 1.5 GeV for both decay leptons what excludes the contamination with the low energetic hadrons, which can be misidentified as decay leptons.

The major source of the background is the non-resonant background due to the lepton pair production by $\gamma\gamma$ fusion, which has a very similar topology to the proton-dissociative J/ψ production. The Bethe-Heitler events survive the selection cuts and their effective removal can be achieved by statistical subtraction from the data sample. For this aim the GRAPE MC was used, normalized to the luminosity of the data sample and statistically subtracted bin-by-bin from the data.

6.3 Comparison of data and MC

The comparison between the data and MC in various distributions is done after all selection cuts, except for the cut on the variable shown, and within an invariant mass window $1.5 < M_{l^+l^-} < 5.0\,\text{GeV}$. The final MC sample is a sum of EPSOFT and GRAPE MC.

The EPSOFT MC was reweighted as described in Sec. 6.1 and the normalization of the GRAPE MC was mentioned in Sec. 6.2. In Fig. 32 the distributions of the scattered electron energy is shown, separately for electrons and muons. The distributions of $|t|$ and W are shown in Fig. 33, for the whole sample and separately for both decay channels. The distributions of p_T of the tracks and the associated energy deposits in the CAL are shown in Fig. 34. These distributions are presented for electrons and muons, for decay tracks and the second lepton. The overall agreement between the data and MC is satisfactory.

6.4 Binning

The measurement of the cross section is performed in a particular range of the kinematic variables. The accessible phase space is divided into so-called bins. A large number of bins

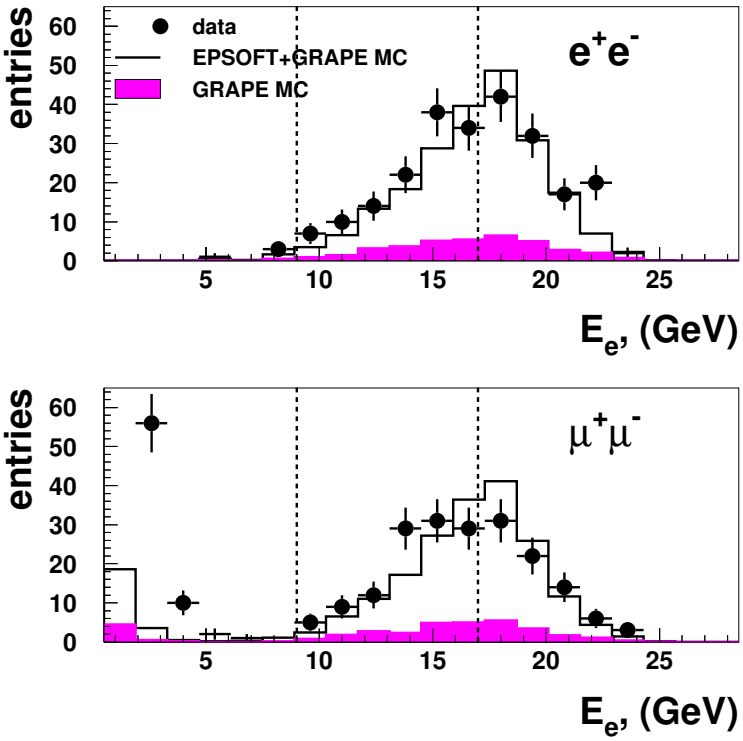

Figure 32: *The distribution of the energy of tagged electron for $J/\psi \to e^+e^-$ (upper plot) and $J/\psi \to \mu^+\mu^-$ (lower plot) in the data (full circles) and MC (solid line). The solid line is the sum of EPSOFT and GRAPE MC. The shaded area indicates the background coming from QED processes (GRAPE MC). The vertical lines show the kinematic range used in this analysis.*

gives more precise information about the shape of the cross section, on the other hand too small bin size provides the increase of statistical uncertainties and larger migration effects. So, the bin sizes should be at least of a similar size to the resolution of the kinematic variable in the particular bin.

The quality of the bins can be expressed by efficiency and purity, calculable with MC events, defined as follows:

$$efficiency = \frac{number\ of\ events\ generated\ and\ measured\ in\ bin\ \mathrm{i}}{number\ of\ events\ generated\ in\ bin\ \mathrm{i}}, \tag{53}$$

$$purity = \frac{number\ of\ events\ generated\ and\ measured\ in\ bin\ \mathrm{i}}{number\ of\ events\ measured\ in\ bin\ \mathrm{i}}. \tag{54}$$

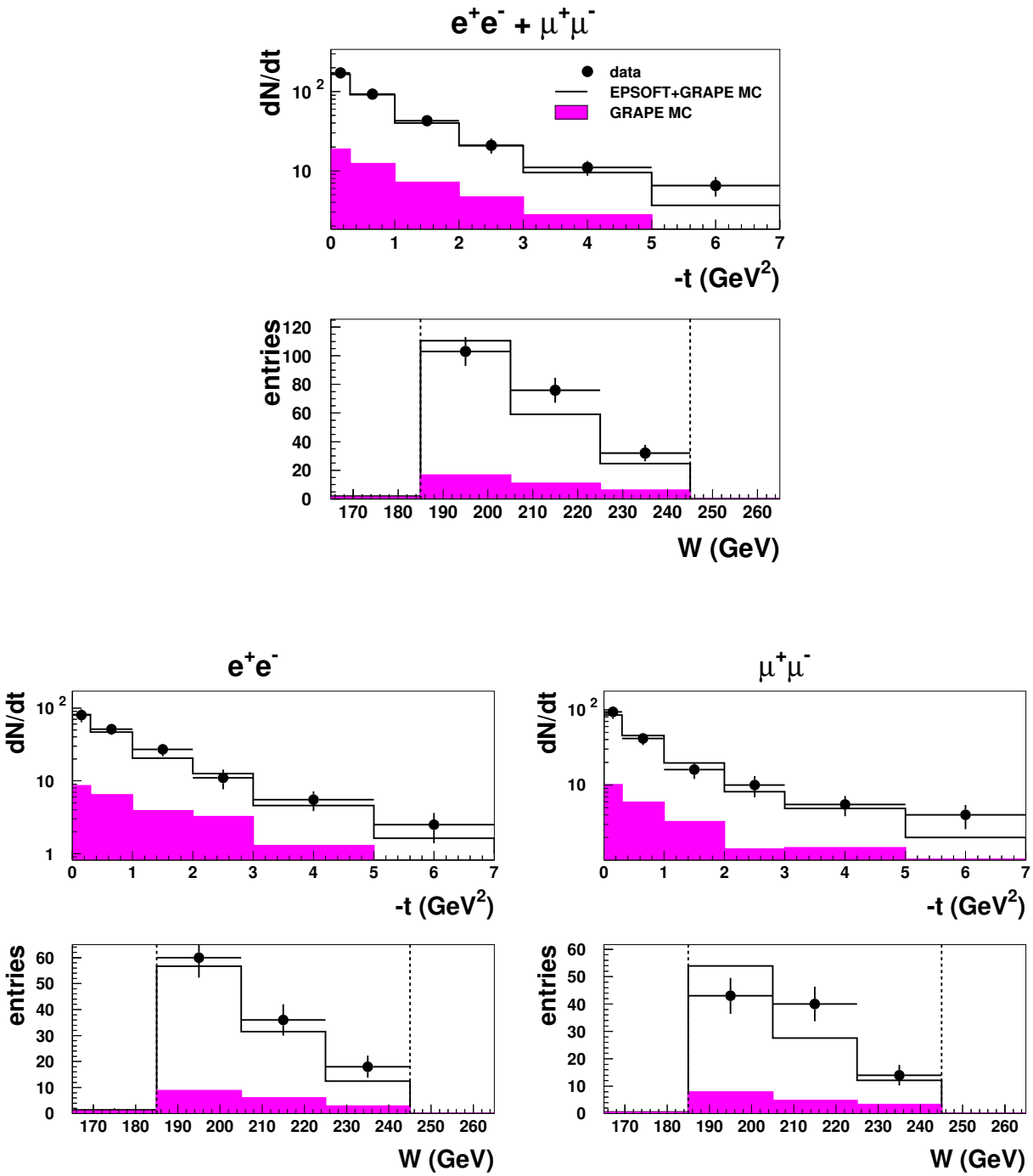

Figure 33: *The comparison of the W and t distributions in the data (full circles) and MC simulation (solid line). The solid line is the sum of EPSOFT and GRAPE MC. The shaded area indicates the background coming from QED processes (GRAPE MC).*

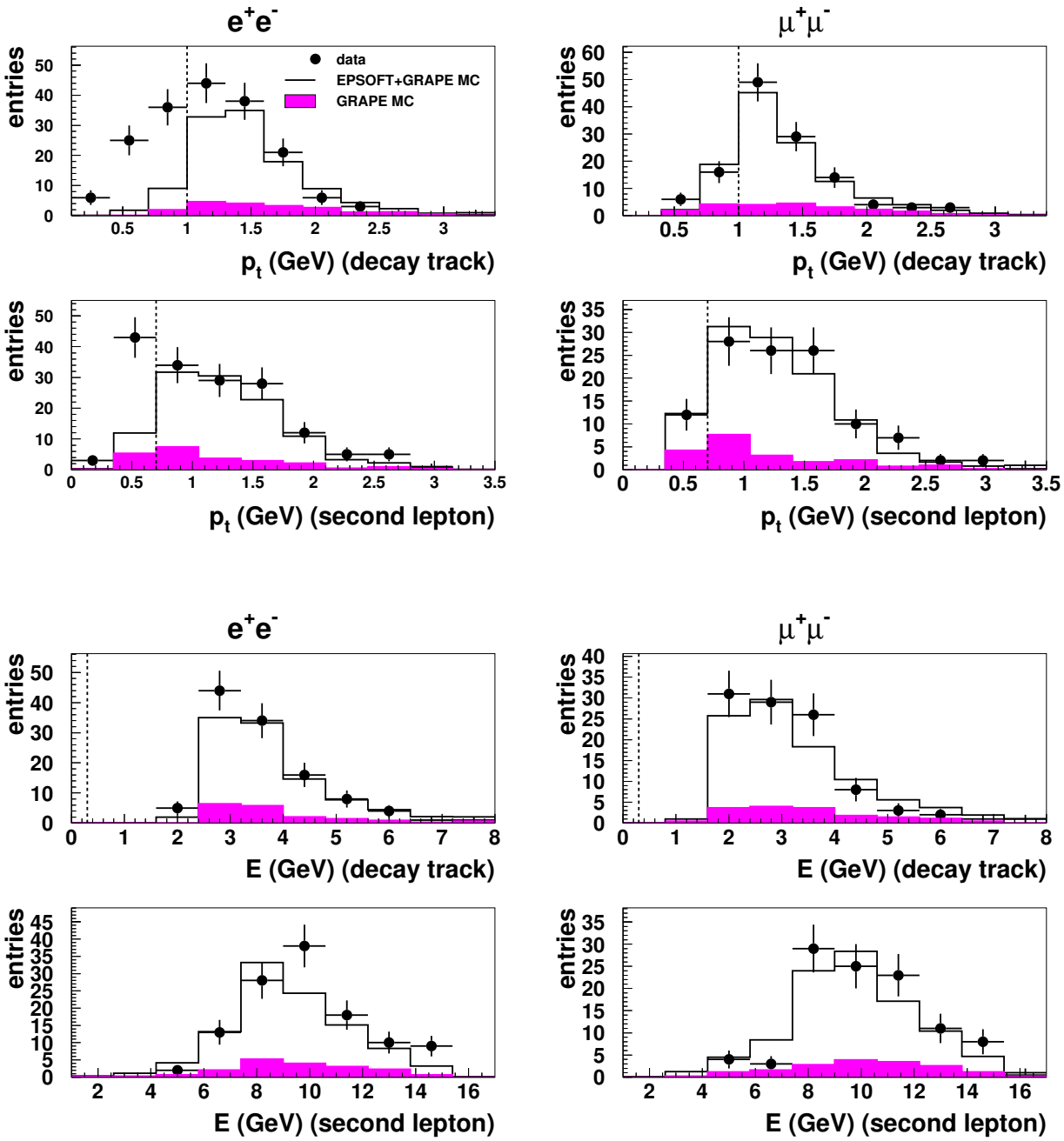

Figure 34: *The comparison of E and t distributions in the data (full circles) and MC simulation (solid line). The solid line is the sum of EPSOFT and GRAPE MC. The shaded area indicates the background coming from QED processes (GRAPE MC).*

The resolution for a particular variable is determined from the root-mean-square (RMS) of the distribution of the difference between its generated and reconstructed value. The efficiency is reduced by the analysis cuts, by trigger and detector acceptances and is affected by the resolution which is also strongly correlated to purity.

The study of the reconstruction of $E_{e'}$ (and also W, which is directly calculated from $E_{e'}$, see Eq. 49) is shown in Fig. 35 for both decay channels separately. The variable $E_{e'}$ is well measured over the range $9 < E_{e'} < 17\,\mathrm{GeV}$. The resolution of the measurement is less than 1 GeV.

The reconstruction of the variable $|t|$ is presented for electrons and muons in Fig. 36. The agreement is satisfactory, but becomes worse for higher values of $|t|$.

In further analysis bins in all relevant variables were chosen to be wider than the considered variable resolution. This suppresses the probability of migrations between the neighboring bins and lowers the correlation between statistical errors.

The acceptance is estimated on the basis of MC generated events in the selected kinematic region and is defined as:

$$acceptance = \frac{number\ of\ events\ measured\ in\ bin\ \mathrm{i}\ after\ all\ cuts}{number\ of\ events\ generated\ in\ bin\ \mathrm{i}}. \tag{55}$$

The acceptance determined according to Eq. 55 accounts for the detector and reconstruction efficiencies, the geometrical acceptance, the detector resolution and trigger efficiency. Fig. 37 shows the acceptance as a function of $|t|$ for the electron and muon decay channels separately, derived from the reweighted EPSOFT MC, in the same bins in which the differential cross section $d\sigma/dt$ was calculated. The average acceptance in both cases is about 5%.

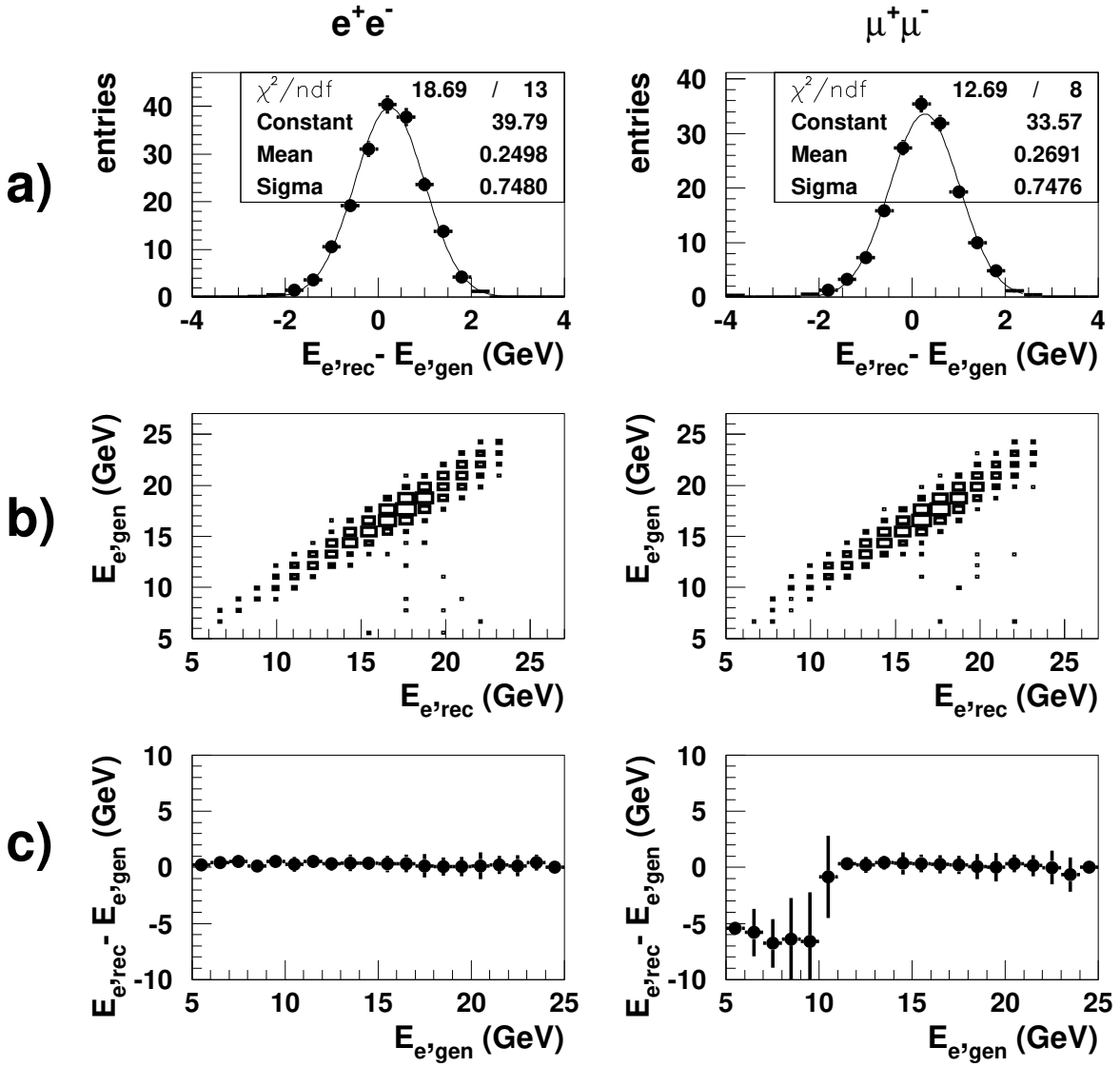

Figure 35: *The reconstruction of variable $E_{e'}$: (a) distribution of $E_{e'\mathrm{rec}} - E_{e'\mathrm{gen}}$; (b) correlation between $E_{e'\mathrm{rec}}$ and $E_{e'\mathrm{gen}}$; (c) $E_{e'\mathrm{rec}} - E_{e'\mathrm{gen}}$ as a function of $E_{e'\mathrm{gen}}$.*

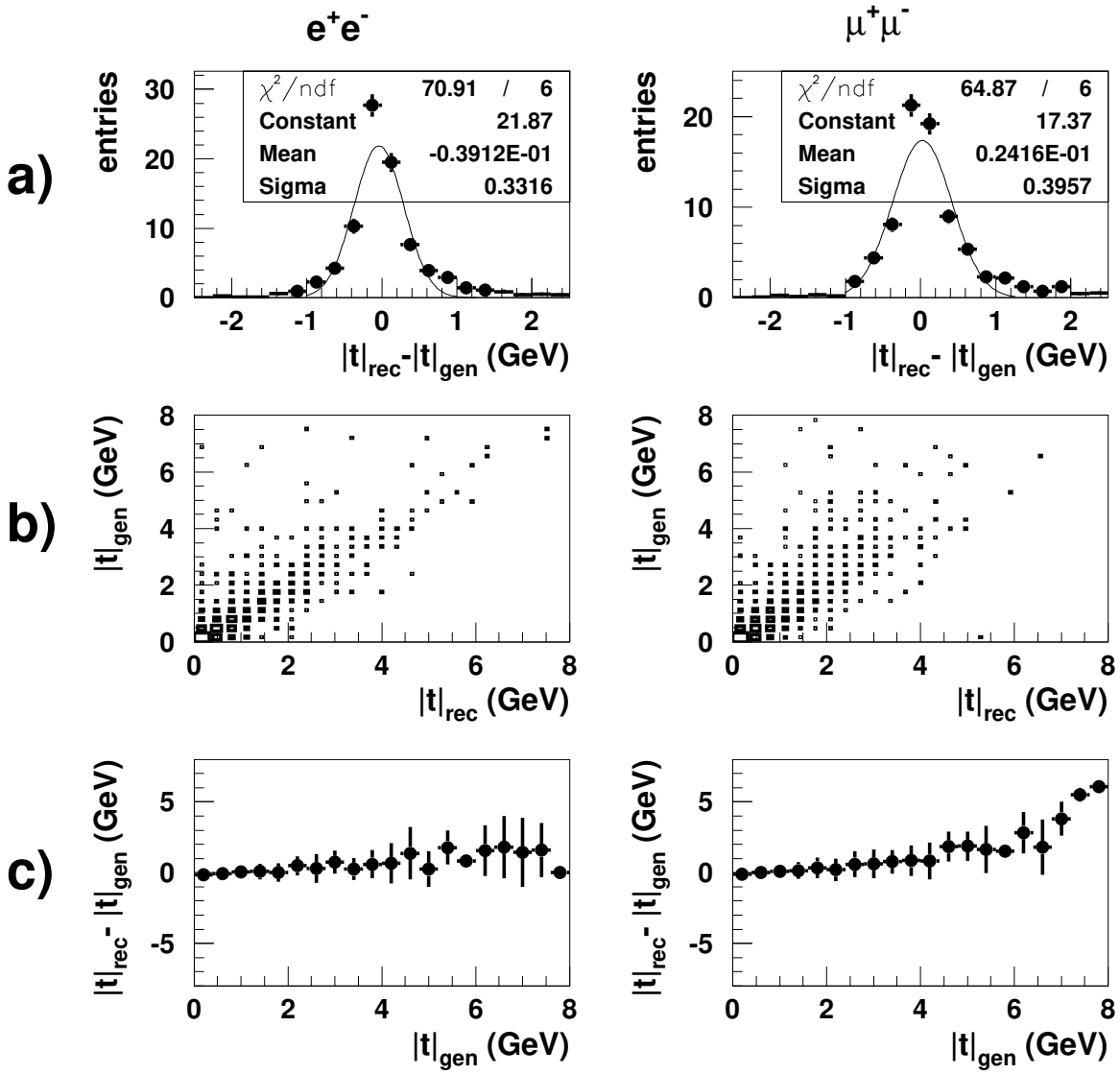

Figure 36: *The reconstruction of t: (a) distribution of $|t|_{rec} - |t|_{gen}$; (b) correlation between $|t|_{rec}$ and $|t|_{gen}$; (c) $|t|_{rec} - |t|_{gen}$ as a function of $|t|_{gen}$.*

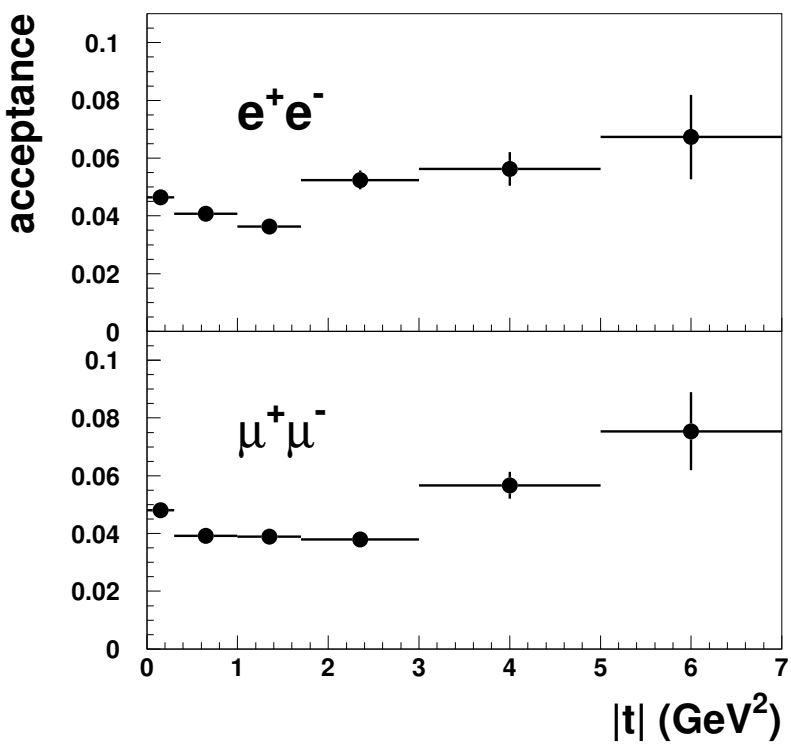

Figure 37: *The acceptance as a function of $|t|$ for the electron (upper plot) and muon (lower plot) decay channels.*

7 Experimental Results

7.1 Cross section definition

The differential cross section $d\sigma/dt$ for the proton-dissociative production of J/ψ in the reaction $\gamma p \to VY$ is given by the formula

$$\frac{d\sigma}{dt}(\gamma p \to VY) = \frac{N}{A \cdot \Phi_\gamma \cdot \Delta t \cdot BR \cdot \mathcal{L}}, \tag{56}$$

where N is the number of the events after all selection cuts and background subtraction in the given bin of $|t|$, $\mathcal{L}$ the integrated luminosity, Φ_γ the photon flux factor integrated over the y and Q^2 range covered in this analysis (see Sec. 1.2), A the acceptance including all detector efficiency corrections, BR the branching ratio for the particular J/ψ decay channel mode and Δt is the width of the $|t|$ bin. N was obtained from the formula

$$N = N_{data} - N_{BH}, \tag{57}$$

where N_{BH} is a number of expected QED Bethe-Heitler events. The effective flux factor for $Q^2 < 0.02\,\mathrm{GeV}^2$ and $185 < W < 245\,\mathrm{GeV}$ (corresponding to $0.37 < y < 0.66$) is $\Phi_\gamma = 0.00907036$. The integrated luminosity used to calculate the cross section is $\mathcal{L} = 30\ \mathrm{pb}^{-1}$ and $\mathcal{L} = 36\ \mathrm{pb}^{-1}$ for electrons and muons, respectively. The branching ratios are: $5.93 \pm 0.10\%$ for $J/\psi \to e^+e^-$ and $5.88 \pm 0.10\%$ for $J/\psi \to \mu^+\mu^-$.

The cross sections were calculated separately for the electron and muon decay channels. Both cross sections were then combined using the error weighted average. This calculations were determined for different kinematic ranges to compare with other measurements and theoretical models. The largest available kinematic range in this analysis corresponds to a condition $M_Y^2/W^2 < 0.1$ for which the MC was generated. To compare the obtained results to the previous ZEUS measurements [7] and theoretical models [73] the kinematic region was restricted to the region of model validity, $x > 0.01$ for $|t| > 1\,\mathrm{GeV}^2$, where x can be interpreted as a fraction of the proton momentum carried by the struck parton and is defined as

$$x = \frac{-(P' - P)^2}{2P(P' - P)} = \frac{|t|}{M_Y^2 - M_p^2 + |t|}. \tag{58}$$

To compare present results with the H1 measurement [74] the kinematic range was restricted to $M_Y^2/W^2 < 0.05$ what corresponds to $z > 0.95$, where z is defined as

$$z = \frac{P \cdot p_{J/\psi}}{P \cdot q} \tag{59}$$

and can be approximated by $z \approx 1 - (M_Y^2 + |t|)/W^2$.

7.2 Systematic uncertainties

The sources of the systematic uncertainties in the proton-dissociative J/ψ cross section measurement are the changes of selection cuts imposed on the data and the MC, the parameterization of the MC reweighting process or trigger efficiencies. Firstly the cross section was calculated with the nominal selection using the optimized cuts and reweighting parameters in the MC. Next, for each source of systematic errors, the cross section was reevaluated by changing the selection criteria or the parameter values in the MC-parameterization. The difference between the cross section σ_i resulting from the systematic check and the nominal one σ is taken as the systematic uncertainty, noted here as δ_i. All systematic checks were added in quadrature to form the total uncertainty, separately for checks decreasing and increasing the nominal value of the cross section, as follows:

$$\delta^{upper} = \sqrt{\sum_i \delta_i^2} = \sqrt{\sum_i (\sigma_i - \sigma)^2}, \quad \sigma_i - \sigma > 0, \tag{60}$$

$$\delta^{lower} = \sqrt{\sum_i \delta_i^2} = \sqrt{\sum_i (\sigma_i - \sigma)^2}, \quad \sigma_i - \sigma < 0 \tag{61}$$

The considered systematic uncertainties (the check index is placed in brackets) are the variations of:

- the cut on z position of the vertex. The nominal value $|z_{\text{vtx}}| < 60\,\text{cm}$ was changed to $|z_{\text{vtx}}| < 40\,\text{cm}$ {1},
- the energy range of the scattered electron, $9 < E_{e'} < 17\,\text{GeV}$ was enlarged by 800 MeV {2} and decreased by 800 MeV {3},
- the nominal cut on $p_t(\text{decay track}) > 1.0\,\text{GeV}$ was changed by $\pm 100\,\text{MeV}$ {4} {5},
- the nominal cut on $p_t(\text{second lepton}) > 0.7\,\text{GeV}$ was changed by $\pm 100\,\text{MeV}$ {6} {7},
- the nominal proton dissociative selection, requiring a tag in the PRT detector or an energy deposit in the FCAL was changed to only a tag in the PRT detector {8} and a tag or energy deposit in the FCAL to be grater than 1 GeV {9},
- the cut on $E_{EMC}/E > 0.8$ was changed to be 0.7 {10} and 0.9 {11},
- the correction factors (MC) for BRMU were changed by $\pm 15\%$ {12} {13},
- the nominal value of β was changed by ± 0.5 {14} {15}.

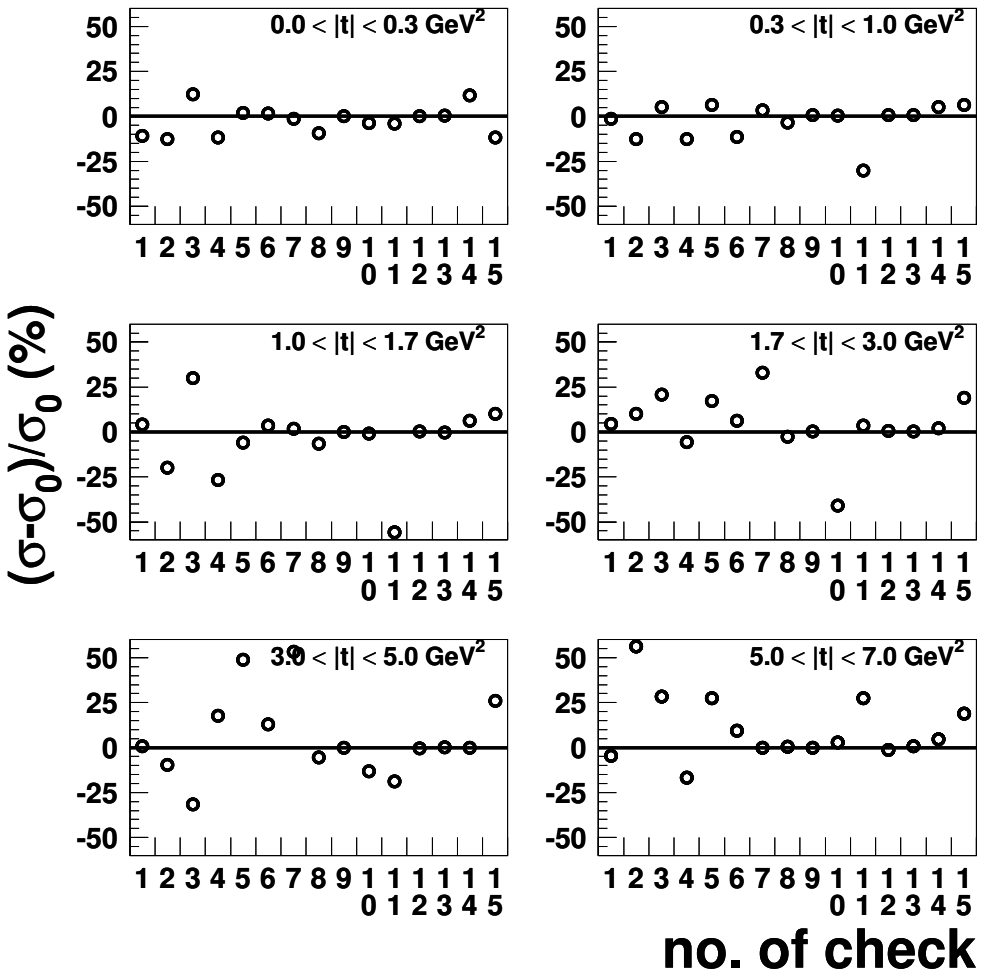

Figure 38: *The systematic uncertainty for $J/\psi \to e^+e^-$ in different $|t|$ bins. The systematic checks are described in the text.*

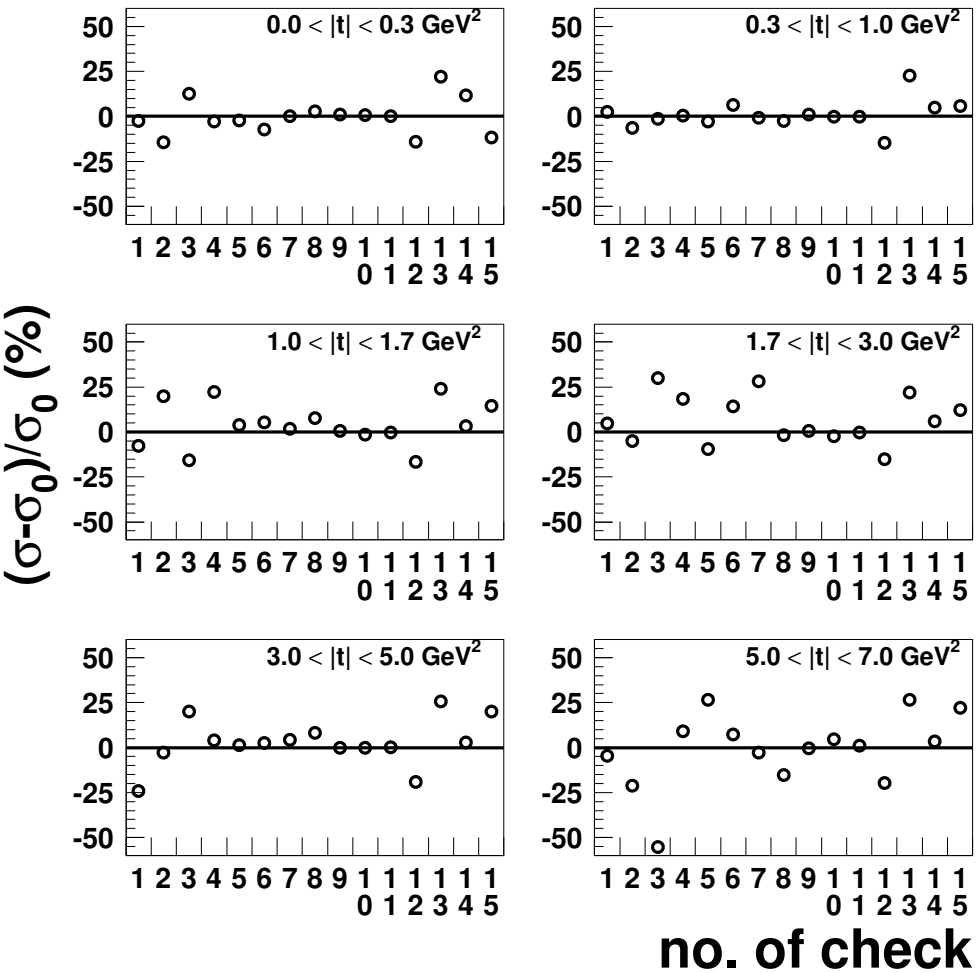

Figure 39: *The systematic uncertainty for $J/\psi \to \mu^+\mu^-$ in different $|t|$ bins. The checks are described in the text.*

7.3 Differential cross section

The differential cross section $d\sigma/dt$ for the proton dissociative J/ψ photoproduction was calculated according to the Eq. 56. These calculations were done for the electron and muon decay channels separately. To combine these cross sections the following procedure was applied: the weighted average cross section was calculated using the statistical uncertainty of each decay channel as weights. The obtained results for different kinematic ranges are presented in Tab. 6-8, where the first error is the statistical uncertainty, the second error is the statistical and systematic uncertainties added in quadrature.

$\lvert t\rvert$ range (GeV^2)	$< t >$ (GeV^2)	$\frac{d\sigma}{dt}$ $(J/\psi \to l^+l^-)$
0.0 - 0.3	0.15	$89.9 \pm 12.8\ ^{+19.3}_{-20.6}$
0.3 - 1.0	0.61	$53.7 \pm 6.9\ ^{+9.9}_{-10.7}$
1.0 - 1.7	1.31	$24.6 \pm 4.8\ ^{+8.5}_{-6.9}$
1.7 - 3.0	2.23	$11.3 \pm 2.1\ ^{+4.6}_{-3.2}$
3.0 - 5.0	3.78	$4.0 \pm 1.0\ ^{+1.7}_{-1.4}$
5.0 - 7.0	5.76	$1.8 \pm 0.9\ ^{+1.2}_{-1.0}$

Table 6: *The differential cross section $d\sigma/dt$ for $J/\psi \to l^+l^-$, calculated in the kinematic range $M_Y^2/W^2 < 0.1$.*

$\lvert t\rvert$ range (GeV^2)	$< t >$ (GeV^2)	$\frac{d\sigma}{dt}$ $(J/\psi \to l^+l^-)$
0.0 - 0.3	0.15	$89.9 \pm 12.8\ ^{+19.4}_{-20.8}$
0.3 - 1.0	0.61	$53.3 \pm 6.9\ ^{+9.6}_{-10.8}$
1.0 - 1.7	1.31	$23.9 \pm 4.7\ ^{+8.0}_{-6.8}$
1.7 - 3.0	2.23	$10.8 \pm 2.8\ ^{+4.3}_{-3.1}$
3.0 - 5.0	3.78	$3.8 \pm 0.9\ ^{+1.5}_{-1.3}$
5.0 - 7.0	5.76	$1.7 \pm 0.8\ ^{+1.1}_{-0.9}$

Table 7: *The differential cross section $d\sigma/dt$ for $J/\psi \to l^+l^-$, calculated in the kinematic range $M_Y^2/W^2 < 0.05$.*

The invariant mass spectra in bins used for the cross section calculation are shown in Fig. 40 and in Fig. 41 for electrons and muons, respectively.

In Fig. 42 the differential cross sections for the electron and muon decay channels are presented, for a kinematic region $M_Y^2/W^2 < 0.1$. Fig. 43 shows the combined cross section for both decay channels with the result of the power-like fit done for the $|t|$ range

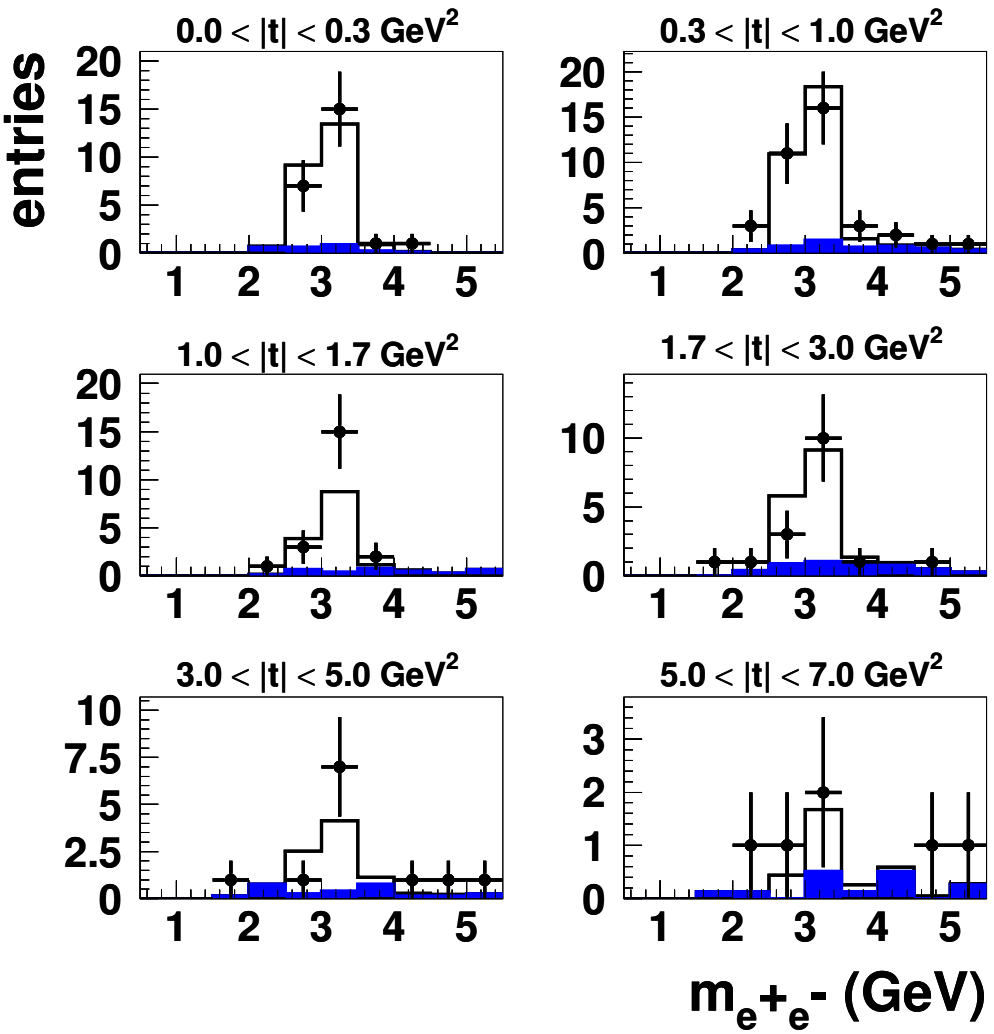

Figure 40: *$M_{e^+e^-}$ distributions in data (full dots) compared to MC (solid line) in bins of $|t|$. The solid line is the sum of the EPSOFT and GRAPE MC. The shaded area indicates the background coming from QED processes (GRAPE MC).*

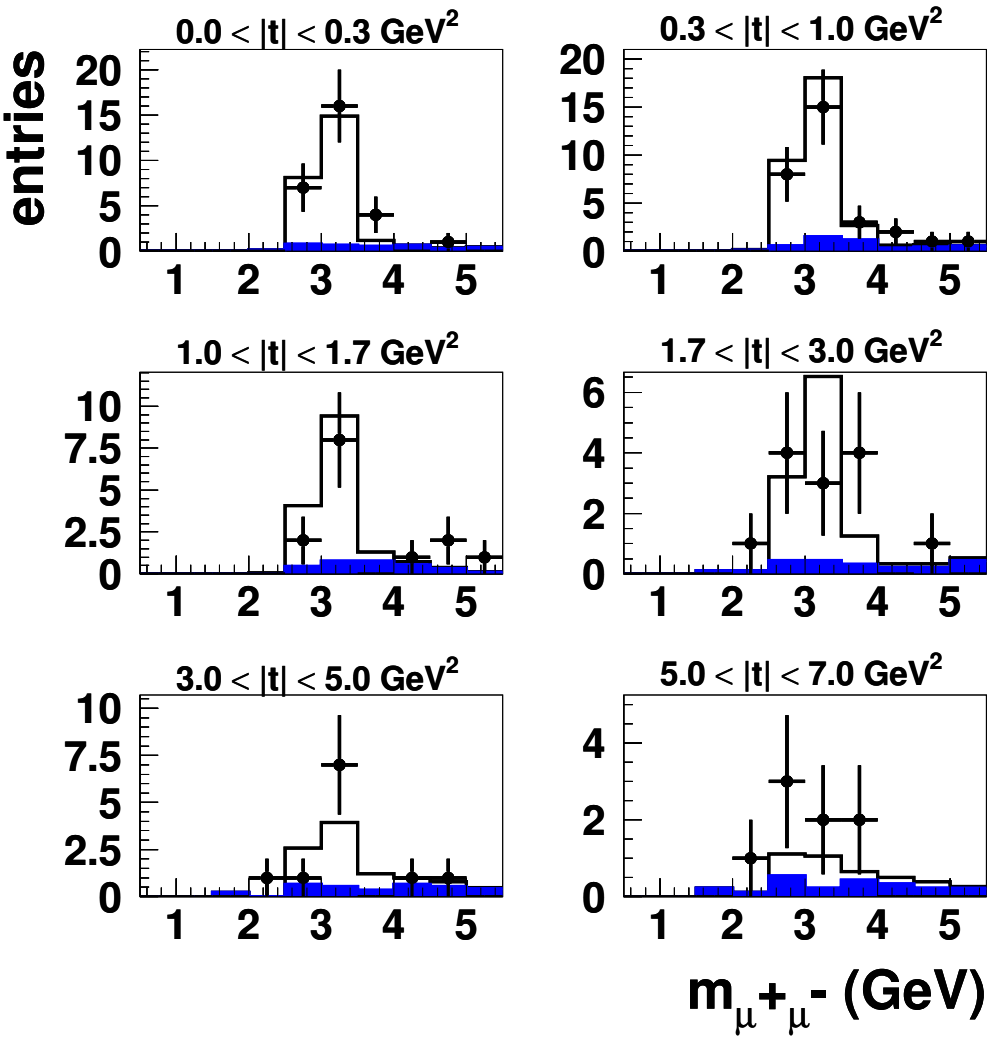

Figure 41: *$M_{\mu^+\mu^-}$ distributions in data (full dots) compared to MC (solid line) in bins of $|t|$. The solid line is the sum of the EPSOFT and GRAPE MC. The shaded area indicates the background coming from QED processes (GRAPE MC).*

$\|t\|$ range (GeV^2)	$< t >$ (GeV^2)	$\frac{d\sigma}{dt}$ $(J/\psi \to l^+l^-)$
1.0 - 1.7	1.31	$19.6 \pm 3.8\ ^{+6.9}_{-6.5}$
1.7 - 3.0	2.23	$9.4 \pm 1.8\ ^{+3.8}_{-3.0}$
3.0 - 5.0	3.78	$3.4 \pm 0.8\ ^{+1.4}_{-1.2}$
5.0 - 7.0	5.76	$1.6 \pm 0.8\ ^{+1.1}_{-0.9}$

Table 8: *The differential cross section $d\sigma/dt$ for $J/\psi \to l^+l^-$, calculated in the kinematic range $x > 0.01$ and $|t| > 1\ GeV^2$.*

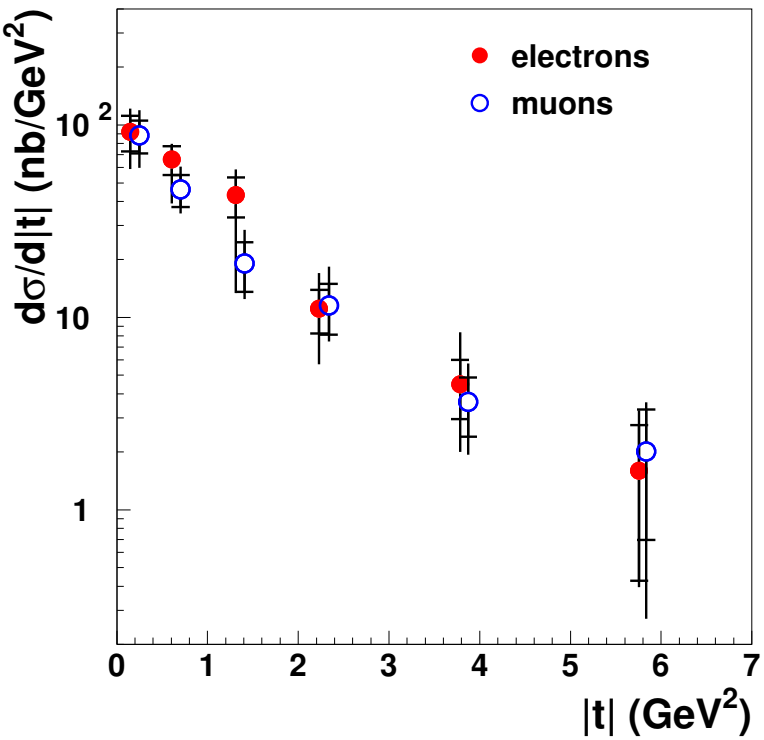

Figure 42: *Proton dissociative J/ψ photoproduction $d\sigma/dt$ cross section for the electron (full circles) and muon (open circles) decay channels separately. The cross sections correspond to a kinematic range of $M_Y^2/W^2 < 0.1$. In the figure the inner error bars represent the statistical errors and the outer error bars shows the statistical and systematic errors added in quadrature . The muon cross section was shifted artificially in $|t|$ to enable easier comparison between both cross sections.*

of $1.0 < |t| < 7.0\,\mathrm{GeV}^2$. The results of the fit with a function $\frac{d\sigma}{dt} = A \cdot |t|^{-n}$, for a different kinematic ranges are shown in the Tab. 9.

$\|t\|$ range GeV^2	power n	stat. error	syst. error	kin. range
1.0 - 7.0	1.75	0.24	0.35	$M^2/W^2 < 0.1$
1.0 - 7.0	1.76	0.24	0.34	$M^2/W^2 < 0.05$
1.0 - 7.0	1.67	0.24	0.34	$x > 0.01$

Table 9: *Results of the fits of a power-like function $A \cdot |t|^n$ to the differential cross section $d\sigma/dt$ in different kinematic ranges.*

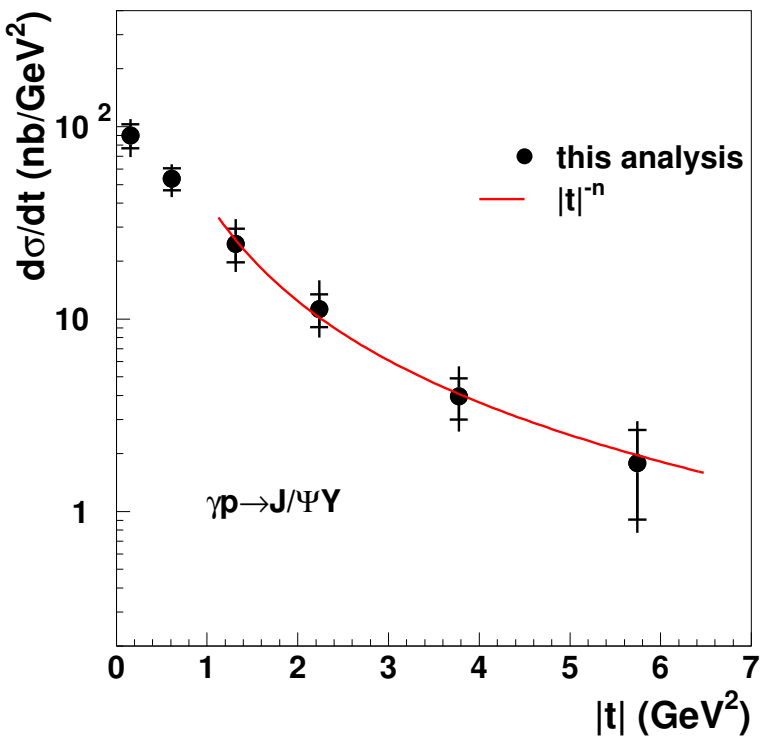

Figure 43: *Proton dissociative J/ψ photoproduction cross section $d\sigma/dt(J/\psi \to l^+l^-)$ in the kinematic range $M_Y^2/W^2 < 0.1$ with a power-like fit, $n = 1.75 \pm 0.24(stat.) \pm 0.35(syst.)$.*

7.4 Comparison with other measurements

In this section the results of the present analysis are compared to the earlier measurements of ZEUS and H1, done for a lower W range and in different ranges of $|t|$.

In the Fig. 44 the differential cross section $d\sigma/dt$ calculated for the kinematic range $M_Y^2 < 0.1W^2$ is compared with the ZEUS measurement [6] restricted to the same condition, but

for average center-of-mass energy $\langle W \rangle = 94\,\text{GeV}$. This measurement is based on the data collected in 1995. Because of large errors at low W it is hard to conclude if there is any rise of the cross section with energy.

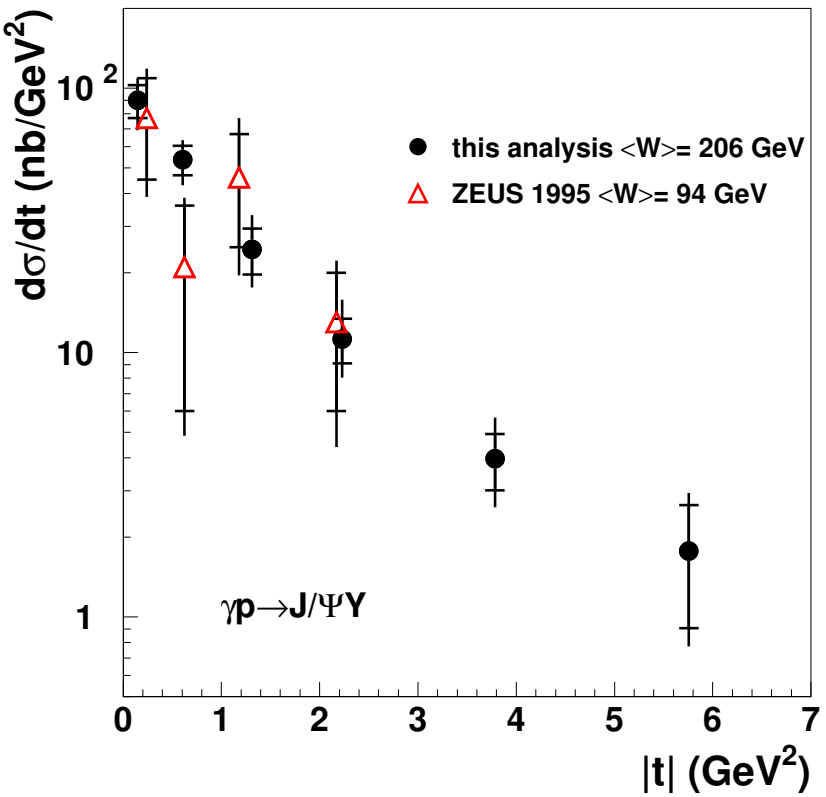

Figure 44: *The comparison of the $d\sigma/dt$ obtained in the present analysis (full circles) with the earlier ZEUS measurement [6] (open triangles) with average center-of-mass energy $\langle W \rangle = 94$ GeV. Both measurement are here restricted to the kinematic range of $M_Y^2 < 0.1 W^2$.*

A comparison performed with a more precise ZEUS measurement [7], based on the data collected in 1996-1997 is shown in Fig. 45. This measurement enlarged the $|t|$ region to $6.5\,\text{GeV}^2$ and is restricted to $80 < W < 120\,\text{GeV}$ and $x > 0.01$. To compare both analyses, the present results are restricted to this latter condition.

The H1 results are obtained in a very large range of $|t|$, namely $|t| < 30\,\text{GeV}^2$, and for $50 < W < 150\,\text{GeV}$. To make direct comparison between both analyses, the present data

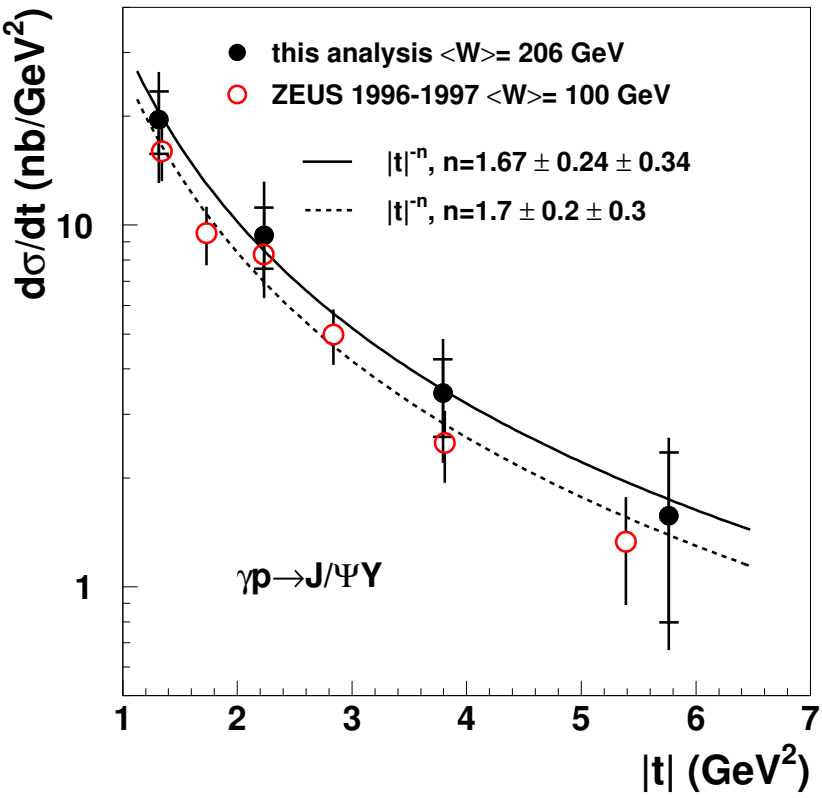

Figure 45: *The comparison of the $d\sigma/dt$ obtained in the present analysis (full circles) with ZEUS measurement [7] (open circles) done for $80 < W < 120$ GeV and $|t| < 6.5$ GeV^2. Both measurements are here restricted to $x > 0.01$.*

are restricted to $M_Y^2 < 0.05W^2$, what corresponds to the kinematic range of $z > 0.95$ for which the H1 measurement was done.

As can be seen on Fig. 45 and Fig. 46 measurements at different energies are compatible within the errors however the cross section at $W \approx 200\,\text{GeV}$ is systematically larger than at $W \approx 100\,\text{GeV}$. To quantify this observation, in Fig. 47 the cross section $\sigma_{\gamma p \to J/\psi Y}$ is presented as a function of W in two bins of $|t|$: $1.2 < |t| < 2.0\,\text{GeV}^2$ and $2.0 < |t| < 6.5\,\text{GeV}^2$. The data at $\langle W \rangle = 100\,\text{GeV}$ are taken from the earlier ZEUS measurement [7]. As can be seen in the figure, at higher $|t|$, the cross section seems to rise with increasing energy.

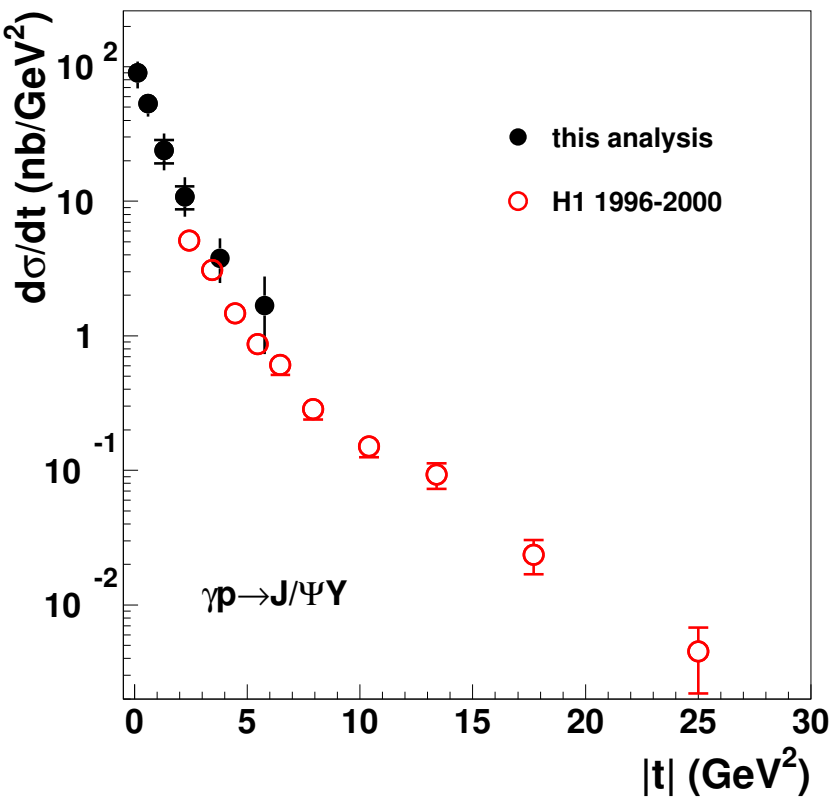

Figure 46: *The comparison of the $d\sigma/dt$ obtained in the present analysis (full circles) restricted to $M_Y^2 < 0.05W^2$ with the H1 measurement [74] (open circles) done for $50 < W < 150$ GeV, $|t| < 30$ GeV^2, and $z > 0.95$.*

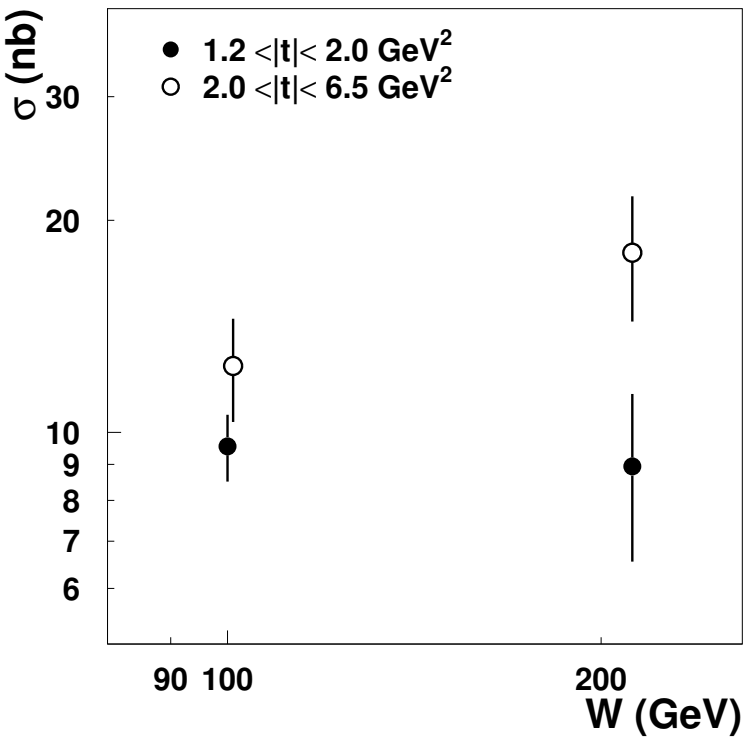

Figure 47: *The photon-proton cross section as a function of W in two bins of $|t|$ calculated in the kinematic range of $x > 0.01$. The errors are statistical only.*

8 Comparison with theoretical models

8.1 Comparison with BFKL model

The γp scattering, at large momentum transfer $|t|$ can be viewed as the exchange of a pomeron. It couples predominantly to individual partons in the proton. This is fulfilled if the size of the pomeron, ($\sim \frac{1}{\sqrt{|t|}}$), is smaller than this of the proton ($\sim \frac{1}{Q_0^2}$), with $Q_0^2 \sim 1\,\mathrm{GeV}^2$ which leads to condition $|t| > 1\,\mathrm{GeV}^2$ [36]. A pomeron exchange, in the lowest order approximation consists of two gluons [35]. The process under study occurs at energies $\sqrt{\hat{s}} \gg t$, where $\hat{s}$ is the photon-parton centre-of-mass energy. In such kinematic region, the pQCD corrections to the two gluon exchange are enhanced by powers of large logarithms of the energy, $\log(\hat{s}/|t|)$. The leading logarithmic corrections (LL) are proportional to $[\alpha_s \log(\hat{s}/|t|)]^n$ at the n-th order of the perturbative expansion. Thus, it is not sufficient to consider the lowest order approximation. The resummation of LL terms to all orders in α_s is given by the BFKL equation [36,73,75,76]. In this calculations the cross section for heavy vector meson production are related to the cross section for the elastic scattering of the parton (from the pomeron) to the parton in the proton. The cross section for the elastic parton-parton scattering are calculated on the base of the Mueller-Tang [77] prescription. In this approximation parts of the amplitude which vanish for infinite large rapidity gap are neglected. The recent model [73] investigates proton-dissociative vector meson production beyond the LL BFKL approximation and the Mueller-Tang prescription, introducing non-leading (NL) corrections.

The cross section for the diffractive scattering of a virtual photon off the proton is related to the parton-photon cross section and the parton densities in the proton (Eq. 35). The partonic cross section, characterized by the invariant collision energy squared $\hat{s} = xW^2$ can be approximated as:

$$\frac{d\sigma(\gamma q \to V q)}{dt} \sim \frac{\alpha_s^4}{t^4} |\mathcal{F}(z,\tau)|^2 \tag{62}$$

where $z = \frac{3\alpha_s}{2\pi} \ln(\frac{\hat{s}}{\Lambda^2})$ and $\tau = \frac{|t|}{M_V^2 + Q_\gamma^2}$ with M_V being the mass of the vector meson, Q_γ^2 is the photon virtuality (taken to be zero for photoproduction) and Λ is characteristic mass scale related to M_V and $|t|$. The coupling of the pomeron to quarks is the same as the coupling to gluons except for a constant factor color $\frac{81}{16}$. The function $\mathcal{F}$ introduces the W-dependence of the differential cross section and hardens the t-dependence.

The BFKL model predicts an approximate power-law behaviour for the t dependence of the form $d\sigma/dt \propto |t|^{-n}$ and strong rise of the cross section with increasing energy (in contrary to the two gluon exchange which yields energy independent cross section).

The prediction of the BFKL model [73] are compared in this section with the previous ZEUS measurement [7] ($\langle W \rangle = 100\,\mathrm{GeV}$) and the results of the present analysis ($\langle W \rangle =$

200 GeV). This model has two free parameters $\alpha_0 = 0.21$ and s_0 (governing the dynamics of the gluon ladder) which is taken to be $0.5\,\mathrm{GeV}^2$. These parameters were chosen to reproduce the measurements of the $\rho, \phi, J/\psi$ cross sections at $\langle W \rangle = 100\,\mathrm{GeV}$ [7] using LL approximation. The BFKL LL and BFKL LL + NL calculations for fixed α_0 and s_0 were then extrapolated to $\langle W \rangle = 200\,\mathrm{GeV}$.

In Fig. 48 and Fig. 49 the comparison between the data and theoretical predictions are presented. They are shown in different combinations to enable detailed comparisons. Both measurements are compared with BFKL calculations in LL approximation and with the non-leading (NL) corrections. The LL calculations reproduce well the shape of the t distributions, but overestimate the magnitude of its rise with increasing W. The leading logarithmic approximation including non-leading corrections gives a weaker cross section dependence on W but results in steeper t distributions.

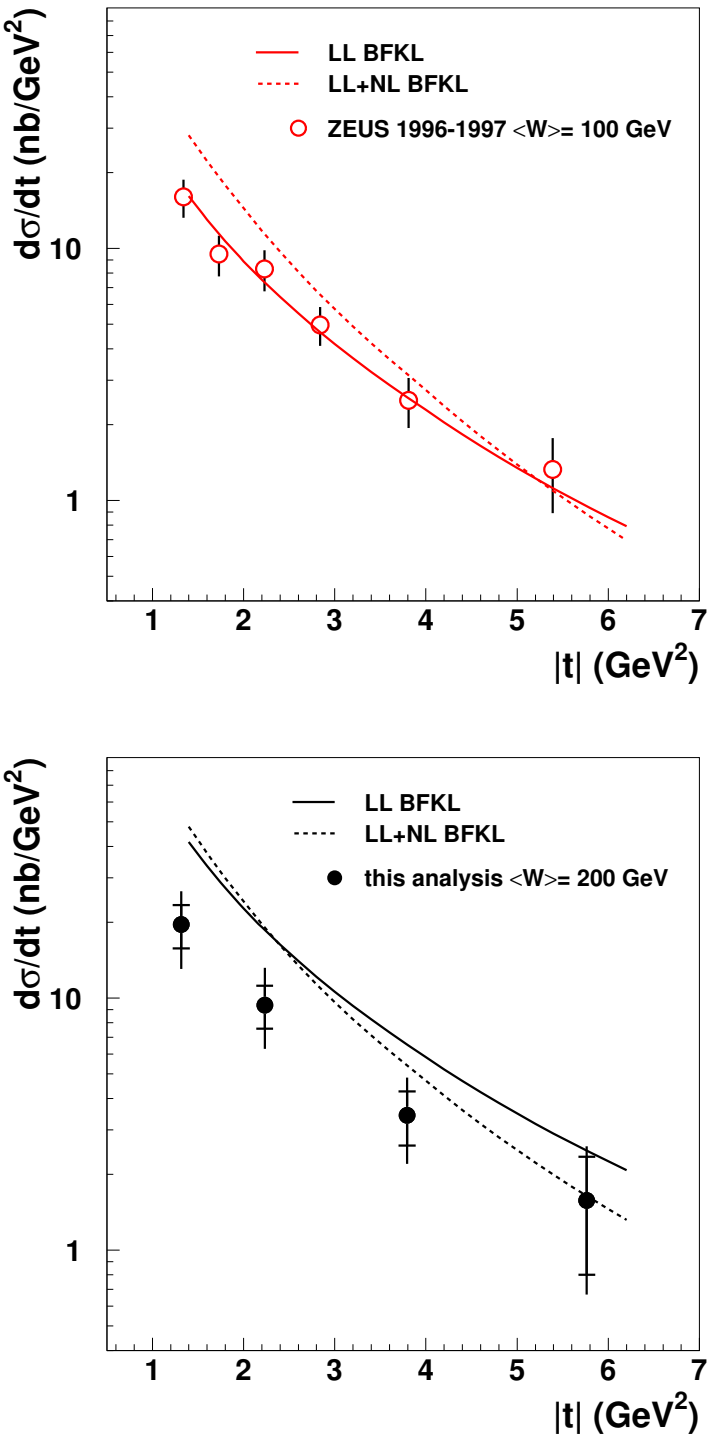

Figure 48: *Comparison of results of the present analysis ($W \approx 200\,GeV$) and the previous ZEUS measurement [7] ($W \approx 100\,GeV$) with the BFKL calculations in LL and LL+NL approximation.*

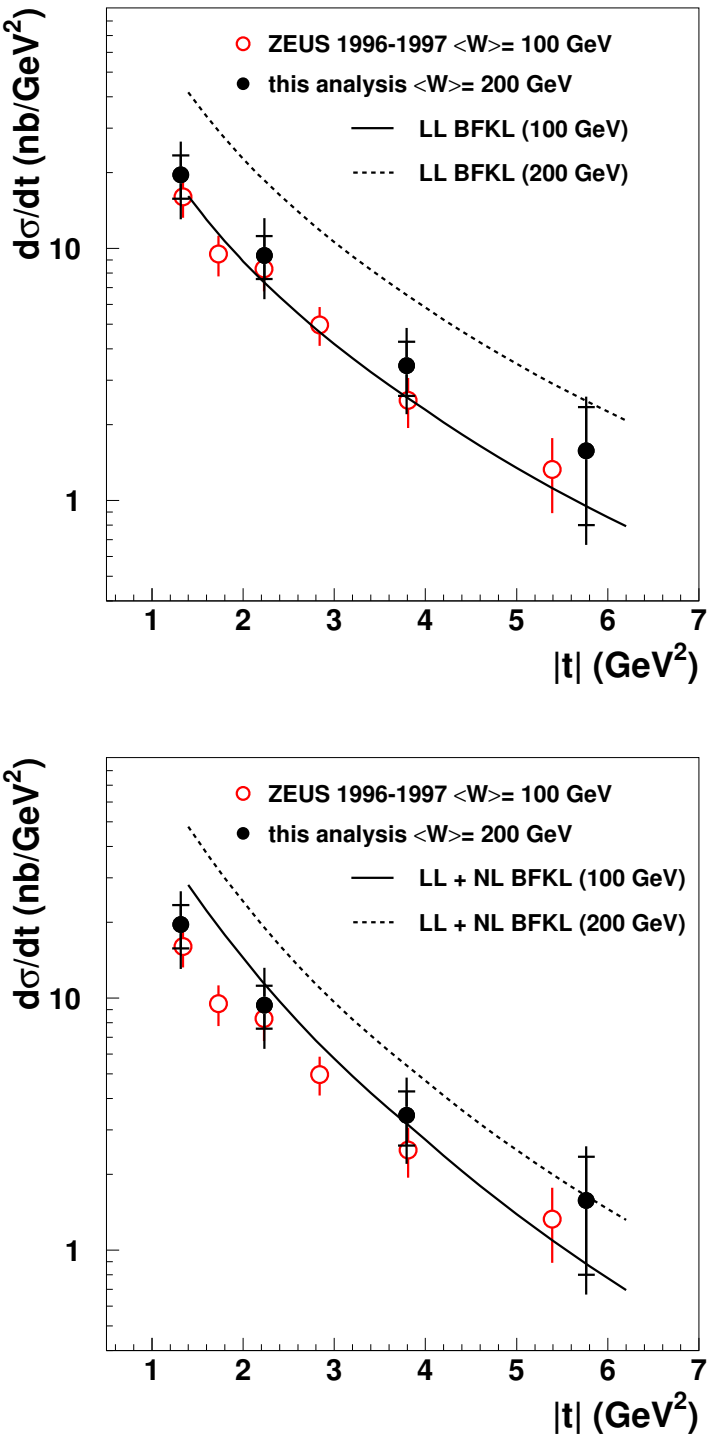

Figure 49: *Comparison of results of the present analysis ($W \approx 200$ GeV) and earlier ZEUS measurement [7] ($W \approx 100$ GeV) with the BFKL LL (upper plot) and BFKL LL+NL (lower plot) calculations for both energies.*

8.2 Comparison with DGLAP model

The γp scattering in the DGLAP model [78] is classified into three kinematic regions. The low $|t|$ region, $0 < |t| < Q_0^2$, where $Q_0^2 \sim 1\,\mathrm{GeV}$ is the input scale for DGLAP evolution, is dominated by the elastic processes. The second region, which is suitable to the studied process in this analysis, is the intermediate region $Q_0^2 < |t| < M_{J/\psi}^2$. The authors of the model suggest that the physics in this region is similar to the one of small $|t|$ region, i.e. the vector meson is produced quasi elastically while the proton dissociates into a diffractive mass. In this intermediate the process is dominated by logarithms of the form $(\log(M_{J/\psi}^2/|t|))$ due to momentum integration over loops in the ordered gluon ladder. For $|t| > M_{J/\psi}^2$ the momenta on the gluon ladder are no longer strongly ordered. In consequence the standard DGLAP evolution cannot be used.

The cross section is proportional to the squared gluon distribution

$$d\sigma/dt \propto \alpha_s^2(\bar{Q^2}) x G^2(x, \bar{Q^2}, t), \tag{63}$$

where, for $|t| < Q_0^2$, $\bar{Q}^2 = (Q^2 + M_{J/\psi}^2)/4$ and $x = (Q^2 + M_{J/\psi}^2)/W^2$. The parameters of the model were fitted to the total elastic J/ψ cross section [79]. The model was extended to the $Q_0^2 < |t| < M_{J/\psi}^2$ region by choosing $\bar{Q}^2 = (Q^2 + M_{J/\psi}^2)/\frac{|t|}{4Q_0^2}$ and $x = (Q^2 + M_{J/\psi}^2 + |t|)/W^2$ and fitted to the preliminary ZEUS proton-dissociative data [80] at $\langle W \rangle = 100\,\mathrm{GeV}$ and extrapolated to $\langle W \rangle = 200\,\mathrm{GeV}$.

The DGLAP model predicts a weak energy dependence of the differential cross section on the energy and approximately power-like $|t|$ dependence.

In Fig. 50 the results of the present analysis and preliminary ZEUS 1996-1997 [80] results for $\langle W \rangle = 100\,\mathrm{GeV}$ are compared with DGLAP calculation in the LL approximation for $\langle W \rangle = 100\,\mathrm{GeV}$ and $\langle W \rangle = 200\,\mathrm{GeV}$. The DGLAP calculations describe relatively well the shape of the cross section and its rise with energy.

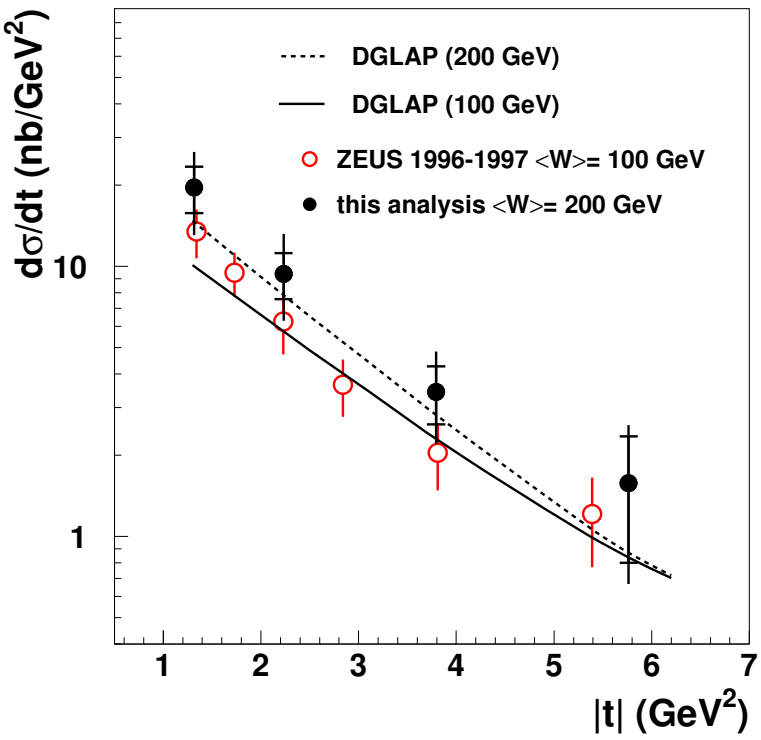

Figure 50: *Comparison of preliminary ZEUS 1996-1997 results [80] and the present results for kinematic range $x > 0.01$ with the DGLAP calculations in LL approximation.*

9 Summary

In this thesis the results of the measurement of the proton dissociative J/ψ meson photoproduction, $\gamma p \to J/\psi\, Y$, were presented. The analysis was a continuation of the previous ZEUS measurements and extended the available kinematic range to very large values of W. The data sample used in the analysis corresponds to integrated luminosity of $36\,\mathrm{pb}^{-1}$ and was collected in 1996 and 1997 with the ZEUS detector at HERA. The study was performed in the kinematic range of $185 < W < 245\,\mathrm{GeV}$ and $|t|$ values up to $7\,\mathrm{GeV}^2$.

The reconstruction of the J/ψ signal, dominated by the one track event topologies, was based on the information from the CTD, the CAL and the electron tagger located at 35 m from the IP. Tagging of a scattered electron allowed the extension of the W range and ensured low $Q^2 < 0.02\,\mathrm{GeV}^2$.

The selected kinematic variables were compared to the EPSOFT MC. The QED background was evaluated by means of the GRAPE MC. The comparison of many distributions showed agreement between the data and the MC.

The differential cross section was calculated in different kinematic regions, in order to compare it with the ZEUS and H1 measurements. These comparisons showed that within the errors the cross sections at 100 GeV and 200 GeV are compatible, however small rise with increasing energy is not excluded. The cross section for $|t| > 1\,\mathrm{GeV}^2$ was well described by the power-like dependence of the form $\sim |t|^{-n}$, predicted by pQCD models.

The results were compared to the pQCD based models using the BFKL as well as the DGLAP evolution equations. The existing models calculations for $\langle W \rangle \approx 100\,\mathrm{GeV}$ are in good agreement with the ZEUS data and indicates that large $|t|$ can provide a suitable hard scale for pQCD. In the case of the present analysis ($\langle W \rangle \approx 200\,\mathrm{GeV}$), the relative shape of the cross section is well reproduced by the BFKL LL and DGLAP models, but the normalization is rather overestimated (BFKL LL, BFKL LL+NL), although data seem to prefer the DGLAP evolution.

References

[1] J. J. Aubert et al., Phys. Rev. Lett. **33**, 1404 (1974).

[2] J.-E. Augustin et al., Phys. Rev. Lett. **33**, 1406 (1974).

[3] C. Bacci et al., Phys. Rev. Lett. **33**, 1408 (1974).

[4] J. D. Bjorken and S. Glashow, Phys. Lett. **11**, 255 (1964).

[5] S. Glashow, J. Iliopoulous and L. Maiani, Phys. Rev. **D2**, 1285 (1970).

[6] ZEUS Coll., J. Breitweg et al., Eur. Phys. J. **C14**, 213 (2000).

[7] ZEUS Coll., S. Chekanov et al., Eur. Phys. J. **C26**, 389 (2003).

[8] G. Levman. ZEUS-Note 95-088.

[9] R. Feynman, Phys. Rev. Lett. **23**, 1415 (1969).

[10] M. Gell-mann, Phys. Lett. **8**, 214 (1964).

[11] G. Zweig, CERN-8192/TH, p. 401 (1964).

[12] G. Zweig, CERN-8419/TH, p. 402 (1964).

[13] J. D. Bjorken and E. A. Paschos, Phys. Rev. **185**, 1975 (1969).

[14] H. Deden et al., Nucl. Phys. **B85**, 269 (1975).

[15] TASSO Coll., R. Badelik et al., Phys. Lett. **B86**, 243 (1979).

[16] V. N. Gribov and L. N. Lipatov, Sov. J. Nucl. Phys. **15**, 438 (1972).

[17] L. N. Lipatov, Yad. Fiz. **20**, 181 (1974).

[18] G. Altarelli and G. Parisi, Nucl. Phys. **B126**, 298 (1977).

[19] Yu. L. Dokshitzer, Sov. Phys. **JETP46**, 641 (1977).

[20] L. N. Lipatov, Sov. J. Nucl. Phys. **23**, 338 (1976).

[21] E. A. Kuraev, L. N. Lipatov and V. S. Fadin, Sov. Phys. **JETP44**, 443 (1976).

[22] I. I. Balitzky, L. N. Lipatov, Sov. J. Nucl. Phys. **28**, 822 (1978).

[23] M. L. Good and W. D. Walker, Phys. Rev. **120**, 1875 (1960).

[24] A. Donnachie and P. V. Landshoff, Phys. Lett. **B296**, 227 (1992).

[25] H. Abramowicz, A. Caldwell. DESY 98-192.

[26] T. Regge, Nuovo Cimento **14**, 951 (1959).

[27] T. Regge, Nuovo Cimento **18**, 947 (1960).

[28] P. D. B. Collins, *An Introduction to Regge Theory and High Energy Physics*. Cambridge University Press, 1977.

[29] G. F. Chew and S. C. Frautschi, Phys. Rev. Lett. **8**, 41 (1962).

[30] Particle Data Group, Eur. Phys. J. **C15**, 1 (2000).

[31] S. Donnachie, G. Dosch, P. Landshoff, O. Nachtmann, *Pomeron Physics in QCD*. Cambridge University Press, 2002.

[32] V. N. Gribov, Sov. Phys. **JETP 14**, 478 (1962).

[33] J. J. Sakurai, Phys. Rev. Lett. **22**, 981 (1969).

[34] J. J. Sakurai, D. Schildknecht, Phys. Lett. **B40**, 121 (1972).

[35] D. Yu. Ivanov et al., Phys. Lett. **B478**, 101 (2000).

[36] J. Bartels et al., Phys. Lett. **B375**, 301 (1996).

[37] ZEUS Coll., *The ZEUS detector*. Status Report 1993 DESY.

[38] N. Harnew et al., Nucl. Inst. and Meth. **A279**, 290 (1989).

[39] B. Foster et al., Nucl. Phys. **B (Proc. Suppl.)**, 181 (1993).

[40] B. Foster et al., Nucl. Inst. and Meth. **A338**, 254 (1994).

[41] M. Derrick et al., Nucl. Inst. and Meth. **A309**, 77 (1991).

[42] A. Andresen et al., Nucl. Inst. and Meth. **A309**, 101 (1991).

[43] B. Bernstein, Nucl. Inst. and Meth. **A336**, 23 (1993).

[44] K. Desler, U. Schneekloth. ZEUS-Note 95-061.

[45] H. Bethe, W. Heitler, Proc. Roy. Soc. **A146**, 83 (1934).

[46] H. Bethe, Phys. Rev. **89**, 1256 (1953).

[47] J. Andruszków et al.. DESY 92-006.

[48] J. Crittenden et al., *The C5 upgrade*. ZEUS Note 01-002.

[49] R. Brun et al., *GEANT 3.13*, 1987. CERN DD/EE/84-1.

[50] S. M. Fisher and P.Palazzi, *The ADAMO Data System*. Programmers Manual.

[51] R. van Woudenberg, *ZGANA Version 3.05/01, User Manual and Documentation*, 1993.

[52] M. Kasprzak. Ph.D. Thesis, DESY F35D-96-16, (1996).

[53] L. Adamczyk. Ph.D. Thesis, DESY-THESIS-1999-045,(1999).

[54] HERWIG: A Monte Carlo Event Generator for Simulating Hadron Emission Reactions with Interfering Gluons, Vol. 67, 1992.

[55] H. Abramowicz, A. Levy, *The ALLM parametrization of $\sigma(\gamma^* p)$, an update*, 1997. DESY-97-251.

[56] T. Abe, Comp. Phys. Comm. **136**, 126 (2001).

[57] T. Ishikawa et al., *GRACE manual*, 1993. KEK-report 92-19.

[58] F. W. Brasse et al., Nucl. Phys. **B110**, 413 (1976).

[59] A. Muecke et al., Comput. Phys. Commun. **124**, 290 (2000).

[60] G. F. Hartner, *VCTRAK Briefing: Program and Math.* ZEUS Note 98-058.

[61] N. Tuning, *ZUFOs: Hadronic final state reconstruction with calorimeter, tracking and backsplash correction.* ZEUS Note 01-021.

[62] N. Tunning. Ph.D. Thesis, Amsterdam, 2001.

[63] A. Caldwell et al.. ZEUS-Note 98-018.

[64] ZEUS Luminosity Group, L.Adamczyk et al.. ZEUS Note 01-004.

[65] G. Abbiendi et al., *Observation of $J/\psi \to \mu^+\mu^-$ in the first $274\,nb^{-1}$ of 1993 run.* ZEUS Note 93-120.

[66] A. Bertolin, R. Brunera, L. Stanco, *Measurements of inelastic J/ψ photoproduction at HERA with 1994 data.* ZEUS Note 98-076.

[67] J.Tandler, *Exclusive J/ψ Production at Very Low Q^2.* ZEUS Note 02-017.

[68] *Exclusive Electroproduction of J/Ψ Mesons at HERA.* Paper in preparation.

[69] ZEUS Coll., S. Chekanov et al., Eur. Phys. J. **C24**, 345 (2002).

[70] F.James, M.Roos, *MINUIT Function Minimization*, 1996. CERN-Note D506.

[71] A. Bruni, *private communication.*

[72] M. Corradi, *private communication.*

[73] R. Enberg et al., Eur. Phys. J. **C26**, 219 (2003).

[74] H1 collab, A.Aktas et al.., Phys. Rev. Lett. **B568**, 205 (2003).

[75] J. R. Forshaw and M. G. Ryskin, Z. Phys. **C68**, 137 (1995).

[76] J. R. Forshaw and G. Poludniowski, Eur. Phys. J. **C26**, 411 (2003).

[77] A. H. Mueller and W-K. Tang., Phys. Lett. **B284**, 123 (1992).

[78] E. Gotsman et al., Phys. Lett. **B532**, 37 (2002).

[79] H1 Coll., C. Adloff et al., Phys. Lett. **B483**, 23 (2000).

[80] ZEUS Coll., *contributed paper 556.* International Europhysics Conference on High Energy Physics, Budapest 2001.